Engineering a noise-free quantum memory for temporal mode manipulation

Thomas Muir Hird
St Catherine's College, Oxford

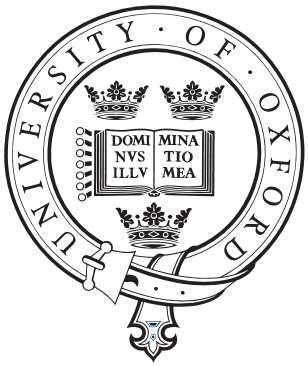

Submitted for the degree of Doctor of Philosophy
Trinity Term 2021

Supervised by
Dr Patrick M. Ledingham and Prof. Ian A. Walmsley

Clarendon Laboratory
University of Oxford
United Kingdom

Engineering a noise-free quantum memory for temporal mode manipulation

Thomas Muir Hird
St Catherine's College, Oxford

Submitted for the degree of Doctor of Philosophy
Trinity Term 2021

Abstract

An optical quantum memory, a device which can store and retrieve on demand an arbitrary quantum state at the single photon level, has been identified as a significant cornerstone of photonic quantum technologies. The development of such a memory would allow the creation and development of a large number of quantum technologies. These would range from the ability to synchronise processing steps in an optical quantum computer, to the construction of a quantum repeater which would allow faithful transmission of quantum states over arbitrarily long distances.

In this thesis I investigate broadband light storage in a room-temperature Raman memory for purposes of quantum information processing with photons. During the course of this thesis, a novel scheme to suppress four-wave mixing noise is simulated, based on equations derived to describe the physics of the memory interaction. The experimental arrangement to test the suppression method is described and an original method using photon statistics is demonstrated. The results of these experiments prove the ability of the memory to retrieve and maintain the non-classicality of the state, given a single photon input.

Following the affirmation that, using this noise suppression technique, the memory can function at the single-photon level, I go on to consider how the temporal-spectral properties of a pulsed mode of light may be manipulated using the memory. There are two primary reasons for this investigation: 1) Increasing the efficiency of the *read-in* process by carving the optimum mode of the memory 2) Using the memory as a device operating in a high dimensional quantum information basis. The restrictions of such applications are considered and a method to test the efficacy of transformations in this basis is devised and experimentally tested. I also perform demonstrations of light storage using conventional temporal modes using a novel method of velocity selection within warm vapour.

Finally I detail further experiments that are achievable with the Raman quantum memory given the progress that has been achieved during my DPhil research. The results show that the Raman memory is a viable candidate for a practical route towards low-noise quantum storage and for manipulation of temporal modes of light.

To my teachers

Acknowledgements

This thesis is dedicated to my teachers, and I can think of no one who has taught me more about quantum optics, being a scientist, the importance of acronyms, and life itself, than the Quantum Boss himself, Dr Patrick Ledingham – Cheers mate. My research in the group was always been under the watchful eye of Provost Walmsley to whom I owe a great deal. Thank you for captaining the ship that is HMS Ultrafast.

My time in the group was made all the more enjoyable by the crew. From the Big Dogs, including Benni, Helen, and Jamie to the ship's cats (my fellow PhD students) Oscar, Toms, Alex, Joelle, James and many others... thank you all for the good times. Within the motley meme team I was blessed with an expert troupe in Dylan, Jonas, Joe and Sarah; truly I could not have done it without you all. Drs Thomas and Munns, our times in crossword corner will be sorely missed. To my Main man, Dougal, you were a pleasure to have in the lab and I look forward to hearing about your future endeavours. Beyond the group I've always had my friends, both near and far to rely on when seas got rough. If I were to list them all, a universal quantum computer might be realised by the time I finished, but to name a few would be Anna, Dom, Dumper, Irish, Sarah and Hannah, Cogs and the Lewis' and Biscuit(s)[1].

Finally to my family, my parents Michael and Vicky, and my sisters Bids, Emma, and Ellie, thank you for more than I can possibly say. To Sammy whose unconditional love and support mean the world to me, and my daughter Darcey, this is for you. Thank you.

[1]Biscuit is the name of a dog, but Rich Tea Biscuits also played a critical part of my DPhil.

People acknowledged in the text

P.M.L: Dr Patrick Ledingham

S.E.T: Dr Sarah Thomas

J.H.D.M: Dr Joseph Munns

J.N.B: Dr Jonas Becker

D.J.M: Dougal Main

O.L.A: Oscar Lazo-Arjona

J.N: Dr Josh Nunn

S.G: Shabo Gao

Author's publications

Journal articles

1. S. E. Thomas, **T. M. Hird**, J.H.D. Munns, B. Brecht, D. J. Saunders, J. Nunn, I. A. Walmsley and P. M. Ledingham, "Raman quantum memory with built-in suppression of four-wave-mixing noise." *Physical Review A, 100(3)*,033801, 2019.

2. D. Main, **T. M. Hird**, G. Gao, E. Oguz, D. J. Saunders, I. A. Walmsley and P. M. Ledingham, "Preparing narrow velocity distributions for quantum memories in room-temperature alkali-metal vapors." *Physical Review A, 103(4)*,043105, 2021.

3. D. Main, **T. M. Hird**, G. Gao, I. A. Walmsley and P. M. Ledingham, "Room temperature atomic frequency comb storage for light" *Optics Letters, 46.12,* 2960-2963, 2021.

4. **T. M. Hird**, J. H. D. Munns, S. E. Thomas, J. Nunn, P. M. Ledingham, J. Sperling, B. Brecht and I. A. Walmsley "Temporal-mode selectivity with a Raman quantum memory." *in preparation*

Selected conference publications

1. **T. M. Hird**, S. E. Thomas, J. H. D. Munns, O. L. Arjona, S. Gao, J. Nunn, B. Brecht, D. J. Saunders, P. M. Ledingham, and I. A. Walmsley, "Engineering a noiseless and broadband Raman quantum memory for temporal mode manipulation." *Laser Science JW3A-63*, Optical Society of America, 2018.

2. **T. M. Hird**, S. E. Thomas, J. H. D. Munns, B. Brecht, D. J. Saunders, J. Nunn, I. A. Walmsley and P. M. Ledingham, "Noise Suppression via Atomic Absorption in a Raman Quantum Memory" *Quantum Information and Measurement T5A. 76*, Optical Society of America, 2019.

3. **T. M. Hird**, D. Main, G. Gao, E. Oguz, D. J. Saunders, I. A. Walmsley and P. M. Ledingham, "Demonstration of an Atomic Frequency Comb Quantum Memory Using Velocity-Selective Pumping in Warm Alkali Vapour." *CLEO: QELS_Fundamental Science FW4C.5*, Optical Society of America, 2020.

Contents

List of Figures

Chapter 1

Introduction

> "Begin at the beginning," the King said, gravely,
> "and go on till you come to the end: then stop."
>
> Lewis Carroll, *Alice in Wonderland*

The concept of a quantum memory for light is a simple device. Its purpose is to interact with a pulse of light carrying quantum information, store that information for some length of time, and then re-dispatch it as a propagating pulse on demand. The fact that quantum information cannot be copied dictates that an effective quantum memory cannot involve measurement and must operate at high efficiency. Any record or trace of the pulse that remains represents lost information.

This thesis presents the progress towards a noise-free quantum memory and discusses applications that such a memory could be used for. This chapter provides background on why quantum memories are significant, what they can be used for, and how they might be implemented.

1.1 Quantum Information

The motivation for quantum memories is given by the 20th-century revolution in quantum information. Whilst classical information is traditionally stored in *bits*, a *qubit* is an object that lives in a two-dimensional Hilbert space with basis states $|0\rangle$ and $|1\rangle$. A quantum bit is the building block of quantum information; the primary distinction being that a qubit can exist in any superposition of its basis states. Common examples of qubits include the spin-state of a spin-$\frac{1}{2}$ particle or the polarisation of a photon. Systems with three or more basis states (qutrits, qudits) have been shown to have some advantages but often come with additionally practical complexities.

A general qubit is represented by a linear combination of basis states $|\psi\rangle = \alpha\,|0\rangle + \beta\,|1\rangle$, where α and β are complex numbers and obey the normalisation condition $|\alpha|^2 + |\beta|^2 = 1$. A measurement of the state $|\psi\rangle$ projects it onto a basis;, for example $|0\rangle, |1\rangle$, but a superposition of states can itself be used as a basis e.g. $|+\rangle = \frac{|0\rangle+|1\rangle}{\sqrt{2}}$. The coefficients α and β will determine the probabilities of each measurement outcome.

Multiple qubits also possess the ability to have correlations beyond what is possible for classical states. This property is known as entanglement and can be demonstrated by considering the two-qubit state:

$$\left|\Phi^+\right\rangle = \frac{1}{\sqrt{2}}(|0\rangle_A\,|1\rangle_B + |1\rangle_A\,|0\rangle_B). \tag{1.1}$$

This is impossible to write as the product of two independent qubits A and B. A measurement on only qubit A yields a random result of either $|0\rangle$ or $|1\rangle$; each with 50% probability. However, measuring one qubit will immediately fix the state of the other qubit

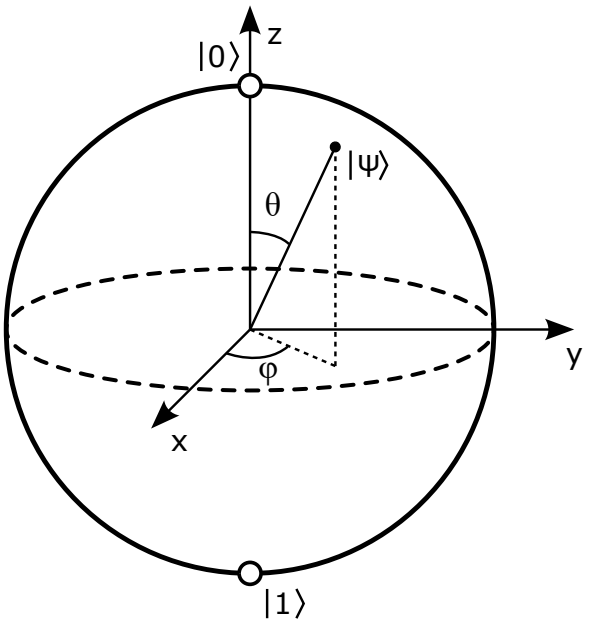

Figure 1.1: Bloch sphere representation of a qubit. Probability amplitudes of a superposition $|\psi\rangle = \alpha\,|0\rangle + \beta\,|1\rangle$ are given by $\alpha = \cos\left(\frac{\theta}{2}\right)$ and $\beta = e^{i\phi}\sin\left(\frac{\theta}{2}\right)$. Figure from [1].

should it be measured in the same basis. This correlation is independent of the spatial separation; leading to the famous adage of "spooky action at a distance".

This appears initially no different to classical correlations; measuring the handedness of a glove will instantly provide information about the spatially separated other half. The difference? Gloves do not have phase, nor are they governed by the Heisenberg uncertainty principle for conjugate variables. Only one kind of measurement exists for a gloves handedness whilst a qubit may be measured in the $|0\rangle, |1\rangle$ basis or any superpositional bases; and the results will remain correlated in all measurements.

Bell proposed a bound to illustrate the difference between these correlations compared to the glove case where it is just the experimentalist who is ignorant in a universe that "knows" the measurement outcome ahead of time[2]. These hidden variable theories have been subsequently ruled out[3] with recent work considered to be loophole-free[4].

These properties of superposition and entanglement have been identified to yield signi-

ficant improvements in the following key areas of *Quantum Technology*[1]:

1. **Cryptography**: It is not the cryptography itself which quantum technologies can improve on; there are a wealth of classical algorithms which are deemed to be, to all intents and purposes, unbreakable [6]. The problem is that they require a key – a piece of pre-shared information; however many scenarios where you wish to encrypt information is between two parties who have previously had no interaction. This has lead to the field of *quantum key distribution* (QKD) with seminal work performed by Bennett and Brassard [7] and Ekert [8] in 1984 and 91 respectively, where they created provably secure key distribution protocols. Other classical techniques do exist for these scenarios however they rely on a computational difficulty – computations that might be shown to be possible with quantum computation. The record distance for which QKD could currently be conceived would be approximately 1200 km after Jianwei Pan's group demonstrated entanglement between two ground stations via a photonic satellite link [9].

2. **Computation**: The advantage of quantum computing is often described as a result of the superposition possible by qubits; by existing in a superposition of $|0\rangle$ and $|1\rangle$ quantum computers can explore all possible combinations in parallel. This is compared to a classical algorithm which may be forced to evaluate all possible combinations. Whilst this pop-science description is not strictly true, by exploiting *quantum contextuality*[2], a number of quantum computing algorithms have been shown to scale

[1] A third significant area is *Quantum Metrology* but at present quantum memories do not play a significant role. See [5] for a recent review on the field.

[2] Contextuality is the idea that the measurement outcome of a quantum observable is dependent on any other observables exist within the same measurment set. In 2014, contextuality was identified as the critical resource that gives quantum computers their advantage [10]. For recent reviews on quantum contextuality see [11, 12].

more favourably than the best, currently known, classical algorithm. Perhaps the most famous example of this quantum advantage is Shor's algorithm to factorise an integer into its constituent primes [13]. The resources required for prime factorisation by the best known classical means grows sub-exponentially[3] with input size whilst Shor's algorithm grows "only" polynomially. Many classical cryptography algorithms such as RSA relied on the complexity of the factoring problem [15], the potential for quantum computers to quickly factorise numbers and thus break the encryption has lead to the fame/infamy of Shor's algorithm. Experimental demonstration has been shown in a number of different systems, beginning with the factorisation of 15 (into 3 and 5) [16], with the current state of the art being factoring 21 using photonic quantum computation [17]. Other quantum algorithms showing speed-up over their classical counterparts include Grover's algorithm for the search in an unordered database [18] as well as data fitting [19], and linear solver [20,21] algorithms.

The ability to surpass the current classical limits in these applications has naturally produced significant effort into the development of possible architectures. To date, there is no single architecture that satisfies all of the requirements[4] needed to implement quantum computing. For the transfer of quantum information, optical-frequency photons make a promising "flying qubit" since they travel at the speed of light and interact weakly with the environment. They are also noise-free at room temperature and possess multiple degrees of freedom such as spatial/temporal modes and polarisation. Single qubit unitaries can be implemented with simple linear optics such as waveplates, phase-plates and beam-splitters.

[3] This is to say, the resources required scales with input size faster than any polynomial whilst still smaller than an exponential scaling: $\mathcal{O}\left(e^{(\log(N))^{1/3}(\log(\log(N)))^{2/3}}\right)$ [14].

[4] The requirements are generally stated as the DiVincenzo criteria[22] and are: Scalability, initialisation, universal gates, qubit measurement capability and a long enough decoherence time.

The following section describes the quantum nature of photons, and describes the degrees of freedom which can be used to garner the fabled *quantum advantage*.

1.2 Quantum states of light

A photon is defined as an elementary excitation of a single mode of the electromagnetic field. A single photon state can be defined [23] as the light field for which the measurement with a number-resolving detector of perfect detection efficiency yields one for the mean number and zero for the variance[5].

For use in linear optical quantum computing (LOQC), Photons need to have two key properties: one, that they are true single photons, and two, that every photon in the experiment is identical. A vital component of scalable quantum information processing is therefore a bright source of indistinguishable, pure single photons in the Fock state $|1\rangle$. Measures of purity and indistinguishability are vital to determining the merit of different single-photon sources. Other important considerations are the brightness of the source, the emission wavelength, the temperature at which the source must be operated and whether it is deterministic or probabilistic.

The archetypal experiment to measure indistinguishability is the Hong-Ou-Mandel (HOM) effect [24], which observes quantum interference of two photons at the outputs of a beam splitter. If two single photons are incident on a beam splitter then we describe the input mode as a two-photon Fock state in input modes a and b i.e. $|\psi\rangle_{\text{in}} = |1,1\rangle_{ab} = \hat{a}^\dagger \hat{b}^\dagger |0,0\rangle_{ab}$. The 50:50 beam splitter performs a unitary transformation on the input optical modes to output

[5] Chapter 3 will speak in detail on the statistics of photon states.

modes $\hat{c}$ and $\hat{d}$ such that

$$\begin{aligned} \hat{a}^\dagger &\to \frac{\hat{c}^\dagger + \hat{d}^\dagger}{\sqrt{2}} \\ \hat{b}^\dagger &\to \frac{\hat{c}^\dagger - \hat{d}^\dagger}{\sqrt{2}}. \end{aligned} \tag{1.2}$$

The output state is then given by:

$$\hat{a}^\dagger \hat{b}^\dagger \left|0,0\right\rangle_{ab} \to \frac{1}{2}(\hat{c}^\dagger + \hat{d}^\dagger)(\hat{c}^\dagger - \hat{d}^\dagger) \left|0,0\right\rangle_{cd} \tag{1.3}$$

$$= \frac{1}{2}\left((\hat{c}^\dagger)^2 - (\hat{d}^\dagger)^2 - \hat{c}^\dagger\hat{d}^\dagger + \hat{d}^\dagger\hat{c}^\dagger\right) \left|0,0\right\rangle_{cd} \tag{1.4}$$

If the two photons on the input ports a and b are *completely* indistinguishable, the last two terms in the above expression cancel and the output is:

$$\left|\psi\right\rangle_{\text{out}} = \frac{1}{2}\left((\hat{c}^\dagger)^2 - (\hat{d}^\dagger)^2\right) \tag{1.5}$$

$$= \frac{1}{\sqrt{2}}(\left|2,0\right\rangle_{cd} - \left|0,2\right\rangle_{cd}) \tag{1.6}$$

The $\left|1,1\right\rangle_{cd}$ state has disappeared due to quantum interference between the pathways and therefore if two identical photons are incident on a 50:50 beam splitter they will always exit the same port, meaning we will not measure any coincidence events between the output ports of the beamsplitter. However, by (for example) introducing a temporal delay between the two photons, we can gradually make them distinguishable. The degree to which we observe this *bunching* effect or lack of conincidences is a measure of the indistinguishability of the photons. The coincidence probability is given by $p_{1,1} = \frac{1}{2}\left(1 - |\langle\psi_a|\psi_b\rangle|^2\right)$ thus vanishing for identical inputs and yields a visibility of the indistinguishability measurement $V = \text{Tr}(\rho_a\rho_b)$. In the case of weak coherent states the HOM visibility is limited to 50% as multi-photon contributions lead to coincidence detections.

1.2.1 Single photon sources

Spontaneous Parametric Down Conversion

The most commonly used single photons sources currently rely on probabilistic processes such as spontaneous parametric down conversion (SPDC) or spontaneous four-wave mixing (SFWM). SPDC is a second-order nonlinear process in which a pump photon (p) is converted into two, lower energy photons called the signal (s) and the idler (i). The down-conversion is known as Type-I if the daughter photons have the same polarisation, and Type-II if they have orthogonal polarisation. SPDC occurs in materials with a non-zero second order susceptibility $\chi^{(2)}$, i.e. non-centrosymmetric crystals such as Potassium titanyl phosphate (KTP) and Beta barium borate (BBO) [25]. The process conserves both energy and momentum, therefore the frequencies and wavevectors of the down-converted photons satisfy:

$$\omega_{\mathrm{p}} = \omega_{\mathrm{s}} + \omega_{\mathrm{i}} \tag{1.7}$$

$$\mathbf{k}_{\mathrm{p}} = \mathbf{k}_{\mathrm{s}} + \mathbf{k}_{\mathrm{i}}. \tag{1.8}$$

SPDC photons are always produced in pairs and the output state of a SPDC source is a two-mode squeezed vacuum:

$$|\Psi\rangle_{\mathrm{SI}} = \sqrt{1-\lambda^2} \sum_{n=0}^{\infty} \lambda^n |n\rangle_{\mathrm{S}} |n\rangle_{\mathrm{I}} \tag{1.9}$$

where $|n\rangle_{\mathrm{S/I}}$ is an n-photon Fock state in the signal/idler mode respectively, and λ is the squeezing parameter which is determined by properties of the nonlinear crystal and the

power of the pump beam. By increasing the pumping power we can increase λ and therefore increase the single photon pair production rate, but this also increases the multi-photon events. Therefore to have a true single-photon heralded state we need to keep the squeezing sufficiently low to suppress higher order events, and the single photon brightness is limited to $\lambda \lesssim 0.1$ [26].

Quantum Dot Single Photon Sources

A different, rapidly improving platform for single-photon sources is based on semiconductor quantum dots (QDs) in photonic structures. A quantum dot is a nanoscale semiconductor embedded in higher band gap semiconductor. This confines charge carriers in all three dimensions and generates an isolated two-level system with discrete energy levels. It has been shown that this "artificial atom" can emit single [27] and indistinguishable photons [28], and QD sources do not suffer from multi-photon events like SPDC, simply because the quantum dot is a single emitter. For years the main challenges have been to efficiently collect the emitted single photons and obtain high values of indistinguishability.

Recent results have demonstrated that by deterministically fabricating a microcavity around a quantum dot, using in-situ lithography, ultrabright sources of indistinguishable photons can be produced [29,30]. The cavity enhances emission into a single spatial mode which can be collected with high efficiency by minimising all sources of loss from the QD to the output of a single mode fibre. The current world leading effort in this field is performed by Tomm *et al.* [31] from earlier this year, demonstrating 57% single photon collection efficiency whilst maintaining two-photon interference visibility of 97.5% at a clockcycle of 1 GHz.

We now briefly outline some of the means of which quantum information could be stored in photons[6].

1.2.2 Degrees of freedom

- **Polarisation:** Perhaps the most common basis of quantum information for photons. Classically, light is an electromagnetic wave produced by oscillation of electric and magnetic fields in the plane orthogonal to the direction of propagation. The polarisation is represented by the direction of the electric field oscillations $\boldsymbol{E}$; if $\boldsymbol{E}$ is in a straight line in a fixed direction, it is said to be linearly polarised. The electric field can also rotate as it oscillates, tracing out an ellipse, or, in the two extreme cases, tracing a circle, producing either left- or right- circularly polarised light. Any polarisation can be expressed as a linear combination of horizontal and vertical polarisation: $\alpha |H\rangle + \beta |V\rangle$. Horizontal and vertical form the basis qubit states with single qubit gates performed by birefringent materials and polarisation beamsplitters (PBS); these, combined with single photon detectors allow for measurement in this basis. Using polarisation qubits both QKD and quantum computations have been demonstrated numerous times[33–37] including being used for the demonstrations of Shor's algorithm[38]. This has been enabled by the breadth of research conducted into photons entangled in the polarisation degree of freedom[39–41].

- **Spatial:** This multi-dimensional basis makes use of the transverse mode profile that a single photon has. This degree of freedom has been exploited in a number of ways including orbital angular momentum[42–44] and spatial modes[45,46]. These have often

[6] We shall restrict ourselves to discrete variables for QIP. For a comprehensive text on using continuous variables in quantum information see [32].

been combined with polarisation to create hyper-entangled states across multiple degrees of freedom [47]. These modes do, however, suffer from their incompatability with single mode fibres and sensitivity to propagation effects [48,49].

- **Time/Frequency bins:** These qubit states borrow heavily from classical photonics, taken to the single photon limit. These modes make use of schemes whereby the occupation (photon vs no photon) of a time or frequency bin (or window) is considered. These modes benefit from relative insensitivity to inhomogeneities in transmission mediums and has benefited greatly from advances in switching technology [36,50] including a simulation of a 2 dimensional quantum random walk based on a time-bin encoding and fast polarisation switching [51].

- **Temporal modes:** Frequency, and its conjugate variable time, can be discretised in bins as described above, with dimensionality limited to the time/frequency window available for the encoding. This however does not make optimum use of the space. We can instead define field orthogonal modes existing in overlapping spaces within the time-frequency domain. These *temporal modes* (TM) can be thought of as the temporal (or spectral) profile of a light pulse and can form a complete basis that are the natural basis for single photons produced by PDC [52]. Unlike orbital angular momentum (OAM) modes of light they exist in the same spatial mode, and are hence compatible with single mode fibres [53]. These modes will be investigated in detail in Chapter 5.

1.3 Quantum memories

As alluded to earlier, a photonic quantum memory is a device that is able to store and retrieve a quantum state of light. The ability to store and retrieve quantum states of light has been highlighted as a solution to a number of challenges within photonic quantum information processing (QIP). Quantum memories have been shown to have applications ranging from extending the range of quantum communication channels [54], developing deterministic single-photon sources [55] and synchronising multi-photon quantum computation protocols [56].

The two applications which have been driving factors in the development of quantum memories are applications of *temporal multiplexing* and the realisation of a *quantum repeater*. Multiplexing provides a solution to the scaling problem in photonic quantum networks as well as providing a means to generate deterministic single photons which forms a constituent part of universal quantum computing proposals [57] (as well as in some quantum repeater proposals [58]).

Every application of a quantum memory demands a specific set of requirements in order to reach their best performance, with no platform nor protocol able to meet all criteria. The rest of this chapter will outline the applications, the metrics by which we can compare quantum memory protocols and the protocols themselves. The bulk of this thesis focuses predominantly on a quantum memory based on the off-resonant Raman interaction in a room-temperature atomic caesium ensemble.

1.3.1 Applications

The transfer of arbitrary quantum states can be achieved between parties sharing an entangled system. The problem lies in the distribution of this entanglement; current optical fibres can reliably transfer quantum states short distances but are limited by photon losses in the fibre and decoherence. The solution, as proposed by Briegel et al.[59], is to have the transmission length divided into segments separated by nodes of quantum repeaters. The crucial finding of Briegel was that the decay of the information with a repeater architecture could scale polynomially and not exponentially with distance. The objective of the repeater is to perform entanglement swapping with an adjacent node such that two nodes further apart then become entangled. This is again an inherently probabilistic process and as such quantum memories are required so a node can wait until entanglement has been heralded in an adjacent one.

It is worth mentioning at this point that the potential applications go beyond the two explored in detail below. For example, the possibility for entanglement enhanced sensing whereby the storage of entanglement is used as a resource with applications in improving the precision of quantum sensors[60,61].

Quantum repeaters

The idea behind a quantum repeater is to allow entanglement to be "swapped" by a measurement such that entanglement is transferred to other quantum systems which are further apart.

Figure 1.2 shows a simple schematic for a quantum repeater node consisting of an EPR source for producing entangled photons and quantum memories. If the distance between 1

and 2 is so great that transmission of quantum information is practically impossible because of fibre loss, then the distance can be reduced by the addition of a quantum repeater. The photons are stored in the memories until the adjacent memory has also stored a photon. The pair can be recalled on demand and by way of a Bell-state measurement the entanglement is projected onto another pair of states (be they photons or photons stored in memories in other nodes)[7]. The extension of the set-up shown in Figure 1.2 is simple, by just adding subsequent nodes the distance between 1 and 2 can become arbitrarily large.

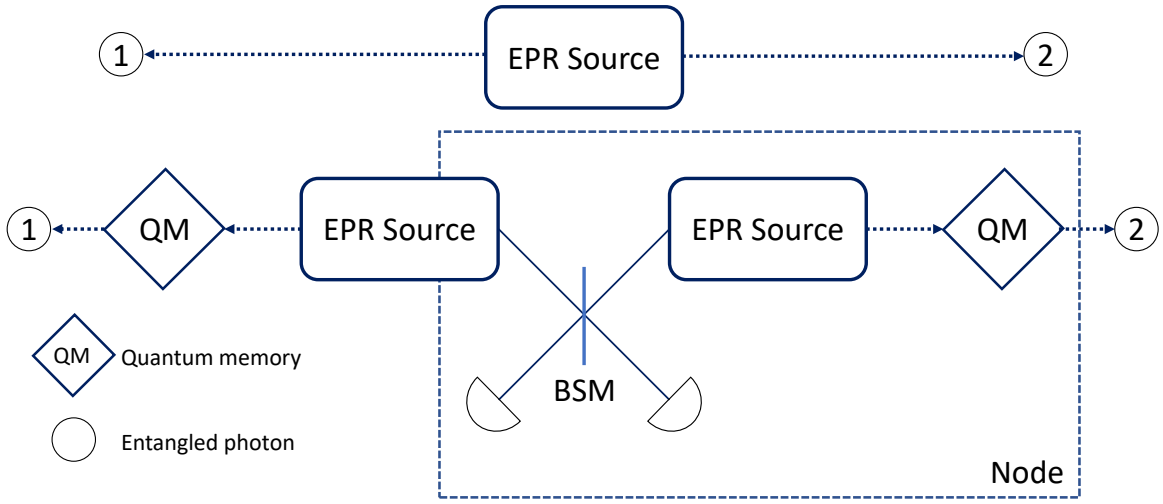

Figure 1.2: Showing how the distance travelled by a photon from an EPR source, to create entanglement between two parties (1 and 2), reduces with the addition of a quantum repeater node. The Bell state measurement (BSM) causes the entanglement to be projected such that 1 and 2 now share a maximally entangled pair.

The realisation of a quantum repeater would fill the gap between local processing (such as that performed by a quantum computer) and the long-distance communication of quantum information (the basis of a *Quantum Internet*[62]). There is little doubt therefore that the development of a quantum repeater (and by extension, quantum memories) is one of significant importance.

[7]The result of the Bell-state measurement can be seen explicitly when the DLCZ protocol is examined in Section 1.3.3

Temporal multiplexing

As outlined above, temporal multiplexing is the synchronisation of successful probabilistic outcomes which are repeatedly attempted [63]. Synchronisation is achieved by storing the heralded outputs of successful operations inside a quantum memory and synchronising the output [64]. We now consider the improvement a quantum memory would provide to the significant issue of single-photon synchronisation.

The optical pumping of a non-linear $\chi^{(2)}$ crystal provides a means to produce heralded single photons via spontaneous parametric down-conversion (SPDC) [65]. This process is stimulated by random vacuum fluctuations and is therefore an inherently probabilistic process. For use as a single-photon source, it is a necessity that SPDC sources be operated with a low probability of production $p \ll 1$ (typically $p \sim 0.01$) [66] such that the likelihood of multi-photon events is negligible.

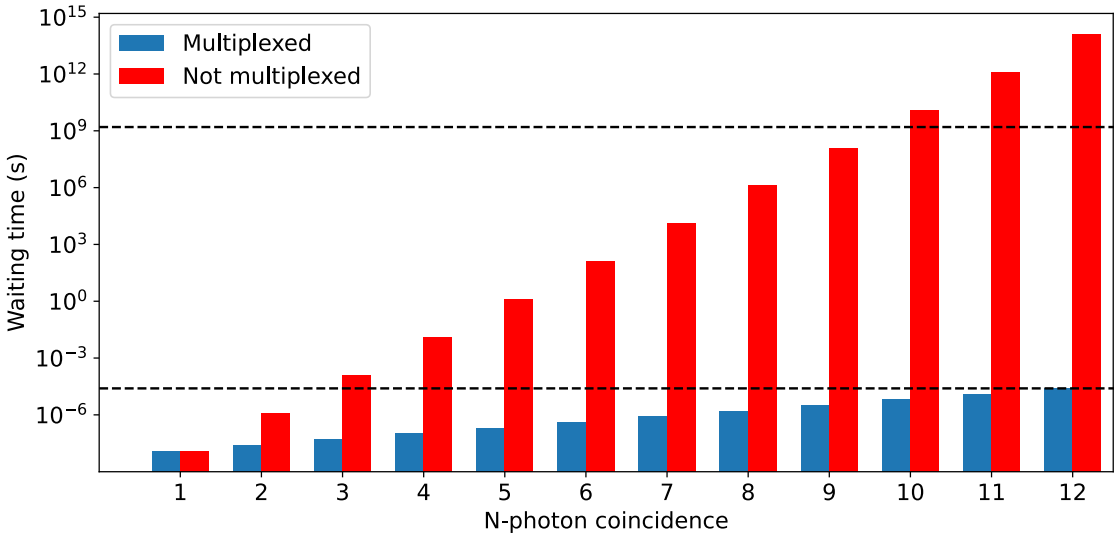

Figure 1.3: Waiting times for an N-fold photon coincidence with and without the temporal multiplexing strategy described in [67]. A memory efficiency and time-bandwidth product are $\eta = 50\%$, $B = 1000$ are assumed with a repetition rate of 80 MHz. The upper and lower dotted lines are at 50 years and 25 µs respectively.

The probability of producing N single photons from N sources simultaneously scales exponentially (p^N); the probability of producing 10 simultaneous photons is of order 1 in 10^{20}. Nunn *et al.*[67] describes how memories can be used to solve this issue with N memories and N probabilistic single-photon sources. Once $N-1$ memories are storing single photons they are all read-out on demand, heralded by the emission of the N^{th}, yielding an N-fold coincidence. The dramatic reduction in waiting time can be seen in Figure 1.3. It has been shown that the rate of this coincidence is dependent upon the time-bandwidth product and efficiency of the memory, metrics which we shall define in the following section.

1.3.2 Figures of merit

The usefulness of a quantum memory is broadly parameterised by its bandwidth, storage time and mode-capacity; all of which are defined with respect to the efficiency with which the information is retrieved. In addition to these metrics, technical simplicity and ease of implementation and miniaturisation allow for practical implementation within a QIP network.

Efficiency

Efficiency (η) measures the energy ratio between the retrieved and input states. This can be given as $\eta = \langle N_{\text{out}} \rangle \,/\, \langle N_{\text{in}} \rangle$ where $\langle N_{\text{in}} \rangle$ and $\langle N_{\text{out}} \rangle$ are the average photon numbers per pulse for the input and output respectively. For single-photon input states, it translates into the probability of the photon being stored and subsequently retrieved. For single-photon level storage, this is very difficult to directly measure for a single process, thus counting statistics of photons recovered from the memory and of photons incident to the memory are accumulated, with their ratio giving the measured efficiency. Less than unit efficiency

corresponds to loss; of which many quantum algorithms are sensitive to and thus it is beneficial for efficiency to be as high as possible.

Fidelity

The fidelity $\mathcal{F}$ of a memory can be considered as the overlap between the input and outputs to the memory and is given by $\mathcal{F} = \left|\mathrm{Tr}(\sqrt{\sqrt{\rho_{in}}\rho_{out}\sqrt{\rho_{in}}})\right|^2$ [68,69] where $\rho_{in/out}$ are the density matrices of the stored/recovered state. A memory can only be considered quantum if it surpassed the maximum recovered fidelity from a classical device. One could imagine a classically stored measurement of the target state, and the preparation of a new state based on the results. This would on average yield a fidelity of $2/3$ [70], hence for a memory to be considered quantum it must exceed this value. This quantum-classical bound derives from the 'measure and prepare' strategy to replicate a quantum state following a single measurement [71].

The fidelity is also closely linked to the **noise** of the retrieved state; for the storage of weak coherent states, the signal to noise ratio (SNR) can be used. One useful metric to compare noise in different memory protocols is the μ_1 [72] which compares both noise and efficiency:

$$\mu_1 = \frac{\langle n_{\mathrm{noise}} \rangle}{\eta_{\mathrm{mem}}} \tag{1.10}$$

where $\langle n_{\mathrm{noise}} \rangle$ is the expectation of the number of noise photons and η_{mem} is the memory efficiency. In the case of single photon storage, this could be thought of as the relative probability of the retrieved photon having come from noise, given a photon was sent into the memory. That is to say with $\mu_1 = 1$, when a single photon is sent into the memory, a photon detected at the output would have been as likely to have come from noise as to be

the retrieved signal.

In the case of true single-photon storage, zero added intensity noise would be the ability to store photons with a second-order correlation $g^{(2)} = 0$ and retrieve them with the same $g^{(2)}$ whilst added phase noise or modification of the state would induce other errors (as a reduction in fidelity manifesting as increased distinguishability between what were previously identical photons).

Lifetime

As the quantum state is held the efficiency with which it can be retrieved will decrease exponentially due to decoherence within the storage medium. In this thesis, we shall define memory lifetime τ_{mem} as the time at which memory efficiency has dropped to $1/e$ of its initial value. For quantum repeater applications, the lifetime must be long enough to both allow photon transmission and perform necessary entanglement swapping operations; typically this is dominated by photon travel time therefore a longer lifetime significantly boosts the possible distance a repeater can operate for.

Bandwidth

The bandwidth σ limits the maximum spectral width of the pulses that could be stored – simultaneously representing the reciprocal of the shortest pulse that could be stored. A large storage bandwidth, therefore, allows for fast performance.

Time-bandwidth product (B)**:** The product of lifetime and bandwidth gives a dimensionless number used to evaluate memory performance. The time-bandwidth product indicates how many pulse-widths a pulse can be delayed by, indicating the number of operations during which the memory can hold the state. An example temporal multiplexing applic-

ation is illustrated in Figure 1.3, which shows the potential reduction in waiting time for a synchronised N-photon event with the inclusion of a quantum memory with $B = 1000$. Time-bandwidth product is the principal figure of merit for this application and demonstrates significant improvement achieved with a relatively modest efficiency. This example displays how memories may be used as a solution to scalability for non-deterministic processes in quantum photonic networks.

Multimodeness

The ability to simultaneously store many optical modes, be them in any of the degrees of freedom described in Section 1.2.2, is described by a memory's multimode capacity. Quantum repeater protocols, generating entanglement between distinct nodes have been shown to gain an N-factor rate enhancement when applied to memories with a multimode capacity equal to N [73]. Whilst historically a high capacity has been typically desired, recently applications for *single-mode* memories have been developed [74]. The Raman protocol described as the focus of this thesis is single-mode and as such the applications of the memory using temporal modes will be described in Chapter 5.

1.3.3 Implementations

There are a number of possible physical systems with which quantum memories can be realised with protocols developed each with its own set of advantages and disadvantages. In this section, I will review the physical processes behind a number of proposals and discuss limitations they may have.

The simplest way one could imagine storing a photon would be simply to extend its optical path length; this is possible in free space [75], a fibre or a cavity [76] where active

switching could be used for retrieval. However, these systems are currently limited by loss (switching loss, fibre loss or intracavity loss) which means that they are not currently suited for application in larger-scale quantum networks[56,77].

To store light in matter requires a strong coupling which can be achieved by the use of a cavity. One could then imagine storage using a transition in an isolated atom[78], this however severely restricts the bandwidth it is possible to store. The other method to increase the coupling is to then use an ensemble of atoms - reducing the technical overhead in fabricating a cavity. In this regime, the signal is stored as a collective excitation of the ensemble.

EIT

The interaction between optical fields and multilevel atoms can lead to quantum interference that can dramatically alter the optical properties of a medium[79]. One such example is the non-linear effect of Electromagnetically Induced Transparency (EIT) where Fano interference between transition pathways creates a transparency window for frequencies surrounding a transition.

This effect can be seen in atoms with a Λ-level energy structure as seen in Figure 1.4 (a) where two ground states ($|1\rangle$ and $|3\rangle$)are coupled to a single excited state ($|2\rangle$). Coupling is achieved by a strong control field and a weak signal (or probe) field. Absorption of the signal can occur by the process $|1\rangle \rightarrow |2\rangle$ and by $|1\rangle \rightarrow |2\rangle \rightarrow |3\rangle \rightarrow |2\rangle$. The amplitudes for these transitions interfere destructively and hence the probe is not absorbed - Figure 1.4 (b). The change in absorption is accompanied by a large change in dispersion, which in-turn results in a dramatic change to the group velocity of the signal $v_g = \mathrm{d}\omega/\mathrm{d}k = c/(n + \omega \mathrm{d}n/\mathrm{d}\omega)$.

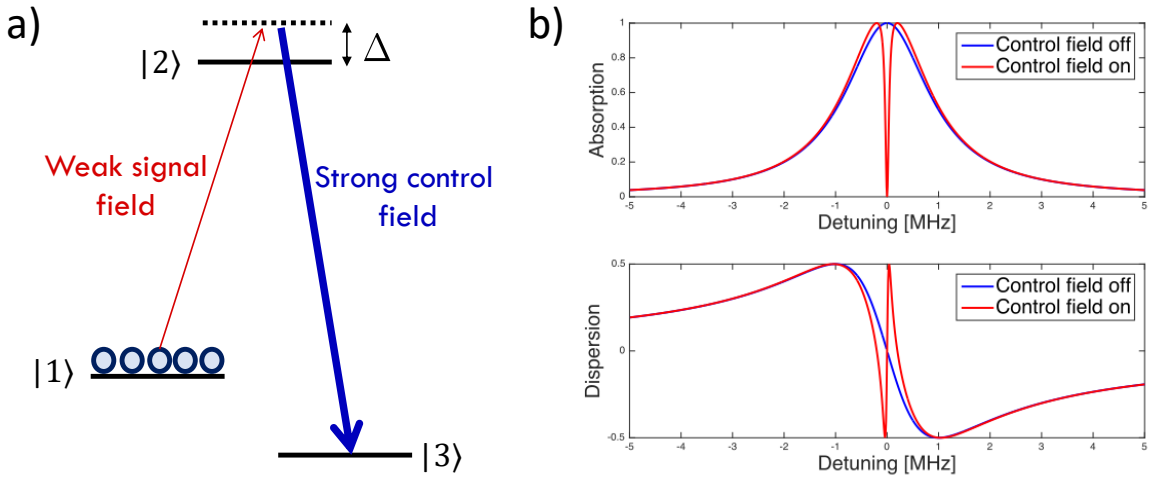

Figure 1.4: (a) Λ energy level structure used in Electromagnetically Induced Transparency with a strong control and weak signal field coupling two ground states to an excited level. (b) Shows the absorption and dispersion as a function of signal detuning from the $|1\rangle \rightarrow |2\rangle$ transition with (red) and without (blue) the bright control field.

To use this process as a memory follows the following procedure:

1. The ensemble of atoms are prepared in the state $|1\rangle$ and the control field is applied. The signal is incident on the ensemble and propagates through (slowly) without loss.

2. The control field is adiabatically reduced to zero, bringing the signal to a halt within the ensemble ($v_g = 0$). The quantum state of the signal is transferred to a ground state coherence (or *spin-wave*) within the ensemble of M atoms with the form:

$$|\Psi\rangle = \sum_{j}^{M} \psi_j e^{i\Delta k z_j} |0_1 0_2 .... 1_j ... 0_M\rangle \tag{1.11}$$

where z_j is the position of the j_{th} atom and Δk is the difference between the wave-vectors of the control and signal fields[80]. The amplitudes ψ_j correspond to the interaction strength the j^{th} atom feels. This represents a spatial hologram across the

ensemble; the excitation encoded across the ensemble of atoms[8].

3. Increasing the control field adiabatically results in the retrieval of the signal from the ensemble.

Using EIT as a memory was first proposed by Fleischhauer and Lukin [81] and was realised by Philips *et al.* the following year [82] using rubidium vapour. Since then it has been developed and implemented using both atomic ensembles [83] and in solid-state media [84]. Significant advancements have been made in increasing the efficiency of EIT memories, with demonstrations exceeding 85% [85] and achieving a time-bandwidth product of 1200 [86] Two key limitations of EIT memories are 1) the possible signal bandwidth; this is typically of order MHz [87] and 2) four-wave mixing noise (the process which is discussed in detail in the following chapter) is inherent to the system, limiting its applications in single-photon storage. There are however proposals to use the orbital angular momentum (OAM) degree of freedom in photons as qubits, and EIT memories have been shown to store photons with OAM, expanding their potential applications in this field [88,89].

Recent investigation of the strong field limit of EIT has provided another memory protocol, **ATS: Autler-Townes Splitting**. Here the transparancy window broadens, and despite the quantum interference inherent to EIT not being present, coherent storage is still possible. This novel memory protocol was demonstrated for the first time in 2019 using a cold atoms rubidium set-up yielding a memory efficiency of 7% and a lifetime of 330 ns [90]. This has subsequently been improved on to an efficiency of 30% with a lifetime of 15 µs with single photon level coherent states [91]. Developing this protocol, potentially extending to warm vapours, is an area of active research.

[8] The concept of the spinwave is explored in detail in Sections 2.4 and 4.2.1.

Raman Memory

The Raman interaction describes the inelastic scattering of a photon from a transition. This linear two-photon process is mediated by a second-order dipole interaction and has two possible outcomes: The scattered photon can have a frequency lower than or greater than the absorbed photon, corresponding to Stokes or anti-Stokes scattered photons respectively.

Like EIT the Raman memory protocol makes use of the Λ level system shown in Figure 1.5 however it differs by the large detuning Δ of both the signal and the control from the excited state $|2\rangle$. The storage process is very similar to that of the EIT protocol but differs with some small subtleties.

1. Again the atomic ensemble is prepared in $|1\rangle$ and the control field and signal field are applied. The control field is detuned from the $|2\rangle \leftrightarrow |3\rangle$ transition by the same amount Δ as the signal is detuned from the $|1\rangle \leftrightarrow |2\rangle$ transition, such that they are in two-photon resonance.

2. The quantum state of the signal is transferred by Raman scattering to the same spin-wave coherence given by equation 1.11. Retrieval of the signal field occurs by the re-application of the control field and the signal is re-emitted as a Stokes photon.

3. Because the signal is not restricted by a transparency window, the signal can can have a much broader spectral profile with its bandwidth limited by only the control's bandwidth and the need to optically address the ground states individually. This is determined by its ground state splitting Δ_g and if the hyperfine levels in the ground-state of Caesium are used as $|1\rangle$ and $|3\rangle$ then $\Delta_g = 9.2\,\mathrm{GHz}$ and the acceptance bandwidth can be of order gigahertz[92].

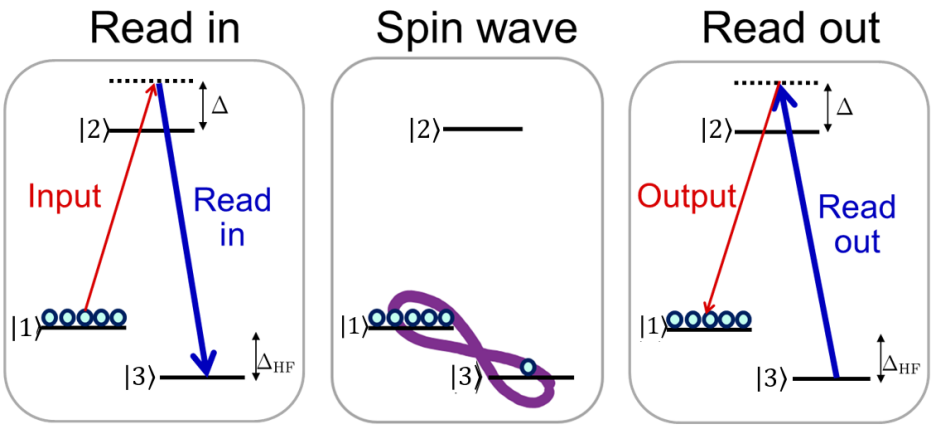

Figure 1.5: Raman Memory Schematic. Energy level arrangement in the Λ-level system where we will use the hyper-fine splitting Δ_{HF} in Caesium for the two ground states. The Raman memory protocol uses a strong control field to drive a Raman transition and store an input signal field as a coherence across an atomic ensemble, or spin-wave. Application of a subsequent control pulse *reads-out* the excitation, and the stored signal is re-emitted.

The GHz possible bandwidth stored in the Raman memory combined with the possible storage time of greater than microseconds yields a time-bandwidth product > 1000, meeting the requirement discussed above for temporal multiplexing. The Raman memory protocol was first demonstrated in 2009 [93] with a bandwidth of 1.2GHz and total efficiency of 15%. A complete discussion of previous experiments using the Raman memory in Caesium will be discussed in Section 2.6 but implementations have seen $B \sim 4000$ and noise suppressed to a level almost allowing single-photon storage whilst maintaining its quantum statistics. Discussions of noise suppression in this memory implementation with hot caesium vapour will form much of the following chapters. Other significant results of the Raman protocol come from the storage of THz bandwidth photons in molecules [94] and bulk diamond [95] which demonstrate the capacity of the Raman protocol to store high bandwidth photons although the memory lifetime is prohibitively short in these demonstrations ($\sim$1ns in hydrogen molecules, $\sim$ 3.5ps in diamond).

In the Raman memory the un-stored signal is not absorbed (because it is so far detuned)

but rather transmitted. This combines with the description of the Raman memory by way of a beam-splitter Hamiltonian:

$$\mathcal{H}_{BS} = C_s \hat{s}\hat{b}^\dagger + h.c. \qquad \text{where} \quad C_s \propto \sqrt{N}\left(\frac{\Omega}{\Delta}\right). \tag{1.12}$$

Here $\hat{s}, \hat{b}$ are annihilation operators for the signal and spin-wave coherence respectively. C_s is the coupling constant for the Raman interaction which is proportional to: the Rabi frequency of the control (Ω), the square root of the number of atoms in the interaction, N, and inversely proportional to the detuning Δ. The memory process may then be thought of as two successive light-matter beam splitters where the read-in and read-out efficiencies correspond to reflectivities - a correspondence that has potentially novel applications since beam splitters play such an instrumental role within LOQC.

ORCA/FLAME

Akin to the Raman memory procotol are the memory protocols ORCA and FLAME: *off resonant cascaded absorption* and *fast ladder memory.* The mechanism of these memories is very similar to the Raman memory, however the storage state $|3\rangle$ is above the intermediate state. The excitation is thereby stored in an excited electron state; which naturally has a short lifetime. Additionally the wavelength of the spatial hologram created by the excitation is very short ($\sim$ µm), and so atomic motion in warm vapour further restricts the lifetime – the demonstrated lifetimes have been only 5 ns in caesium and 86 ns in rubidium. These memory protocols are in their infancy having been designed in 2018 and research is ongoing to, for example, implement ORCA in cold atoms. The protocol is demonstrably noise free, shown to retrieve a single photon with no discernable change to the $g^{(2)}$. Furthermore,

fast repetition rates can in principle be achieved as the bandwidth limit imposed by the ground-state splitting in lambda-type systems is non-existent and perfect initialisation is often achievable without the need for pumping. The operating wavelength and GHz broad acceptance bandwidth of both the Raman and ladder schemes make them well matched for inferfacing current quantum dot sources[74,96].

Photon-Echo Memories

EIT and the Raman protocol form two sides of the same coin - Λ-level schemes in which the signal is mapped adiabatically to a spin-wave coherence without the upper level ever being populated. There do exist a number of alternative memory protocols that borrow from the Hanh echoes used in NMR[97] - these are *Photon-Echo Memories*. The principle behind it is simple: a $\pi/2$ signal pulse is applied to a system of 2 level atoms initialised in the ground state $|0\rangle$. The result is a coherent superposition to the state:

$$|\psi\rangle = \frac{1}{\sqrt{2}}(|0\rangle + e^{i\phi}|1\rangle) \tag{1.13}$$

In practice however this process will suffer from some inhomogeneous broadening which could be from a velocity distribution in warm vapours or strain fields in solid states, all atoms will dephase at a different rates resulting (after time τ) in the state:

$$|\psi\rangle = \sum_{j}^{N}(e^{i(\delta_j\tau+\phi)}|0_1 0_2 ....1_j ...0_N\rangle) \tag{1.14}$$

where δ_j the difference in detuning felt by each atom labelled by j. If a π pulse is then applied and the atoms dephase after a further time τ then the dephasing already experienced

is effectively cancelled and results in only a global phase. This re-phasing causes an *echo*, and the signal is re-emitted as the atoms return to the ground state.

$$|\psi\rangle \xrightarrow{\pi\ pulse} \sum_j \frac{1}{\sqrt{2}}(e^{i(\delta_j\tau+\phi)}|0\rangle + |1\rangle) \xrightarrow{t=\tau} \sum_j \frac{e^{i\delta_j\tau}}{\sqrt{2}}(e^{i\phi}|0\rangle + |1\rangle) \xrightarrow{signal} |0\rangle \tag{1.15}$$

The process described above is a Hanh-echo scheme from NMR and can apply in photonics, however in the context of single-photon storage a significant issue occurs. A single-photon in general will not perform the required $\pi/2$ rotation, hence after absorption there is only a small amplitude in the upper state $|\psi\rangle = \cos(\alpha)|0\rangle + e^{i\phi}\sin(\alpha)|1\rangle$ where α is small. This means after the π pulse the upper-state has a large amplitude ($\cos(\alpha)$) and hence a significant probability of spontaneous decay. Consequently, the π pulse is not well suited to photonic memories[98] and it is therefore preferable to manipulate the re-phasing via control of the broadening process, resulting in a number of proposals summarised below.

Controlled and Reversible Inhomogeneous Broadening (CRIB) and Gradient Echo Memories (GEM) are schemes where an inhomogeneous broadening to the $|1\rangle \leftrightarrow |2\rangle$ transition is achieved by applying an electric or magnetic field which induces a Stark or Zeeman splitting. For example, in CRIB the state of the ensemble of M atoms involved in the interaction after absorbing the signal is:

$$|\psi\rangle = \sum_j \psi_j e^{i\delta_j t} e^{ikz_j} |0_1..1_j...0_M\rangle \tag{1.16}$$

where k is the wavevector of the signal and δ_j is again the detuning felt by the j^{th} atom caused by a transverse field. Here, as the dephasing is due to the external field, by reversing the direction of the applied field after time τ changes the sign of the detuning felt by each atom and hence the signal is re-emitted by the echo. GEM differs from CRIB in the direction

of the field gradient, where it is applied along the direction of propagation of the signal. This causes the detuning to vary across the sample, essentially encoding the frequencies of the signal to a spatial location. This prevents re-absorption during the read-out phase, maximising (read-out) efficiency.

The final photon-echo method discussed is most similar to CRIB but with some subtleties where it "burns" spectral holes into an inhomogeneously broadened transition to create an Atomic Frequency Comb (AFC). In contrast to CRIB however the inhomogeneous broadening does not have to be reversible, it can be due to (for example) the broadening experienced in rare-earth-doped crystals[99]. The result of this is the creation of a set of energy levels equally spaced by Δ (see Figure 1.6 (c)) that induce dephasing which (like in CRIB) must be re-phased to re-emit the signal. Unlike CRIB, however, because of the periodic nature of the energy spacing, re-phasing will occur (periodically) after a time $(2\pi/\Delta)$ without any change in fields.

The benefit of AFC compared to CRIB is in the ability to make use of inhomogeneous broadenings which are unsuitable for CRIB. In CRIB atoms not in a narrow resonance need to be removed from the interaction by optical pumping, whilst in AFC they need to be removed from not being in N narrow resonances which spans much fewer atoms. It is important to note that AFC in two levels cannot be read-out on demand without modification. This might be via the inclusion of a third level using the Λ configuration. The excitation may then be mapped to the third level just as in EIT and Raman memories to increase storage time and allow on-demand retrieval for AFC. The mapping to the third level is the same, transfer is completed with a bright control pulse, as shown in Figure 1.6. Other schemes to provide on demand read-out from AFC's include using both the

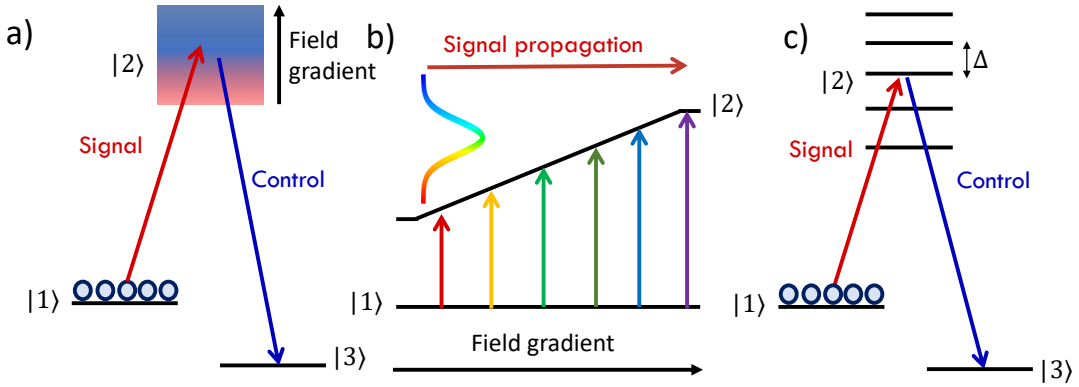

Figure 1.6: Energy level structure for the read-in procedures of a) CRIB b) GEM and c) AFC. In CRIB and GEM the field gradient applied must be reversed for read-out whilst this is not the case in AFC. For these protocols the signal bandwidth should be matched to the now broadened transition, shown explicitly in b).

linear[100,101] and AC-Stark effect[102]. To date AFC memory protocols have been used to store qubits using the polarisation[103–105], time-bin[106] and orbital angular momentum[107] degrees of freedom as well as storing photons from both quantum dot[108] and PDC[109] sources. Large multimode capacity (>130 modes stored) has also been demonstrated[110,111] as have efficiencies in excess of 55%[112],

It is interesting to consider the relationship between optical depth and multi-modality. In 2008, Nunn *et al.* calculated the scaling between optical depth d (proportional to interaction strength) and mode capacity[113]. They applied this comparison across the memory protocol listed and found that for protocols without an inhomogeneous broadening (e.g. Raman, ORCA) the capacity scaled with $\sqrt{d}$ whilst for CRIB and GEM the scaling was a significantly more favourable linear scaling with d. For AFC they found the mode capacity was independent of optical depth, provided a certain threshold was met.

DLCZ

The final implementation of a memory protocol was touched briefly on in Section 1.3.1 and is distinct from the others in that the memory storage is heralded by the emission of a photon. The scheme also provides a natural way for entanglement to be transferred to spatially separated nodes - the constituent part for a quantum repeater and was conceived by Duan, Lukin, Cirac and Zoller in 2001 [114]. The so-called DLCZ protocol makes use of the Raman scattering seen in an atomic ensemble (Figure 1.5) except that in this case the write pulse is bright, and emits a Stokes photon which heralds the storage of the excitation. Read-out is then achieved with a resonant pulse and the *signal* is re-emitted as an anti-Stokes photon. Note this *signal* should not be thought of in the same way as the signal in the previous memories - in this case, it is a herald that the excitation is no longer present.

Figure 1.7 (c) shows how this scheme may then produce a Bell-like state: applying write pulses to two ensembles A and B and having their heralded Stokes photons incident on a beam-splitter combined with a single detection event would produce the state $|\psi\rangle_{AB} = \frac{1}{\sqrt{2}}(|0\rangle_A |1\rangle_B + |1\rangle_A |0\rangle_B)$ where $|1\rangle_J$ and $|0\rangle_J$ represent if ensemble J is storing an excitation or not.

The natural extension of this is to combine two of these Bell states, as done previously in Figure 1.2. We start with two pairs ($AB\&CD$) of entangled atom ensembles:

$$\begin{aligned} |\psi\rangle_{ABCD} &= \frac{1}{\sqrt{2}}(|0\rangle_A |1\rangle_B + |1\rangle_A |0\rangle_B) \otimes \frac{1}{\sqrt{2}}(|0\rangle_C |1\rangle_D + |1\rangle_C |0\rangle_D) \\ &= \frac{1}{2}(|0101\rangle + |0110\rangle + |1001\rangle + |1010\rangle) \end{aligned} \tag{1.17}$$

Simultaneous read-pulses onto the ensembles B and C are applied with the output anti-

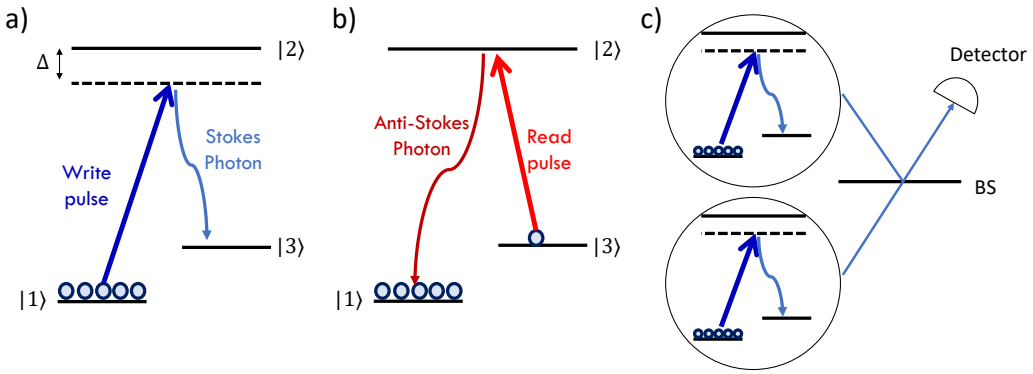

Figure 1.7: a) Energy level structure for the read-in and b) read-out Raman scattering interaction in the DLCZ protocol. c) Entanglement is created between two ensembles by having the emitted Stokes photon incident on a beam-splitter: a single detection event places creates a superposition of the excitation being in the top ensemble or the bottom.

Stokes photons incident on a beam-splitter and two detectors. A single detection result signifies that one ensemble has been read-out but gives no information as to which one - this can be thought as a projection onto the subspace: $\frac{1}{\sqrt{2}}(|0\rangle_B |1\rangle_C + |1\rangle_B |0\rangle_C)$ which results in:

$$|\psi\rangle_{AD} = \frac{1}{\sqrt{2}}(\langle 01|_{BC} + \langle 10|_{BC})\,|\psi\rangle_{ABCD} \tag{1.18}$$

$$= \frac{1}{\sqrt{2}}(|0\rangle_A |1\rangle_D + |1\rangle_A |0\rangle_D) \tag{1.19}$$

Hence a Bell-state has been created between (in principle) spatially separated ensembles A and D (note the normalisation factor in equation 1.18 has been omitted). This is precisely the operation desired in Section 1.3.1, and could form the basis of a quantum repeater network[115] with an impressive demonstration in cold rubidium that had an efficiency of 76% and a storage lifetime of 0.22 s[116]. It is important to note this is a memory scheme where the memory stores information of a quantum excitation as opposed to a quantum state in question. This means that whilst the DLCZ protocol can be used for the synchronisation

of photon sources (using the single photons inherent to the protocol), it cannot be used to store the output of logical operations performed by linear optics (for example in LOQC applications).

1.4 Thesis Outline

This thesis predominantly focuses on implementing the Raman memory protocol in warm vapour, with particular emphasis on the inherent noise process of four wave mixing. Chapter 2 describes the theory of the memory interaction, advancing the initially derived equations of motion with the addition of an extra field, generated by anti-Stokes scattering. Chapter 3 discusses how photon statistics may be used to divine information about noise within a low-photon number state. This yields a tool we can use to quantify the different noise mechanisms that exist within the memory. This is then utilised in Chapter 4 where a novel noise suppression scheme is implemented and proven to eradicate four-wave mixing noise and suggests the protocol is capable of faithfully retrieving a single photon state. This then enables a discussion of an exciting application of the memory using temporal modes in Chapter 5. Chapter 6 also discusses how the ORCA memory can be applied to temporal modes and suggests a method to lengthen the storage time. This method involves selectively pumping a single velocity class in order to suppress Doppler dephasing. By selecting multiple velocity classes we show for the first time that an AFC memory can be created in warm vapour, and posit the combination of the AFC and ORCA protocol. Chapter 7 considers the outlook of the work presented here and suggests future experiments given the removal of noise from our implementation of the Raman protocol.

Chapter 2

Theory of the Raman quantum memory

> "Protons give an atom its identity, electrons its personality."
>
> Bill Bryson, *A short history of nearly everything*

In this chapter, I present a theoretical derivation of the Raman quantum memory, following the framework developed by J.N. Here, I expand on the derivation in part by introducing an additional field to describe a noise process inherent to the protocol, and also by deriving Green's functions that completely describe the memory interaction. Whilst the light-matter interaction surrounding this specific interaction has been studied for over a decade, I am responsible, during the course of my DPhil research, for developing the equations of motion such to include the noise process caused by four-wave mixing.

2.1 Introduction

The Raman memory protocol is based on an off-resonant two-photon Raman transition in an ensemble of atoms with a Λ energy level configuration. The system is prepared in one of the hyperfine ground state levels $|1\rangle$ via optical pumping.

Then, to "write" a photon to the memory, a strong, co-propagating control pulse is used to drive a Raman transition between the ground state levels $|1\rangle \rightarrow |3\rangle$; detuned from resonance with the excited level $|2\rangle$ by Δ_{HF}. This is shown in Figure 2.1.

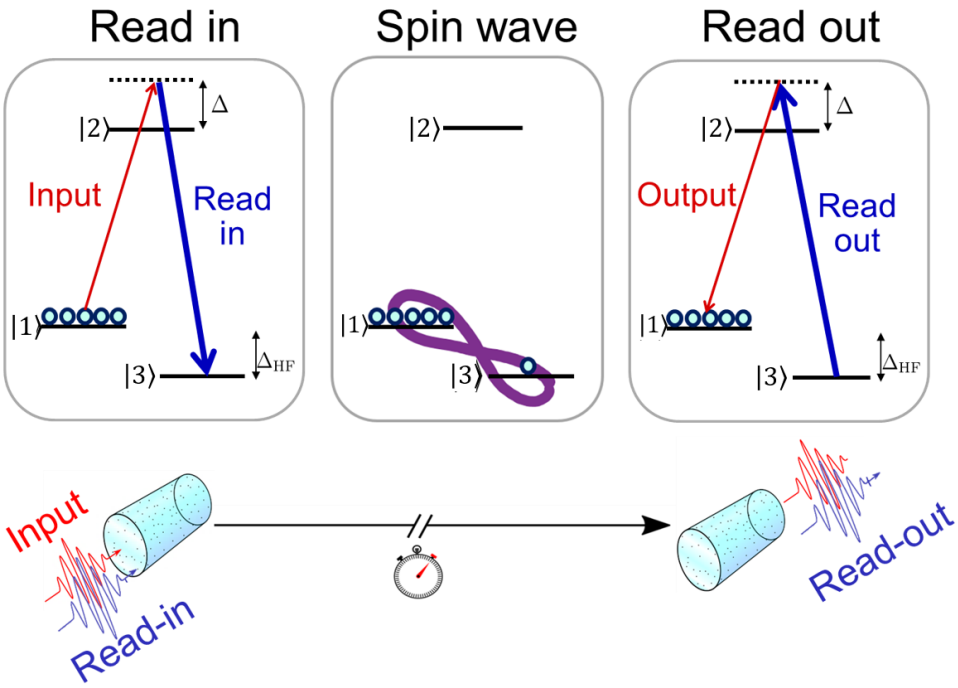

Figure 2.1: Raman Memory Schematic. (a) Energy level arrangement in the Λ-level system where we will use the hyper-fine splitting Δ_{HF} in Caesium for the two ground states. The Raman memory protocol uses a strong control field to drive a Raman transition and store an input signal field as a coherence across an atomic ensemble, or spin-wave. Application of a subsequent control pulse *reads-out* the excitation, and the stored signal is re-emitted.

The result of this interaction is that the input signal field is stored as a collective ground state coherence, or spin-wave, across the entire ensemble. In an atomic ensemble the storage takes the form of an entangled super-position of states[1] in which one[2] spin is flipped. The photonic state is then "read" from the memory, on demand, by again applying another control pulse and driving the system back to the original state with the emission of the signal state.

[1] Shown explicitly in Section 2.4
[2] At the most one when storing a single photon, possibly more if the input state contains more photons.

The off-resonant nature of the Raman memory means that the memory protocol 1) is insensitive to inhomogeneous broadening of the excited state, and 2) can be operated at ambient temperatures without the need for cryogenics or complex atomic cooling and trapping techniques. Furthermore, the bandwidth of the signal that can be stored is determined by the bandwidth of the control field, and not the atomic transition, thus the protocol can store very broadband signals although it ultimately limited by the ground-state splitting. The spin-wave excitation is moderately long-lived (microsecond storage relative to GHz bandwidth photons) and therefore the Raman memory exhibits a very high time-bandwidth product, making it an ideal candidate for temporal multiplexing applications.

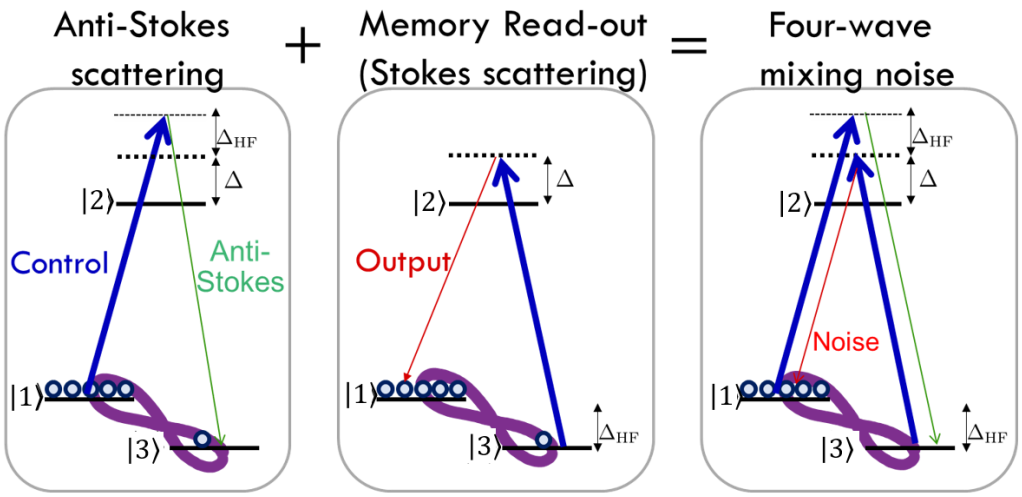

Figure 2.2: Energy level arrangement showing how four-wave mixing leads to noise. The control experiences anti-Stokes scattering, producing an anti-Stokes photon and corresponding coherence (spin-wave). This spurious excitation is then *read out* during the regular read-out interaction, adding noise at the signal mode.

2.1.1 Noise: Four-wave mixing

Spontaneous: As shown in Figure 2.2 there is another way in which the control field can interface with the atoms (as will be described fully in the following section). The strong

control field can couple to the populated ground state and spontaneously anti-Stokes scatter. The result of this scattering is the possibility of flipping a spin from $|1\rangle \rightarrow |3\rangle$. Whilst this process in itself doesn't generate noise[3], the flipped spin can spontaneously scatter a Stokes photon when the read-out control pulse is applied; a Stokes photon which is in the same spatial, temporal and frequency mode as a photon that had been written to the memory via the intended storage transition. This photon is therefore indistinguishable to any retrieved signal, and thus adds noise, corrupting the stored/retrieved quantum state.

Gain: We must think very carefully about what exactly we mean when discussing noise. The spontaneous noise is easy to spot, one simply applies a control pulse and places a detector on the signal mode. The detector records any spontaneous signal produced by four wave mixing. If multiple control pulses are applied then we can see an increase in detected signal despite no input - this is caused by build up of now un-pumped spins in the storage state $|3\rangle$, which can spontaneously Stokes scatter light into the signal mode. In Section 2.3.2 we shall derive a tool to examine the statistical properties of the light emitted by the atoms, and we shall see not only these noise terms but an additional *gain* process dependent on the size of the signal[4] which generates an additional spin-wave in the atoms. The implication of this spurious spinwave is damning. Inherent to the memory is a process that generates noise which is identical to the stored signal in frequency and spatial mode but will pollute any quantum statistics that the retrieved signal may have otherwise had. From this it is clear that this noise cannot be simply filtered away, the underlying process behind it must be stopped.

In the configuration presented, the detuning for this anti-Stokes process is greater than

[3]It does generate anti-Stokes photons, but these can be filtered relatively simply.
[4]This is exactly the process of a four-wave mixing laser.

for the desired process, so the FWM coupling is suppressed with respect to the target memory write/read transitions. Despite this, the noise from this process has been demonstrated to be prohibitively high for the storage of single photons [92], and furthermore, as we will show in the following sections, it is an intrinsic part of the memory Hamiltonian. Therefore, it must be eliminated during the memory interaction in order for the warm vapour caesium ensemble to be a useful quantum memory. It should be noted that four-wave-mixing satisfies energy and momentum conservation, and due to the difference in detuning from the atomic resonances, the three fields will experience different dispersion - a fact we will make use of in Chapter 4 when looking at an approach to reduce this noise process.

2.2 Equations of Motion

A theoretical description of the Raman memory interaction was first laid out by Kozhekin *et al* [117] and later expanded on by Gorshkov [118] and Nunn [119]. The derivation below follows closely that from [119–121] as the theory has developed to more completely describe the interactions.

We consider an ensemble of atoms with a Λ-energy level configuration with two ground eigenstates $|1\rangle$ and $|3\rangle$, transitions between which are electric-dipole forbidden. Each are coupled to an excited state $|2\rangle$, as shown in Figure 2.1. This simple configuration is host to a number of non-linear optical phenomena, including EIT, ATS and stimulated Raman adiabatic passage (STIRAP) [90,122–124].

Once we have found an expression for the light-matter Hamiltonian, we can establish the dynamical equations which govern the atomic evolution. The propagation of the signal field through the atomic ensemble can be determined from Maxwell's equations. By defining

continuous atomic operators for the atomic polarisation and spin wave, we finally arrive at the equations of motion which describe the macroscopic behaviour of the Raman memory.

2.2.1 Light-matter Hamiltonian

The complete Hamiltonian for the light-matter system can be written as the sum of the following contributions:

$$\hat{H} = \hat{H}_A + \hat{H}_L + \hat{H}_{\mathrm{ED}}, \tag{2.1}$$

where $\hat{H}_A$ is the Hamiltonian for an atom in the ensemble, $\hat{H}_L$ is the free field Hamiltonian for the light fields, and the interaction Hamiltonian, $\hat{H}_{\mathrm{ED}}$, describes the electric dipole interaction. The first of these can be diagonalised by expressing $\hat{H}_A$ in terms of its eigenstates $|1\rangle, |2\rangle$, and $|3\rangle$:

$$\hat{H}_A = \sum_{j=1}^{3} \hbar\omega_j \, |j\rangle\langle j| = \sum_{j=1}^{3} \hbar\omega_j \, \hat{\sigma}_{jj} \tag{2.2}$$

where ω_j is the resonant frequency of eigenstate $|j\rangle$ and $\hat{\sigma}_{jk} = |j\rangle\langle k|$. The diagonal elements $\hat{\sigma}_{jj}$ describe the atomic populations in each energy level whilst the off-diagonal elements $\hat{\sigma}_{j\neq k,k}$ capture the coherences between them.

The free-field, radiative Hamiltonian H_L describes excitations of the electromagnetic field and is given by:

$$\hat{H}_L = \int_0^\infty \mathrm{d}\omega \hbar\omega \hat{a}^\dagger(\omega)\hat{a}(\omega) \tag{2.3}$$

Here, the zero-point energy has been ignored and $\hat{a}(\omega), \hat{a}^\dagger(\omega)$ are the annihilation and creation operators for a photon with frequency ω, respectively.

The final contribution to the total Hamiltonian stems from the electric-dipole interaction described by $\hat{H}_{ED} = -e\hat{\mathbf{E}} \cdot \hat{\mathbf{d}}$ where $\hat{\mathbf{E}}$ is the electric field operator and $\hat{\mathbf{d}}$ represents the

dipole operator.

2.2.2 Optical fields

The bright control field with central frequency ω_c can be expressed classically as:

$$\mathbf{E}_c(t,z) = \mathbf{v}_c E_c(t,z) e^{i\omega_c(t-z/c)} + c.c., \tag{2.4}$$

where $t - z/c$ is the retarded time in a moving frame of reference and $\mathbf{v}_c$ is the polarisation vector of the control field. In this derivation we assume the beam to have low divergence over the interaction region allowing the slowly varying amplitude $E_c(t,z)$ to be confined to one-dimensional propagation.

We must however describe the signal field quantum mechanically. Using the Bosonic annihilation operator $\hat{a}(w,t)$, the signal field is given by:

$$\hat{\boldsymbol{E}}_s(z,t) = i\mathbf{v}_s \int \mathrm{d}\omega g(\omega) \hat{a}(\omega,t) e^{-i\omega z/c} + h.c., \tag{2.5}$$

where $\mathbf{v}_s$ is the signal polarisation vector and $g(\omega) = \sqrt{\hbar\omega/4\pi\epsilon_0 c\mathcal{A}}$ is the signal mode amplitude with transverse mode area $\mathcal{A}$. Assuming that the spectral width of the signal pulse is small compared to its central frequency ω_s, we can neglect the frequency dependence of the mode amplitude and re-write the signal as:

$$\hat{\boldsymbol{E}}_s(z) = i\mathbf{v}_s \hat{S}(t,z) e^{i\omega_s(t-z/c)} + h.c. \tag{2.6}$$

Here $g_s = \sqrt{2\pi}g(\omega_s)$ and $\hat{S}$ is the annihilation operator in the time domain[5] which can be identified as the mode amplitude of the signal:

$$\hat{S}(t,z) = e^{-i\omega_s(t-z/c)} \times \frac{1}{\sqrt{2\pi}} \int \mathrm{d}\omega \hat{a}(\omega,t) e^{-i\omega z/c} \tag{2.7}$$

where we have made two further approximations. Firstly, the slowly varying envelope (SVE) approximation where we assume the signal propagation is determined by the slow temporal evolution of $\hat{S}$, whilst the exponential factor represents the rapidly oscillating carrier wave. This approximation is valid if the pulse duration is much greater than the optical period $2\pi/\omega_s$. Secondly, we again make the paraxial approximation assuming the signal propagates along the z-axis with negligible divergence.

2.2.3 The dipole interaction

The dipole operator $\hat{\mathbf{d}}$ from $\hat{H}_{ED} = -e\hat{\mathbf{E}} \cdot \hat{\mathbf{d}}$ can be expressed in terms of matrix elements as

$$\hat{\mathbf{d}} = \sum_{j,k} \langle j | \hat{\mathbf{d}} | k \rangle \hat{\sigma}_{jk} = \sum_{j,k} \mathbf{d}_{jk} \hat{\sigma}_{jk} \tag{2.8}$$

Since the electric dipole interaction has odd parity, only the off-diagonal elements of the dipole operator are non-zero[125]. We can further simplify the operator by forbidding transitions between the two ground states $|1\rangle$ and $|3\rangle$. Under these considerations, the dipole operator is given by:

$$\hat{\mathbf{d}} = \mathbf{d}_{12}\hat{\sigma}_{12} + \mathbf{d}_{23}\hat{\sigma}_{23} + h.c. \tag{2.9}$$

[5] We will re-encounter this operator when discussing that photon statistics properties of the memory in Section 2.3.2

2.2.4 Optical Bloch equations

We can now use the Heisenberg equation of motion to derive the equations that describe the evolution of the atoms. We note first that the free field Hamiltonian commutes with $\hat{\sigma}_{jk}$:

$$\partial_t \hat{\sigma}_{jk} = i[\hat{\sigma}_{jk}, \hat{H}_A + \hat{H}_L + \hat{H}_{\mathrm{ED}}] = i[\hat{\sigma}_{jk}, \hat{H}_A + \hat{H}_{\mathrm{ED}}]. \tag{2.10}$$

This results in a set of coupled differential equations that describe the dynamics of the atomic populations $\hat{\sigma_{jj}}$ and the atomic coherences $\hat{\sigma}_{j\neq k,k}$.

$$\begin{aligned}
\partial_t \hat{\sigma}_{11} &= -i\boldsymbol{E} \cdot [\boldsymbol{d}_{12}\hat{\sigma}_{12} + h.c.] \\
\partial_t \hat{\sigma}_{33} &= +i\boldsymbol{E} \cdot [\boldsymbol{d}_{23}\hat{\sigma}_{23} + h.c.] \\
\partial_t \hat{\sigma}_{12} &= i\omega_{21}\hat{\sigma}_{12} - i\boldsymbol{E} \cdot [\boldsymbol{d}^*_{12}(\hat{\sigma}_{11} - \hat{\sigma}_{22}) + \boldsymbol{d}_{23}\hat{\sigma}_{13}] \\
\partial_t \hat{\sigma}_{13} &= i\omega_{31}\hat{\sigma}_{13} - i\boldsymbol{E} \cdot [\boldsymbol{d}^*_{23}\hat{\sigma}_{12} - \boldsymbol{d}^*_{12}\hat{\sigma}_{23}] \\
\partial_t \hat{\sigma}_{23} &= i\omega_{32}\hat{\sigma}_{23} - i\boldsymbol{E} \cdot [\boldsymbol{d}^*_{23}(\hat{\sigma}_{22} - \hat{\sigma}_{33}) - \boldsymbol{d}_{12}\hat{\sigma}_{13}]
\end{aligned} \tag{2.11}$$

where $\omega_{jk} = \omega_j - \omega_k$. An additional constraint is imposed by the normalisation condition $\sum_j \hat{\sigma_{jj}} = \mathbb{1}$ giving $\partial_t \hat{\sigma_{22}} = -\partial_t(\hat{\sigma}_{11} + \hat{\sigma}_{33})$.

The coupling of the control field to the $|1\rangle \leftrightarrow |2\rangle$ transition via the $\boldsymbol{d}_{12}\cdot\boldsymbol{v}_c$ terms produces an additional light field via anti-Stokes scattering and in doing so, generates coherence in $\hat{\sigma_{32}}$. Here is the origin of the FWM noise term mentioned previously and assumed to be negligible in the initial derivation [119]. This interaction is detuned by $\Delta_+ = \Delta + \Delta_{\mathrm{hf}}$, and we hence also need to consider a quantum mechanical anti-Stokes field at the frequency

$\omega_a = \omega_c + \omega_{13}$:

$$\hat{\boldsymbol{E}}_a = i\boldsymbol{v}_a g_a \hat{A}(t,z) e^{i\omega_a(t-z/c)} + h.c. \tag{2.12}$$

A number of approximations can be applied to simplify these equations. First of all, the atomic populations can be assumed to be constant in time ($\partial_t \hat{\sigma}_{jj} = 0$), which is true provided that the number of atoms far exceeds the number of photons stored in the memory[6]. We can replace the population operators $\hat{\sigma}_{jj}$ with their expectation values: $\hat{\sigma}_{11} \to (1-\alpha) \approx 1$, $\hat{\sigma}_{22} \to 0$, and $\hat{\sigma}_{33} \to \alpha \approx 0$. Here $(1-\alpha)$ is the average proportion of atoms in the initial state $|1\rangle$, or the optical pumping efficiency, and $\alpha \neq 0$ accounts for imperfect initialisation of the atomic ensemble.

The atomic coherences can be expressed in the rotating frame through the following transformation: $\tilde{\sigma}_{jk} = \hat{\sigma}_{jk} e^{i\omega_{jk}\tau}$. This yields:

$$\begin{aligned} \partial_t \hat{\sigma}_{jk} &\to \partial_t \left(e^{-i\omega_{jk}\tau} \tilde{\sigma}_{jk} \right) \\ &= -i\omega_{jk} e^{-i\omega_{jk}\tau} \tilde{\sigma}_{jk} + e^{-i\omega_{jk}\tau} \partial_t \tilde{\sigma}_{jk} \end{aligned}$$

where $\tau = t - z/c$ is the retarded time. From here on, operators in the rotating frame will be marked with a tilde[7]. Inserting the expression for the electric field $\hat{\mathbf{E}}$ into the equations of motion reveals terms which oscillate rapidly at frequencies given by the sum of the optical and resonant frequencies. Applying the rotating-wave approximation, these terms can be neglected if the detuning Δ of the fields from the excited state $|2\rangle$ is sufficiently

[6] Typically the number of atoms in the ensemble is of order $\mathcal{O}(10^{12})$.
[7] Operators will not be labelled with a hat as well as a tilde to avoid clutter

small compared to the optical frequencies. These approximations result in:

$$\partial_\tau \tilde{\sigma}_{12} = -i\boldsymbol{E}\cdot\left((1-\alpha)\boldsymbol{d}_{12}^{*}\mathrm{e}^{-i\omega_{21}\tau} + \boldsymbol{d}_{23}\tilde{\sigma}_{13}\mathrm{e}^{-i\omega_{23}\tau}\right) \tag{2.13}$$

$$\partial_\tau \tilde{\sigma}_{13} = -i\boldsymbol{E}\cdot\left(\boldsymbol{d}_{23}^{*}\tilde{\sigma}_{12}\mathrm{e}^{i\omega_{23}\tau} - \boldsymbol{d}_{12}^{*}\tilde{\sigma}_{23}\mathrm{e}^{-i\omega_{21}\tau}\right) \tag{2.14}$$

$$\partial_\tau \tilde{\sigma}_{23} = +i\boldsymbol{E}\cdot\left(\alpha\boldsymbol{d}_{23}^{*}\mathrm{e}^{i\omega_{23}\tau} + \boldsymbol{d}_{12}\tilde{\sigma}_{13}\mathrm{e}^{i\omega_{21}\tau}\right). \tag{2.15}$$

We write the electric field as

$$\begin{aligned}\boldsymbol{E} &= \boldsymbol{E}_c + \hat{\boldsymbol{E}}_s + \hat{\boldsymbol{E}}_a \\ &= \boldsymbol{c}\mathrm{e}^{i\omega_c\tau} + \boldsymbol{s}\mathrm{e}^{i\omega_s\tau} + \boldsymbol{a}\mathrm{e}^{i\omega_a\tau} + h.c.\end{aligned} \tag{2.16}$$

where we have defined $\boldsymbol{c} = E_c(t,z)\boldsymbol{v}_c$, $\boldsymbol{s} = ig_s\hat{S}(t,z)\boldsymbol{v}_s$ and $\boldsymbol{a} = ig_a\hat{A}(t,z)\boldsymbol{v}_a$. We substitute Equation 2.16 into Equations 2.13 – 2.15, and only keep the slowly oscillating terms $\pm(\omega_{ij} - \omega_{c,s,a})$ as per the rotating wave approximation. We define the detuning from resonance as $\Delta = \omega_s - \omega_{21}$, such that Δ is positive for a blue detuned signal. The ground state splitting is given by $\Delta_{\mathrm{hf}} = \omega_{13}$. This gives:

$$\begin{aligned}\partial_\tau \tilde{\sigma}_{12} &= -i(1-\alpha)\boldsymbol{d}_{12}^{*}\cdot\left[\boldsymbol{s}e^{i\Delta\tau} + \boldsymbol{c}e^{i(\Delta+\Delta_{\mathrm{hf}})\tau} + \boldsymbol{a}e^{i(\Delta+2\Delta_{\mathrm{hf}})\tau}\right] \\ &\quad - i\tilde{\sigma}_{13}\boldsymbol{d}_{23}\cdot\left[\boldsymbol{s}e^{i(\Delta-\Delta_{\mathrm{hf}})\tau} + \boldsymbol{c}e^{i\Delta\tau} + \boldsymbol{a}e^{i(\Delta+\Delta_{\mathrm{hf}})\tau}\right]\end{aligned} \tag{2.17}$$

$$\begin{aligned}\partial_\tau \tilde{\sigma}_{13} &= -i\tilde{\sigma}_{12}\boldsymbol{d}_{23}^{*}\cdot\left[\boldsymbol{s}^{\dagger}e^{-i(\Delta-\Delta_{\mathrm{hf}})\tau} + \boldsymbol{c}^{*}e^{-i\Delta\tau} + \boldsymbol{a}^{\dagger}e^{-i(\Delta+\Delta_{\mathrm{hf}})\tau}\right] \\ &\quad + i\tilde{\sigma}_{23}\boldsymbol{d}_{12}^{*}\cdot\left[\boldsymbol{s}e^{i\Delta\tau} + \boldsymbol{c}e^{i(\Delta+\Delta_{\mathrm{hf}})\tau} + \boldsymbol{a}e^{i(\Delta+2\Delta_{\mathrm{hf}})\tau}\right]\end{aligned} \tag{2.18}$$

$$\begin{aligned}\partial_\tau \tilde{\sigma}_{23} &= +i\alpha\boldsymbol{d}_{23}^{*}\cdot\left[\boldsymbol{s}^{\dagger}e^{-i(\Delta-\Delta_{\mathrm{hf}})\tau} + \boldsymbol{c}^{*}e^{-i\Delta\tau} + \boldsymbol{a}^{\dagger}e^{-i(\Delta+\Delta_{\mathrm{hf}})\tau}\right] \\ &\quad + i\tilde{\sigma}_{13}\boldsymbol{d}_{12}\cdot\left[\boldsymbol{s}^{\dagger}e^{-i\Delta\tau} + \boldsymbol{c}^{*}e^{-i(\Delta+\Delta_{\mathrm{hf}})\tau} + \boldsymbol{a}^{\dagger}e^{-i(\Delta+2\Delta_{\mathrm{hf}})\tau}\right].\end{aligned} \tag{2.19}$$

The final approximation we'll make at this time comes from analysing the size of the terms and considering if any are negligible. More explicitly, in this pertubative limit, the coherences $\hat{\sigma}_{j\neq k,k}$ and the quantum fields $\boldsymbol{s}$ and $\boldsymbol{a}$ in Equation 2.16 are small. This means that we may neglect second order terms of the form $\boldsymbol{s}\tilde{\sigma}_{j\neq k,k}$ and $\boldsymbol{a}\tilde{\sigma}_{j\neq k,k}$. This gives:

$$\begin{aligned}
\partial_\tau \tilde{\sigma}_{12} &= -i(1-\alpha)\boldsymbol{d}_{12}^* \cdot \left[\boldsymbol{s}e^{i\Delta\tau} + \boldsymbol{c}e^{i(\Delta+\Delta_{\mathrm{hf}})\tau} + \boldsymbol{a}e^{i(\Delta+2\Delta_{\mathrm{hf}})\tau}\right] - i\tilde{\sigma}_{13}\boldsymbol{d}_{23}\cdot\boldsymbol{c}e^{i\Delta\tau} \\
\partial_\tau \tilde{\sigma}_{13} &= -i\tilde{\sigma}_{12}\boldsymbol{d}_{23}^*\cdot\boldsymbol{c}^* e^{-i\Delta\tau} + i\tilde{\sigma}_{23}\boldsymbol{d}_{12}^*\cdot\boldsymbol{c}e^{i(\Delta+\Delta_{\mathrm{hf}})\tau} \\
\partial_\tau \tilde{\sigma}_{23} &= i\alpha\boldsymbol{d}_{23}^*\cdot\left[\boldsymbol{s}^\dagger e^{-i(\Delta-\Delta_{\mathrm{hf}})\tau} + \boldsymbol{c}^* e^{-i\Delta\tau} + \boldsymbol{a}^\dagger e^{-i(\Delta+\Delta_{\mathrm{hf}})\tau}\right] + i\tilde{\sigma}_{13}\boldsymbol{d}_{12}\cdot\boldsymbol{c}^* e^{-i(\Delta+\Delta_{\mathrm{hf}})\tau}
\end{aligned} \tag{2.20}$$

From these equations you can begin to see the memory process at work; the signal $\boldsymbol{s}$ in the first equation excites coherence $\tilde{\sigma}_{12}$ which in turn couples to the ground states' coherence $\tilde{\sigma}_{13}$. The last equation is exclusively related to the noise process caused by the anti-Stokes scattering.

2.2.5 Maxwell's equations

From Maxwell's equations we can derive the wave equation for the propagation of the signal field[8] $\boldsymbol{E}_s$ through the atomic ensemble which acts as a dielectric medium in the presence of the field:

$$\left(\nabla^2 - \frac{1}{c^2}\partial_t^2\right)\boldsymbol{E}_s = \mu_0\partial_t^2\boldsymbol{P}_s \tag{2.21}$$

where $\boldsymbol{P}_s$ is the positive frequency component of the dipole moment per unit volume, or atomic polarisation, which acts as a source for the signal field and oscillates at the signal

[8]The same argument will apply to the anti-Stokes field $\boldsymbol{E}_a$

frequency ω_s. $\boldsymbol{P}_s$ can be re-written in terms of the slowly varying polarisation, $\tilde{\boldsymbol{P}}_s$ and the fast oscillating carrier wave: $\boldsymbol{P}_s = \tilde{\boldsymbol{P}}_s e^{i\omega_s \tau}$. Inserting the expression for the signal field from Equation 2.16 into the wave equation and applying the SVE and paraxial approximations again gives:

$$\left[\nabla_\perp^2 + \partial_z^2 + \frac{1}{c^2}\partial_t^2\right]\left[i\boldsymbol{v}_s g_s \hat{S} e^{i\omega_s(t-z/c)}\right] = \mu_0 \partial_t^2 \tilde{\boldsymbol{P}}_s e^{i\omega_s \tau}. \tag{2.22}$$

where, for the sake of completeness, we have included the transverse Laplacian[9]: $\nabla_\perp^2 = \partial_x^2 + \partial_y^2$. Where $k_s = \omega_s/c$ and again making use of the SVE approximation this expression reduces to[119]:

$$\left(\partial_z + \frac{1}{c}\partial_t\right)\hat{S} = -\frac{\mu_0 \omega_s^2}{2 g_s k_s}\boldsymbol{v}_s^* \cdot \tilde{\boldsymbol{P}}_s. \tag{2.23}$$

2.2.6 Memory Equations

To proceed we consider the polarisation density in terms of the atomic dipole operator:

$$\begin{aligned} \tilde{\boldsymbol{P}}_s &= e^{-i\omega_s \tau}\frac{1}{\delta V}\sum_{\beta(\boldsymbol{r})} \boldsymbol{d}^{(\beta)} \\ &= e^{-i\omega_s \tau}\frac{1}{\delta V}\sum_{\beta(\boldsymbol{r})}\left[\boldsymbol{d}_{12}\hat{\sigma}_{12}^{(\beta)} + \boldsymbol{d}_{32}\hat{\sigma}_{32}^{(\beta)}\right] \end{aligned} \tag{2.24}$$

where β labels all the atoms in a small volume δV at position $\boldsymbol{r}$. We can define collective polarisation operators driven at the resonant frequencies as:

$$\begin{aligned} \hat{P} &= \frac{1}{\sqrt{n}\delta V}\sum_{\beta(\boldsymbol{r})}\hat{\sigma}_{12}e^{-i\omega_s\tau} \qquad \hat{R} = \frac{1}{\sqrt{n}\delta V}\sum_{\beta(\boldsymbol{r})}\hat{\sigma}_{32}e^{-i\omega_a\tau} \qquad \hat{B} = \frac{1}{\sqrt{n}\delta V}\sum_{\beta(\boldsymbol{r})}\tilde{\sigma}_{13} \\ \hat{P} &= \frac{1}{\sqrt{n}\delta V}\sum_{\beta(\boldsymbol{r})}\tilde{\sigma}_{12}e^{-i\Delta\tau} \qquad \hat{R} = \frac{1}{\sqrt{n}\delta V}\sum_{\beta(\boldsymbol{r})}\tilde{\sigma}_{32}e^{-i(\Delta+\Delta_{\mathrm{hf}})\tau} \end{aligned} \tag{2.25}$$

[9] In our 1D propagation model the terms involving the transverse Laplacian will evaluate to zero.

where n is the number density of the atoms and in the second line we have moved to the rotating frame. The polarisation operator $\hat{R}$ acts as a source term for the anti-Stokes field. It can be shown[10] that as $\delta V \to 0$ (the continuum approximation), $\hat{P}$, $\hat{R}$ and $\hat{B}$ satisfy bosonic commutation relations, and therefore we identify them as annihilation operators for the atomic polarisations and spin-wave coherence respectively [119]. The use of creation and annihilation operators in the description of the spin coherence is based on the Holstein-Primakho [126] approximation. If we substitute these operators into Equation 2.24 we get:

$$\tilde{\boldsymbol{P}}_s = \sqrt{n}\left(\boldsymbol{d}_{12}\hat{P} + e^{2i\Delta_{\mathrm{hf}}\tau}\boldsymbol{d}_{32}\hat{R}\right) \tag{2.26}$$

$$\tilde{\boldsymbol{P}}_a = \sqrt{n}\left(\boldsymbol{d}_{23}\hat{R} + e^{-2i\Delta_{\mathrm{hf}}\tau}\boldsymbol{d}_{32}\hat{P}\right) \tag{2.27}$$

by then substituting into Equation 2.23 (and the analogous equation for the anti-Stokes field) and defining $\chi_{s,a}^{(ij)} = \frac{\boldsymbol{d}_{ij}\cdot\boldsymbol{v}_{s,a}}{\hbar}\sqrt{n}g_{s,a}$, we are able to produce:

$$\left(\partial_z + \frac{1}{c}\partial_t\right)\hat{S} = -\left(\chi_s^{*(21)}\hat{P} + \chi_s^{*(23)}e^{2i\Delta_{\mathrm{hf}}\tau}\hat{R}\right) \tag{2.28}$$

$$\left(\partial_z + \frac{1}{c}\partial_t\right)\hat{A} = -\left(\chi_a^{*(23)}\hat{R} + \chi_a^{*(21)}e^{-2i\Delta_{\mathrm{hf}}\tau}\hat{P}\right) \tag{2.29}$$

To find expressions for $\hat{P}$ and $\hat{R}$ we substitute their definitions (Equation 2.25) into the optical Bloch equations (Equation 2.20), yielding:

$$\begin{aligned}\partial_t\hat{P} &= -i\Delta\hat{P} + \frac{1}{\sqrt{n}\delta V}\sum_{\beta(\boldsymbol{r})} e^{-i\Delta\tau}\partial_t\tilde{\sigma}_{12} \\ &= -i\Delta\hat{P} - i(1-\alpha)\frac{\sqrt{n}}{\hbar}\boldsymbol{d}_{12}^*\cdot\left(\boldsymbol{s} + \boldsymbol{c}e^{i\Delta_{\mathrm{hf}}\tau} + \boldsymbol{a}e^{2i\Delta_{\mathrm{hf}}\tau}\right) - i\frac{B}{\hbar}\boldsymbol{d}_{23}\cdot\boldsymbol{c}\end{aligned} \tag{2.30}$$

[10] This is shown explicitly in Section 2.4

$$\begin{aligned}\partial_t \hat{R} &= -i(\Delta+\Delta_{\rm hf})\hat{R} + \frac{1}{\sqrt{n}\delta V}\sum_{\beta(\boldsymbol{r})} e^{-i(\Delta+\Delta_{\rm hf})\tau}(\partial_t\tilde{\sigma}_{23})^\dagger \\ &= -i(\Delta+\Delta_{\rm hf})\hat{R} - i\alpha\frac{\sqrt{n}}{\hbar}\boldsymbol{d}_{23}\cdot\left(\boldsymbol{s}e^{-2i\Delta_{hf}\tau}+\boldsymbol{c}e^{-i\Delta_{hf}\tau}+\boldsymbol{a}\right) - i\frac{\hat{B}^\dagger}{\hbar}\boldsymbol{d}_{12}^*\cdot\boldsymbol{c} \quad (2.31)\end{aligned}$$

$$\begin{aligned}\partial_t \hat{B} &= \frac{1}{\sqrt{n}\delta V}\sum_{\beta(\boldsymbol{r})}\partial_t\tilde{\sigma}_{13} \\ &= -i\frac{P}{\hbar}\boldsymbol{d}_{23}^*\cdot\boldsymbol{c}^* + i\frac{R^\dagger}{\hbar}\boldsymbol{d}_{12}^*\cdot\boldsymbol{c} \quad (2.32)\end{aligned}$$

where we have used the fact that, in the continuum limit ($\delta V \to 0$), the sum over the ensemble gives a factor of $n/\hbar$. To account for decoherence we phenomenologically add decay terms to the expressions for $\hat{P}$ and $\hat{R}$. The excited state population decays at a rate of 2γ and so the atomic coherences decay as γ, and we therefore introduce a term $-\gamma\hat{P}$ to the equation for $\partial_t\hat{P}$, and equivalently for $\partial_t\hat{R}$. We assume that the spin-wave does not decay over the timescale of storage of the memory, and thus do not introduce a decoherence term for $\hat{B}$. This assumption is justified as we typically consider storage times of $\approx 10\%$ of the spin-wave lifetime[11]. We have neglected to add Langevin noise operators, which describe independent fluctuations of $\hat{P}$, $\hat{R}$ and $\hat{B}$ and ensure that their bosonic commutation relations still hold. Neglecting these is justified as these operators are initially in the vacuum state and the expectation values of terms involving the operators are all equal to zero (as they appear normally ordered) [119].

Applying these decay terms where $\Gamma_s = \gamma + i\Delta$ ($\Gamma_a = \gamma + i(\Delta+\Delta_{hf})$) is the complex

[11] This lifetime is ultimately given by Doppler dephasing of the spin-wave which we shall discuss in detail in Chapter 6

decay rate for the signal (anti-Stokes) field, and $\Omega_{ij} = \boldsymbol{d}_{ij} \cdot \boldsymbol{v}_c E_c/\hbar$ is the Rabi frequency of the control field, the equations now become:

$$(\partial_t + \Gamma_s)\hat{P} = (1-\alpha)\left(\chi_s^{(21)}\hat{S} - i\Omega_{21}e^{i\Delta_{hf}\tau} + \chi_a^{(21)}e^{2i\Delta_{hf}\tau}\hat{A}\right) - i\Omega_{23}\hat{B} \quad (2.33)$$

$$(\partial_t + \Gamma_a)\hat{R} = \alpha\left(\chi_s^{(23)}e^{-2i\Delta_{hf}\tau}S - i\Omega_{23}e^{-i\Delta_{hf}\tau} + \chi_a^{(23)}\hat{A}\right) - i\Omega_{21}\hat{B}^\dagger \quad (2.34)$$

We also assume that the only time dependence in Equations 2.33 – 2.34 is explicit in the exponentials as we will be operating in the adiabatic limit $\Delta \gg \Omega$ and allows us to eliminate the excited state. In this limit we can consider ω changes sufficiently slowly such that the excited state is never populated. We can hence solve these equations to find $\hat{P}$ and $\hat{R}$:

$$\hat{P} \approx (1-\alpha)\left(\frac{\chi_s^{(21)}}{\Gamma_s}\hat{S} - i\frac{\Omega_{21}e^{i\Delta_{hf}\tau}}{\Gamma_a} + \frac{\chi_a^{(21)}e^{2i\Delta_{hf}\tau}}{\Gamma_a + i\Delta_{hf}}\hat{A}\right) - i\frac{\Omega_{23}}{\Gamma_s}\hat{B} \quad (2.35)$$

$$\hat{R} \approx \alpha\left(\frac{\chi_s^{(23)}e^{-2i\Delta_{hf}\tau}}{\Gamma_s - i\Delta_{hf}}\hat{S} - i\frac{\Omega_{23}e^{-i\Delta_{hf}\tau}}{\Gamma_s} + \frac{\chi_a^{(23)}}{\Gamma_a}\hat{A}\right) - i\frac{\Omega_{21}}{\Gamma_a}\hat{B}^\dagger. \quad (2.36)$$

Substituting these into Equation 2.32 and keeping only stationary terms (the rotating wave approximation again) gives:

$$\begin{aligned}\partial_t\hat{B} = &-i\Omega_{23}^*\chi_s^{(21)}\left[\frac{(1-\alpha)}{\Gamma_s} + \frac{\alpha}{\Gamma_s^*}\right]\hat{S} + i\Omega_{12}^*\chi_a^{*(23)}\left[\frac{(1-\alpha)}{\Gamma_a} + \frac{\alpha}{\Gamma_a^*}\right]\hat{A} \\ &- \left[\frac{|\Omega_{12}|^2}{\Gamma_a^*} + \frac{|\Omega_{23}|^2}{\Gamma_s}\right]\hat{B}. \end{aligned} \quad (2.37)$$

Substituting the expressions for $\hat{P}$ and $\hat{R}$ from Equations 2.35 and 2.36 into the wave equations for the signal and anti-Stokes fields (Equations 2.28 and 2.29), and *finally* arrive at the equations of motion for the Raman memory:

$$\left(\partial_z + \frac{1}{c}\partial_t\right)\hat{S} = i\sqrt{\frac{d\gamma}{L}}\frac{\Omega_{23}}{\Gamma_s}\hat{B} \; - \frac{d\gamma}{L}\left[\frac{(1-\alpha)}{\Gamma_s} + \frac{\alpha}{\Gamma_s^* + i\Delta_{hf}}\right]\hat{S} \tag{2.38}$$

$$\left(\partial_z + \frac{1}{c}\partial_t\right)\hat{A} = i\sqrt{\frac{d\gamma}{L}}\frac{\Omega_{12}}{\Gamma_a}\hat{B}^\dagger - \frac{d\gamma}{L}\left[\frac{(1-\alpha)}{\Gamma_a + i\Delta_{hf}} + \frac{\alpha}{\Gamma_a^*}\right]\hat{A} \tag{2.39}$$

$$\partial_t\hat{B} = -i\Omega_{23}^*\sqrt{\frac{d\gamma}{L}}\left[\frac{(1-\alpha)}{\Gamma_s} + \frac{\alpha}{\Gamma_s^*}\right]\hat{S} + i\Omega_{12}^*\sqrt{\frac{d\gamma}{L}}\left[\frac{(1-\alpha)}{\Gamma_a} + \frac{\alpha}{\Gamma_a^*}\right]\hat{A}^\dagger - \left[\frac{|\Omega_{12}|^2}{\Gamma_a^*} + \frac{|\Omega_{23}|^2}{\Gamma_s}\right]\hat{B} \tag{2.40}$$

We have defined the resonant optical depth as $d = \frac{|\chi|^2 L}{\gamma}$, where L is the length of the atomic medium. The optical depth d is a measure of the proportion of monochromatic light that will be absorbed through an atomic medium, appearing in Beer's law: $I_{\text{out}} = I_{\text{in}}e^{-2d}$.

The final term in Equation 2.40 accounts for the AC Stark shift which is proportional to $|\Omega|^2/\Gamma$, and the final terms in Equations 2.38 and 2.39 account for absorption and dispersion of the signal and anti-Stokes fields.

2.3 Green's Functions (I)

The linearity of the equations of motion means that the relationship between the fields and spin-wave can be described via a linear map with a set of Green's functions [119]. One could consider the memory process in two steps, with one map relating input signals to stored excitation, and a second map converting stored excitations to output signal, however for most purposes it is sufficient to consider a single set relating retrieved signal to input fields. In this way, storage and retrieval of the memory may be written as:

$$\begin{pmatrix} \hat{S}_{\text{out}}(t) \\ \hat{A}^{\dagger}_{\text{out}}(t) \\ \hat{B}_{\text{out}}(z) \end{pmatrix} = \int \begin{pmatrix} G_{ss}(t,t') & G_{sa^\dagger}(t,t') & G_{sb}(t,z') \\ G_{a^\dagger s}(t,t') & G_{a^\dagger a^\dagger}(t,t') & G_{a^\dagger b}(t,z') \\ G_{bs}(z,t') & G_{ba^\dagger}(z,t') & G_{bb}(z,z') \end{pmatrix} \begin{pmatrix} \hat{S}_{\text{in}}(t') \\ \hat{A}^{\dagger}_{\text{in}}(t') \\ \hat{B}_{\text{in}}(z') \end{pmatrix} \mathrm{d}t'/z' \tag{2.41}$$

where $G_{sa^\dagger ti} \equiv G_{s_k a^\dagger}(t, t_i)$ are Green's Functions, representing the map from input to output mode. For example, the equation for the output signal contains all mechanisms in which a signal can be retrieved: it may come from the map from input signal to output signal (G_{ss}), the map of any initial excitation in the spin-wave to output signal (G_{bs}) or the map from the spontaneous anti-Stokes scattering ($G_{a^\dagger s}$). The fact it is a creation operator in this term is critical, it means this process does not need to be seeded and indeed occurs when unseeded (i.e. seeded with the vacuum).

2.3.1 Input Signal

It is useful at this point to consider the input states of the memory. For the signal we will either be considering vacuum, some integer number of photons or a coherent state. We can write both of those as a linear combination of Fock states with the same temporal mode[12] $\sigma(t_1)$ (where $\int |\sigma(t_1)|^2 \mathrm{d}t_1 = 1$). A Fock state of n photons is given by:

$$\left| n^{(1)}_{\sigma} \right\rangle = \int \frac{\sigma(t_1)(S_1^\dagger)^n}{\sqrt{n!}} \left|0\right\rangle \mathrm{d}t_1 = \frac{1}{\sqrt{n!}} \int \sigma(t_1)(S_1^\dagger)^n \left|0\right\rangle \mathrm{d}_1 \tag{2.42}$$

where the $^{(1)}$ index integrated but useful to keep track of and we use $\sigma(t_1) = \sigma_1$ and $\mathrm{d}t_1 = \mathrm{d}_1$.

[12] Temporal modes will be covered in detail in Chapter 5; for the moment we can just consider this to be the temporal pulse shape.

2.3.2 Output Signal

At this point we care (nearly exclusively) about the number of output photons in the signal mode. This can be written as the expectation value of the output bosonic signal operator: $\langle S^\dagger_{out}(t) S_{out}(t)\rangle$. To simplify notation we define $G_{sati} \equiv G_{sa^\dagger}(t, t_i)$ and $S_i \equiv S_{\rm in}(t_i)$, and take out the explicit z- or t-dependence in the integrals by letting $\mathrm{d}_1 \equiv \mathrm{d}t_1$ or $\mathrm{d}z_1$ as appropriate. This simplifies the first line above to:

$$S_{\rm out}(t) = \int \mathrm{d}_1 \left(G_{sst1} S_1 + G_{sa^\dagger t1} A_1^\dagger + G_{sbt1} B_1 \right). \tag{2.43}$$

When considering the product, the only meaningful (non-zero) terms will be when we have a creation/annihilation pair. Using the definition of S_{out} above we have:

$$\begin{aligned} S_t^\dagger S_t &= \int (G^*_{sst1} S_1^\dagger + G^*_{sa^\dagger t1} A_1 + G^*_{sbt1} B_1^\dagger)\mathrm{d}_1 \times \int (G_{sst2} S_2 + G_{sa^\dagger t2} A_2^\dagger + G_{sbt2} B_2)\mathrm{d}_2 \\ &= \int (G^*_{sst1} G_{sst2} S_1^\dagger S_2 + G^*_{sa^\dagger t1} G_{sa^\dagger t2} A_1 A_2^\dagger + G^*_{sbt1} G_{sbt2} B_1^\dagger B_2)\mathrm{d}_{12} \end{aligned} \tag{2.44}$$

The complete input state will be something akin to $|\Psi_{in}\rangle = \left|\psi^{(1)}_{s,\sigma}\right\rangle |0_a\rangle \left|\psi^{(2)}_{b,\beta}\right\rangle$ where $\beta(z_i)$ has the same role as $\sigma(t_1)$ for the spin-wave. For brevity we define $|\Psi_{in}\rangle = \left|s^{(1)}_{in}\right\rangle |0_a\rangle \left|b^{(2)}_{in}\right\rangle$. The expected number of photons retrieved in the signal mode is then:

$$N_{out}(t) = \langle \Psi_{in}| S_t^\dagger S_t |\Psi_{in}\rangle = \langle S_t^\dagger S_t\rangle \tag{2.45}$$

$$\begin{aligned}
\langle S_t^\dagger S_t\rangle &= \int \left\langle s_{in}^{(3)}\right| G_{sst1}^* G_{sst2} S_1^\dagger S_2 \left|s_{in}^{(4)}\right\rangle + \langle 0_a| G_{sa^\dagger t1}^* G_{sa^\dagger t2} A_1 A_2^\dagger |0_a\rangle + \left\langle b_{in}^{(3)}\right| G_{sbt1}^* G_{sbt2} B_1^\dagger B_2 \left|b_{in}^{(4)}\right\rangle \mathrm{d}_{12} \\
&= \int G_{sst1}^* G_{sst2} \left\langle s_{in}^{(3)}\right| S_1^\dagger S_2 \left|s_{in}^{(4)}\right\rangle + G_{sa^\dagger t1}^* G_{sa^\dagger t2} \langle 0_a| A_1 A_2^\dagger |0_a\rangle + G_{sbt1}^* G_{sbt2} \left\langle b_{in}^{(3)}\right| B_1^\dagger B_2 \left|b_{in}^{(4)}\right\rangle \mathrm{d}_{12} \\
&= \langle N_{in}^s\rangle \int G_{sst1}^* G_{sst2} \sigma_1^* \sigma_2 \delta_{12} \mathrm{d}_{12} + \int G_{sa^\dagger t1}^* G_{sa^\dagger t2} \delta_{12} \mathrm{d}_{12} + \langle \eta_p\rangle \int G_{sbt1}^* G_{sbt2} \beta_1^* \beta_2 \delta_{12} \mathrm{d}_{12} \\
&= \langle N_{in}^s\rangle \int |G_{sst1}\sigma_1|^2 \mathrm{d}_1 + \int |G_{sa^\dagger t1}|^2 \mathrm{d}_1 + \langle \eta_p\rangle \int |G_{sbt1}\beta_1|^2 \mathrm{d}_1
\end{aligned} \tag{2.46}$$

The three terms can be described as follows:

1. The first term used the definition in Equation A.14 and describes the output in the signal mode that depends on the input. We label this $N_{mem}(t) = \langle N_{in}^s\rangle \int |G_{sst1}\sigma_1|^2 \mathrm{d}_1$

2. The second term used the bosonic commutation relation (Equation A.7) to calculate photons from spontaneous four-wave mixing: $N_{spont}^{AS}(t) = \int |G_{sa^\dagger t1}|^2 \mathrm{d}_1$

3. Finally the third term describes signal mode photons resulting from spontaneous Raman scattering due to imperfect pumping: $N_{spont}^{P}(t) = \langle \eta_p\rangle \int |G_{sbt1}\beta_1|^2 \mathrm{d}_1$. We have used $\left\langle B^\dagger B\right\rangle = \langle \eta_p\rangle$ which we shall see in the next section we may set equal to α.

Together, these comprise the total number of output photons from the memory interaction

$$\boxed{N_{out} = N_{mem} + N_{spont}^{AS} + N_{spont}^{P}} \tag{2.47}$$

2.4 Spin-Wave I

In the previous sections we have both qualitatively and mathematically described the spin-wave and its Bosonic annihilation/creation operator $\hat{B}$ (Equation 2.25) with regards to the spin-flip operator $\hat{\sigma}_{31} \equiv |3\rangle\langle 1|$. Using this definition allows us to examine the spin-wave's

properties in detail.

The spin-wave we describe is a *hyper-entangled* state over N volume slices/atoms and contains exactly one excitation has the form akin to a Dicke-state (or generalised W-state)[127]; a superposition over N atoms where just one is excited:

$$|\Psi_I\rangle = \sum_i^N \frac{1}{\sqrt{N}} |0_1 \cdots 1_i \cdots 0_N\rangle \tag{2.48}$$

where we have moved to the qubit basis for the two ground states for simplicity. That is, a simple relabelling of the two ground states $|1\rangle$ and $|3\rangle$ to $|0\rangle$ and $|1\rangle$ respectively, and the atomic system is now described to be pumped to the zero state $|0\rangle^{\otimes N}$.

In this basis the creation (and annihilation) operators are therefore:

$$\hat{B}^\dagger = \frac{1}{\sqrt{N}} \sum_i^N |1\rangle \langle 0|_i \bigotimes_{j\neq i}^N \mathbb{1}_j \qquad\qquad \hat{B} = \frac{1}{\sqrt{N}} \sum_i^N |0\rangle \langle 1|_i \bigotimes_{j\neq i}^N \mathbb{1}_j \tag{2.49}$$

(flip on ith spin, identity on the rest).

It is worth checking that these operators obey the Bosonic commutation relation:

$$\begin{aligned} \hat{B}\hat{B}^\dagger &= \frac{1}{N} \sum_i^N (|0\rangle\langle 1|_i \bigotimes_{j\neq i}^N \mathbb{1}_j) \sum_m^N (|1\rangle\langle 0|_i \bigotimes_{n\neq m}^N \mathbb{1}_n) \qquad (2.50) \\ &= \frac{1}{N} \sum_i^N (|0\rangle\langle 0|_i \bigotimes_{j\neq i}^N \mathbb{1}_j) + \sum_i^N \sum_{m\neq i}^N (|0\rangle\langle 1|_i \otimes |1\rangle\langle 0|_m \bigotimes_{n\neq i,m}^N \mathbb{1}_n) \\ \hat{B}^\dagger\hat{B} &= \frac{1}{N} \sum_i^N (|1\rangle\langle 1|_i \bigotimes_{j\neq i}^N \mathbb{1}_j) + \sum_i^N \sum_{m\neq i}^N (|1\rangle\langle 0|_i \otimes |0\rangle\langle 1|_m \bigotimes_{n\neq i,m}^N \mathbb{1}_n) \qquad (2.51) \end{aligned}$$

The double sum (second term) in both products are the same and hence vanishes with the

commutator. Writing $\mathbb{1} = |0\rangle\langle 0| + |1\rangle\langle 1|$ means we can write the commutator:

$$\begin{aligned}\left[\hat{B}, \hat{B}^\dagger\right] &= \frac{1}{N}\sum_i^N (|0\rangle\langle 0| - |1\rangle\langle 1|)_i \bigotimes_{j\neq i}^N \mathbb{1}_j \\ &= \frac{N}{N}\mathbb{1}^{\otimes N} - \frac{2}{N}\sum_i^N (|1\rangle\langle 1|)_i \bigotimes_{j\neq i}^N \mathbb{1}_j \\ &\approx \mathbb{1}^{\otimes N} \end{aligned} \tag{2.52}$$

Hence when N is very large, this commutation relation holds, and our description for the Bosonic operator is valid.

Expectation Values Ideal States: To consider the spin-wave in more detail it is useful to build upon the definition of our *ideal* spin-wave in Equation 2.48. We can then also consider the density matrix ρ_I of such a system.

$$|\Psi_I\rangle = \frac{1}{\sqrt{N}}\sum_i^N |0_1 \cdots 1_i \cdots 0_N\rangle \quad \rho_I = \frac{1}{N}(\sum_i^N |0_1 \cdots 1_i \cdots 0_N\rangle)(\sum_j^N \langle 0_1 \cdots 1_j \cdots 0_N|) \tag{2.53}$$

We know that the annihilation operator $\hat{B}$ on the ideal spin-wave equals the zero (vacuum) state $|0\cdots 0\rangle$, and therefore $\hat{B}^\dagger\hat{B}$ acting on the ideal spin-wave state must equal the ideal spin-wave state.

$$\hat{B}^\dagger |0_1 \cdots 0_N\rangle = |\Psi_I\rangle \tag{2.54}$$

$$\hat{B} |\Psi_I\rangle = \frac{1}{N}\sum_{i,j}^N (|0\rangle \langle 1|_i) |0_1 \cdots 1_j \cdots 0_N\rangle = |0_1 \cdots 0_N\rangle$$

$$\therefore \quad \hat{B}^\dagger\hat{B} |\Psi_I\rangle = |\Psi_I\rangle \tag{2.55}$$

$$\therefore \quad \langle\Psi_I| \hat{B}^\dagger\hat{B} |\Psi_I\rangle = \mathrm{Tr}\left(\rho_I \hat{B}^\dagger\hat{B}\right) = 1 \tag{2.56}$$

It is also useful to define some *mixed states* of spin-waves, with 1, 2, n excitations (the zero state ρ_0 is included for completeness):

$$\rho_0 = |0_1 \cdots 0_N\rangle \langle 0_1 \cdots 0_N| \tag{2.57}$$

$$\rho_1 = \sum_i^N \frac{1}{N} |0_1 \cdots 1_i \cdots 0_N\rangle \langle 0_1 \cdots 1_i \cdots 0_N| \tag{2.58}$$

$$\rho_2 = \sum_{i_1,i_2}^N \frac{1}{N(N-1)} |0_1 \cdots 1_{i_1} \cdots 1_{i_2} \cdots 0_N\rangle \langle 0_1 \cdots 1_{i_1} \cdots 1_{i_2} \cdots 0_N| \tag{2.59}$$

$$\rho_n = \sum_j^n \sum_{i_j}^N \frac{(N-n)!}{N!} \left|0_1 \cdots 1_{i_1} \cdots 1_{i_j} \cdots 0_N\right\rangle \left\langle 0_1 \cdots 1_{i_1} \cdots 1_{i_j} \cdots 0_N\right| \tag{2.60}$$

Thus ρ_n represents a mixed state with n excitations. There are ${}^N P_n$ permutations that the n excitations can occupy in the N atoms, represented by the sums in ρ_n.

We note that $\mathrm{Tr}\left(\rho_0 \hat{B}^\dagger \hat{B}\right) = 0$ and $\mathrm{Tr}\left(\rho_n \hat{B}^\dagger \hat{B}\right) = \frac{n}{N}$

With a pumping efficiency of $(1-\alpha)$ we can assume the initial state ρ_{in} to be a thermal (Bose-Einstein) distribution of ρ_i's with average excitation number αN:

$$\rho_{\mathrm{in}} = \sum_i^N \frac{1}{(\alpha N + 1)} \left(\frac{\alpha N}{\alpha N + 1}\right)^i \times \rho_i \tag{2.61}$$

This gives:

$$\begin{aligned}
\mathrm{Tr}\left(\rho_{\mathrm{in}} \hat{B}^\dagger \hat{B}\right) &= \sum_i^N \frac{1}{(\alpha N + 1)} \left(\frac{\alpha N}{\alpha N + 1}\right)^i \times \frac{i}{N} \\
&= \frac{1}{N} \times \frac{\alpha N \left(1 + \alpha N - (1 + \alpha N + N)\left(\frac{\alpha N}{\alpha N + 1}\right)^N\right)}{(1 + \alpha N)} \\
&\simeq \frac{\alpha N (1 + \alpha N)}{N(1 + \alpha N)} \quad \left[\text{to a very good approximation } \left(\frac{\alpha N}{\alpha N + 1}\right)^N = 0\right] \\
&= \alpha
\end{aligned} \tag{2.62}$$

The implication of the above results are as follows: with the pumping efficiency given by $(1-\alpha)$ then the expectation of $\langle \hat{B}^\dagger \hat{B} \rangle = \alpha$ yields the number of spin-wave excitations that could be read-out into the signal mode, producing spurious photons created in the signal mode. The number of these excitations that get mapped into the signal mode is defined by G_{sb} from Equation 2.41, and thus produces the term N^P_{spont} in Equation 2.47.

2.4.1 Multiple pure state excitations

It will become useful to consider multiple instances of the spin-wave creation operator. To do this we now introduce the bracketed subscript to introduce normalised pure state spin-wave with n excitations $\left|\Psi_I^{(n)}\right\rangle = \left(1/\sqrt{^N P_n}\right) \sum_j^n \sum_{i_j}^N \left|0_1 \cdots 1_{i_1} \cdots 1_{i_j} \cdots 0_N\right\rangle$ where

$$\begin{aligned}
\hat{B}^\dagger \hat{B}^\dagger \left|0_1 \cdots 0_N\right\rangle &= \hat{B}^\dagger \left|\Psi_I\right\rangle \\
&= \hat{B}^\dagger \left|\Psi_I^{(1)}\right\rangle \\
&= \frac{1}{\sqrt{N(N-1)}} \sum_{i,j}^N \left|0_1 \cdots 1_i \cdots 1_j \cdots 0_N\right\rangle \\
&= \left|\Psi_I^{(2)}\right\rangle
\end{aligned} \tag{2.63}$$

Furthermore $\hat{B}\left|\Psi_I^{(2)}\right\rangle = \sqrt{2}\left|\Psi_I^{(1)}\right\rangle$ *(without normalisation)* as $\hat{B}$ can annihilate either the i-th or the j-th spin, (and so $\hat{B}\left|\Psi_I^{(n)}\right\rangle = \sqrt{n}\left|\Psi_I^{(n-1)}\right\rangle$). Likewise $\hat{B}^\dagger\left|\Psi_I^{(n)}\right\rangle = \sqrt{n+1}\left|\Psi_I^{(n+1)}\right\rangle$ From here it follows $\mathrm{Tr}\left(\rho_n \hat{B}^\dagger \hat{B}^\dagger \hat{B}\hat{B}\right) = \frac{n(n-1)}{N^2}$, and so gives:

$$\begin{aligned}
\mathrm{Tr}\left(\rho_{\mathrm{in}} \hat{B}^\dagger \hat{B}^\dagger \hat{B}\hat{B}\right) &= \sum_i^N \frac{1}{(\alpha N+1)} \left(\frac{\alpha N}{\alpha N+1}\right)^i \times \frac{i(i-1)}{N^2} \\
&= \frac{1}{N^2} \times \frac{2\alpha^2 N^2(\alpha N+1)}{(1+\alpha N)} \quad \left[\text{after approximating } \left(\frac{\alpha N}{\alpha N+1}\right)^N = 0\right] \\
&= 2\alpha^2
\end{aligned} \tag{2.64}$$

2.5 Simulation

The final theory I shall cover in this section is the simulations I performed in Python [128]. We numerically solve Equations 2.38 – 2.40 using a combination of the Runge-Kutta method [129] and Chebyshev iteration method [130] in the following way:

- A grid in (z, t) space is used with (N_z, N_t) points. N_z must be sufficiently large to sample the absorption length of the all fields through the atomic medium, and N_t must satisfy $N_t > (cT_{\text{sim}}/L)\, N_z^2$ where T_{sim} is the total simulation time, to ensure numerical stability.

- A matrix ρ combining S, A, B is initialised according to the boundary conditions at $t = 0$.

- A function f is created to perform derivatives: $\dot{\rho} = f(t, \rho)$. The Chebyshev method is used to perform the differential $\partial/\partial z$ on S and A.

- The Runge-Kutta method is used to perform the time derivative, by discretising ρ into N_t time steps and defining:

$$\rho_{n+1} = \rho_n + \frac{dt}{6}(k_1 + 2k_2 + 2k_3 + k_4) \qquad k_1 = f(t_n, \rho_n)$$

$$t_{n+1} = t_n + dt \qquad k_2 = f(t_n + \frac{dt}{2}, \rho_n + k_1\frac{dt}{2})$$

$$k_3 = f(t_n + \frac{dt}{2}, \rho_n + k_2\frac{dt}{2})$$

$$k_4 = f(t_n + dt, \rho_n + k_3 dt)$$

- This simulation is then run for increasing timesteps, constantly updating the $z = 0$ boundary condition.

- The final result of this simulation in a $(3 \times N_z \times N_t)$ array in (z, t) space for the three variables S, A, B.

It is easy to picture this matrix in the following way: the S vector for the first N_z value has dimensions: $(1 \times 1 \times N_t)$ and describes the input signal mode to the memory as time progresses. Likewise the signal output of the memory has the same dimensions, but the vector is taken for the final N_z value. This will include the transmitted signal and then (at a later time) the retrieved signal from the memory. Figure 2.3 below shows an example simulation at 3 positions within the memory: Firstly the input at $L = 0$ (blue), then at $L/2$ (orange), and finally the output $z = L$ (green).

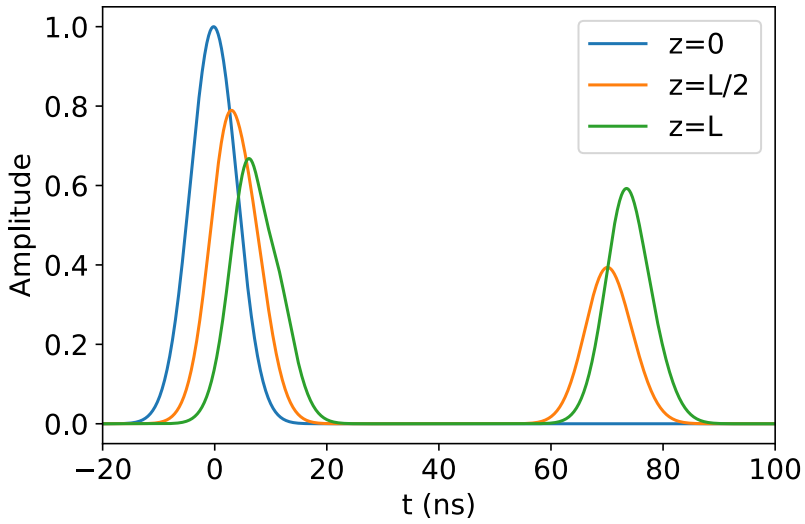

Figure 2.3: Example simulation of storage and retrieval occurring within the memory. An input pulse of 10 ns FWHM is incident on the memory (blue) and as it is stored in the memory, the signal amplitude diminishes until it exits (green). Retrieval begins at 65 ns, and that retrieved signal can be seen propagating through the memory (orange→green) until it too exits the memory.

We define the memory efficiency as the ratio of the energy of the retrieved signal to the input state:

$$\eta_{\text{mem}} = \frac{N_{\text{out}}}{N_{\text{in}}} = \frac{\int_{-\infty}^{+\infty} \mathrm{d}t \left\langle S_{\text{out}}^{\dagger}(t) S_{\text{out}}(t) \right\rangle}{\int_{-\infty}^{+\infty} \mathrm{d}t \left\langle S_{\text{in}}^{\dagger}(t) S_{\text{in}}(t) \right\rangle}. \tag{2.65}$$

Practically, in the simulation, this is the integral ($|amplitude|^2$) of the second green pulse (output) over the blue (input). By setting $\Omega_{12} = 0$ and fixing $\hat{A} = 0$ we are able to simulate the memory interaction without the four-wave mixing process. By comparing the efficiency of the memory with, and without the FWM process, will give us one metric as an indicator for how effective any noise suppression method is.

2.5.1 Green's Functions (II)

We have described how to simulate the memory interaction for a given input signal and control field, however we still need to construct the Green's functions described in Equation 2.41. To do this we consider the same control field in all cases and completely span the space of input signals. To do this we use Hermite-Gauss modes[13] for the temporal profile ($\sigma(t)$ in Equation 2.42) of our input states. Each constituent part of the Green's function $G_{ss}(t, t_i)$ is a matrix created by the outer-product of the input and output signal vectors when using the Hermite-Gauss modes as an input. The sum of these matrices then forms the final Green's function $G_{ss}(t, t_i)$.

2.5.2 Single Value Decomposition

The single value decomposition (SVD) is a standard tool in linear algebra, lending itself to many applications within various fields of natural sciences. The singular value decomposition of a rectangular matrix $M \in \mathbb{C}^{m\times n}$, where without loss of generality $m \geq n$, is a decomposition obtained by orthogonal transformation which produces a diagonal matrix:

$$M = U\Sigma V^{\dagger} \tag{2.66}$$

[13]These are defined fully in Chapter 5.

where U and V are unitary matrices of sizes $(m \times m)$, and $(n \times n)$ respectively and $\Sigma = \text{diag}(\lambda_1, \ldots, \lambda_n)$, where $\lambda_i \geq 0$ and are called the singular values. By convention these are listed in descending magnitude such that $\Sigma_{11} = \lambda_1$ is the largest value.

Performing the SVD on the Green's Function $G_{ss}(t, t_i)$ yields the optimum input mode given the memory conditions (most importantly the control field Ω_{12}) – in this case optimum refers to maximising efficiency. In Chapter 5 we shall see how it is experimentally possible to carve HG modes, and in principle carve the optimum basis state (comprised of a superposition of HG modes) predicted by the SVD of the Green's function.

The Green's functions also play a pivotal role in the following chapter, since as can be seen from equation 2.46, the Green's function $|G_{sa^\dagger t1}|^2$ directly links to the spontaneous signal produced by anti-Stokes scattering in Equation 2.47.

2.6 Previous Experiments

Suppressing four-wave mixing noise to enable quantum-level operation of the Raman memory has been a key focus of the research group for the past few years, a goal that has until now proved elusive. This section briefly outlines the key developments of the implementations of the Raman memory since its conception in 2007 [119,131].

- (2010) The Raman memory was first demonstrated with a coherent state, demonstrating a storage time of 12.5 ns and a total efficiency of 15%. The coherence of the retrieved pulse was demonstrated by the observation of interference fringes between the retrieved state and a delayed copy of the input state. The maximum fringe visibility of $86 \pm 5\%$ demonstrated that the memory interaction is coherent [93].

- (2011) Single photon level coherent light, $\langle n \rangle = 1.6$, was stored for 4 µs with total efficiency of 15%. An unconditional noise floor of 0.25 photons per pulse was observed and attributed to four-wave mixing[132]. [$\mu_1 \approx 1$]

- (2012) The ability to store polarisation encoded information was demonstrated using a *dual-rail* architecture. Horizontal and vertical polarisations are split into two beam-paths through the memory before being recombined after the memory. In this way any arbitrary polarisation can be stored. This was demonstrated with an upper-bound on the conditional Fidelity of 97%, dropping to 86% for a 1.5 µs storage time, this was despite no improvement in efficiency (30%) storing $\langle n \rangle = 10^4 - 10^5$ [133].

- (2015) Heralded single photons with input $g^{(2)} = 0.016$ were stored in the memory and retrieved with $g^{(2)} = 1.59$, displaying no non-classicality. Four-wave mixing contributing thermal statistics to the retrieved $g^{(2)}$ was identified as the key barrier to retrieving quantum states[92].

- (2016) A cavity was used to suppress four-wave mixing by being anti-resonant with the anti-Stokes field with the noise floor lowered to $(15 \pm 2) \times 10^{-3}$ photons per pulse and a total efficiency of $(9.5 \pm 0.5)\%$ for the storage of weak coherent states with $\langle n \rangle = 0.7$[134] ($\mu_1 \approx 0.17$, reduced from $\mu_1 \approx 0.5$ with the best free-space operation). This demonstrated a successful method to suppress the anti-Stokes scattering and hence reduce the noise.

  However, the intra-cavity loss sustained during the demonstration was too high to achieve single-photon storage. This method of suppression is viable given future engineering advances, but is far from technically simple. I shall detail how this method

acts in a similar way to noise suppression technique that I investigate in Chapter 4.

2.7 Summary of the Raman memory theory

By deriving an expression for the light-matter Hamiltonian, we have found a set of optical Bloch equations which describe the temporal evolution of the atomic populations and coherences in the rotating-wave approximation. Furthermore, we derived the propagation equation of the signal field using the paraxial and slowly-varying-amplitude approximations. Having defined bosonic operators for the atomic polarisation and the collective spin wave coherence, we then arrived at a set of dynamical equations for the memory interaction. These differ from those first derived by the inclusion of the anti-Stokes field, which ultimately adds noise to the retrieved signal.

We described the hyper-entangled spin-wave in detail and examined noise due to imperfect preparation of the atomic ensemble. Finally we have showed that solutions to the memory equations of motion are given by a linear mapping, represented by a Green's function which relates input and output modes via a linear transformation. The shape of the optimal input mode and the associated memory efficiency can then be determined by performing an SVD of the Green's function.

Having established a theoretical framework for the Raman memory, we will next consider a theory to best describe the impact of the added noise using photon statistics. This will lead to the derivation of a tool that can best describe the ramifications of the added noise.

Chapter 3

Photon statistics

"There are three types of lies: Lies, damn lies, and statistics."

Benjamin Disraeli

In Section 1.2 we defined a single photon. If we now consider a coherent beam of light, one might imagine this as a periodic stream of photons. This is not the case – discretising photons in this way leads to statistical fluctuations within the number distribution. The probability to detect n photons within a coherent state, average photon number $\langle n \rangle$ is given by a Poissonian distribution [23]:

$$p(n) = \frac{\langle n \rangle^n}{n!} e^{-\langle n \rangle}. \tag{3.1}$$

For photons emitted from a black body, have super-Poissonian statistics given by:

$$p(n) = \frac{1}{\langle n \rangle + 1} \left(\frac{\langle n \rangle}{\langle n \rangle + 1} \right)^n \tag{3.2}$$

Sub-Poissonian states have a smaller varience and are thus more stable: now we can now imagine our equidistant photon stream. This gives a pure photon-number state, described in the Fock basis [23].

3.1 Second-order autocorrelation function

As can be guessed from the above, the nature of any light source can be uniquely characterized by its coherence properties. Experimentally the coherence properties of light are measured by correlation functions of different order as described originally by Glauber [135]. The photon number statistics of classical and non-classical states of light can be distinguished by measuring the second-order intensity autocorrelation function, $g^{(2)}$, using a Hanbury Brown-Twiss set up as shown in Figure 3.1.

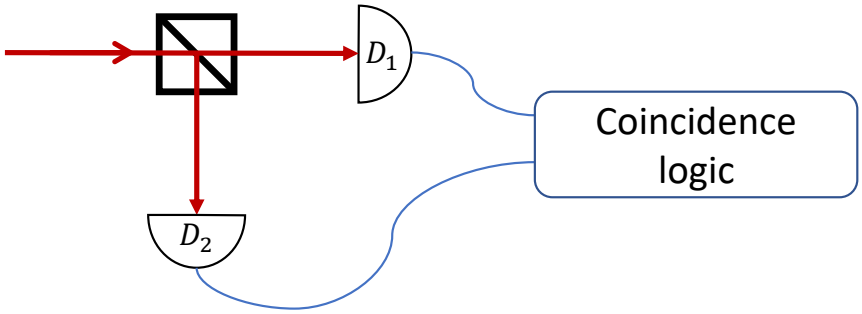

Figure 3.1: Figure showing a Hanbury Brown-Twiss set up where an input is split on a Beam-Splitter before two photodetectors. A coincidence measurement is made between the signals from the two detectors. This can be used to yield a $g^{(2)}$ measurement as a function of delay between the two detections.

We can define the normalised $g^{(2)}$ in terms of normally ordered products of photon creation and annihilation operators so that - at zero time delay -

$$g^{(2)}(\tau = 0) = \frac{\langle \hat{a}^\dagger \hat{a}^\dagger \hat{a} \hat{a} \rangle}{\langle \hat{a}^\dagger \hat{a} \rangle^2} \tag{3.3}$$

We may further relate this to the variance $V_n = \langle \Delta n \rangle^2 = \langle n^2 \rangle - \langle n \rangle^2$ of the photon number distribution where $\langle n \rangle$ is the mean photon number given by $\langle \hat{n} \rangle = \langle \hat{a}^\dagger \hat{a} \rangle$

$$g^{(2)}(0) = \frac{\langle \hat{a}^\dagger(\hat{a}\hat{a}^\dagger - 1)\hat{a}\rangle}{\langle \hat{a}^\dagger\hat{a}\rangle^2} = \frac{\langle \hat{n}^2\rangle - \langle \hat{n}\rangle}{\langle \hat{n}\rangle^2} = 1 + \frac{\langle \Delta n\rangle^2 - \langle \hat{n}\rangle}{\langle \hat{n}\rangle^2}. \tag{3.4}$$

Classical light sources are bounded with a $g^{(2)}(0) \geq 1$ with a coherent source exhibiting Poissonian photon number statistics with $\langle \hat{n}\rangle = (\Delta n)^2$, resulting in $g^{(2)}(0) = 1$. A single-mode thermal source has a $g^{(2)}(0) = 2$. Any light source with $g^{(2)}(0) < 1$ exhibits sub-Poissonian photon statistics and the light is said to be *antibunched*. This inequality corresponds to sub-Poissonian statistics for which the variance of the photon number distribution is less than its mean, thus violating the Cauchy-Schwarz inequality for classical distributions. A single photon Fock state $|n = 1\rangle$ has $\langle \hat{n}\rangle = 1$ and $(\Delta n)^2 = 0$, resulting in $g^{(2)}(0) = 0$ for this state.[1]

We may also write the $g^{(2)}$ in terms of the density matrix of the input state:

$$g^{(2)}(0) = \frac{\langle \hat{n}(\hat{n} - 1)\rangle}{\langle \hat{n}\rangle^2} = \frac{\mathrm{Tr}\{\hat{\rho}\hat{n}(\hat{n} - 1)\}}{(\mathrm{Tr}\{\hat{\rho}\hat{n}\})^2} \tag{3.5}$$

Only the diagonal terms of the density matrix (when written in the photon number-state basis) contribute to $g^{(2)}(0)$. Thus we can rewrite this in terms of the per-pulse photon probabilities as

$$\begin{aligned} g^{(2)}(0) &= \frac{\sum_{n=0}^{\infty} n(n-1)P(n)}{\left(\sum_{n=0}^{\infty} nP(n)\right)^2} \\ &= \frac{2P(2) + 6P(3) + 12P(4) + \dots}{(P(1) + 2P(2) + 3P(3) + \dots)^2} \\ &= \frac{2P(2) + 6P(3) + 12P(4) + \dots}{\mu^2} \end{aligned} \tag{3.6}$$

[1] These results are described in full in Appendix A.1 using the formalisms used in the earlier derivations.

where μ is the mean photon number per pulse. This is useful if we wish to simulate mixtures of different photon number distributions.

Experimentally the $g^{(2)}(0)$ of a single mode of light is measured using a Hanbury-Brown-Twiss (HBT) interferometer shown in Figure 3.1. The setup consists of a 50/50 beam splitter (BS) and an APD each at the two output ports of the BS, D1 and D2. The $g^{(2)}(0)$ is obtained from the probability of coincidence between the clicks from both detectors (P1,2) and the probability of independent clicks (P1 and P2) on each detector.

$$g^{(2)}(0) = \frac{P_{1,2}}{P_1 P_2} = \frac{G^{(2)}_{1,2}}{s_1 s_2 \Delta t_c T} \tag{3.7}$$

where $G^{(2)}_{1,2}$ is the total number of conincidences in measurement time T, s_1 and s_2 are the count rates on D_1 and D_2 and Δt_c is the width of the coincidence window used for $G^{(2)}_{1,2}$.

3.2 $g^{(2)}$ of the Raman memory

In Section 2.3.2 we showed how the signal mode output from the memory could be calculated from the expectation values of $\langle S^{\dagger}_{out}(t) S_{out}(t)\rangle$. In this section we go one step further and examine the $g^{(2)}_{\text{out}}$ of the memory. This is defined as:

$$g^{(2)}_{\text{out}} = \frac{\iint \mathrm{d}t\, \mathrm{d}t' \left\langle S^{\dagger}_{\text{out}}(t') S^{\dagger}_{\text{out}}(t) S_{\text{out}}(t) S_{\text{out}}(t') \right\rangle}{\left(\int \mathrm{d}t \left\langle S^{\dagger}_{\text{out}}(t) S_{\text{out}}(t) \right\rangle \right)^2}. \tag{3.8}$$

It is clear from the definition of S_{out} below,

$$S_{\text{out}}(t) = \int \mathrm{d}_1 \left(G_{sst1} S_1 + G_{sa^{\dagger}t1} A^{\dagger}_1 + G_{sbt1} B_1 \right), \tag{3.9}$$

that the numerator of $g^{(2)}_{\text{out}}$ will be a complicated expression. The numerator's expression is therefore:

$$\begin{aligned} S^\dagger_{t'} S^\dagger_t S_t S_{t'} &= \int \left(G^*_{sst'1} S^\dagger_1 + G^*_{sa^\dagger t'1} A_1 + G^*_{sbt'1} B^\dagger_1 \right) \mathrm{d}_1 \times \int \left(G^*_{sst2} S^\dagger_2 + G^*_{sa^\dagger t2} A_2 + G^*_{sbt2} B^\dagger_2 \right) \mathrm{d}_2 \\ &\times \int \left(G_{sst3} S_3 + G_{sa^\dagger t3} A^\dagger_3 + G_{sbt3} B_3 \right) \mathrm{d}_3 \times \int \left(G_{sst'4} S_4 + G_{sa^\dagger t'4} A^\dagger_4 + G_{sbt'4} B_4 \right) \mathrm{d}_4, \end{aligned} \tag{3.10}$$

which will then be integrated over t, t' and the expectation value with $|\Psi_{in}\rangle$ taken. As before, in the product of $S^\dagger_t S_t$ in Equation 2.44, the non-zero product terms must have a pair (or two) of annihilation-creation operators. These non-zero terms can be split into two categories; three terms consisting of 4 similar operators, and the cross-terms comprising of 2 pairs of like operators.

3.2.1 4 similar operators (S, A and B):

Before considering the terms explicitly, we note what we can learn using the $g^{(2)}$ of the input. From the definition, the $g^{(2)}_{in}$ is defined be:

$$g^{(2)}_{\text{in}} = \frac{\iint \mathrm{d}t\, \mathrm{d}t'\ \langle \psi_{\text{in}}|\, S^\dagger_{t'} S^\dagger_t S_t S_{t'}\, |\psi_{\text{in}}\rangle}{\left(\int \mathrm{d}t\ \langle \psi_{\text{in}}|\, S^\dagger_t S_t\, |\psi_{\text{in}}\rangle \right)^2} = \frac{\iint \mathrm{d}t\, \mathrm{d}t'\ \langle \psi_{\text{in}}|\, S^\dagger_{t'} S^\dagger_t S_t S_{t'}\, |\psi_{\text{in}}\rangle}{N^2_{\text{in}}}, \tag{3.11}$$

we can therefore write:

$$\iint \mathrm{d}t\, \mathrm{d}t'\ \langle \psi_{\text{in}}|\, S^\dagger_{t'} S^\dagger_t S_t S_{t'}\, |\psi_{\text{in}}\rangle = N^2_{\text{in}} g^{(2)}_{\text{in}}. \tag{3.12}$$

The equation above can also be applied to the $g^{(2)}_{B,in}$, where this corresponds to the popula-

tion statistics of any initial spin-wave. We can now consider the three terms of the 4 like operators:

1. Using the expectation value in Equation 3.12

$$\begin{aligned}
&\int G^*_{sst'1}G^*_{sst2}G_{sst3}G_{sst'4}\left\langle s^{(5)}_{in}\right| S^\dagger_1 S^\dagger_2 S_3 S_4 \left|s^{(6)}_{in}\right\rangle \mathrm{d}_{1234} \\
&= N^2_{in} g^{(2)}_{in} \int G^*_{sst'1}G^*_{sst2}G_{sst3}G_{sst'4}\sigma^*_2\sigma_3\delta_{12}\delta_{34}\delta_{23}\mathrm{d}_{1234} \\
&= N^2_{in} g^{(2)}_{in} \int |G_{sst1}G_{sst'1}\sigma_1|^2 \mathrm{d}_1 \\
&= N^2_{in} g^{(2)}_{in} \mathbb{G}_{ss}
\end{aligned} \tag{3.13}$$

2. Using the bosonic commutation relation in equation A.7

$$\begin{aligned}
&\int G^*_{sa^\dagger t'1}G^*_{sa^\dagger t2}G_{sa^\dagger t3}G_{sa^\dagger t'4}\left\langle 0_a\right| A_1 A_2 A^\dagger_3 A^\dagger_4 \left|0_a\right\rangle \mathrm{d}_{1234} \\
&= \int G^*_{sa^\dagger t'1}G^*_{sa^\dagger t2}G_{sa^\dagger t3}G_{sa^\dagger t'4}(\delta_{13}\delta_{24}+\delta_{14}\delta_{23})\mathrm{d}_{1234} \\
&= 2\int |G_{sa^\dagger t1}G_{sa^\dagger t'1}|^2 \mathrm{d}_1 \\
&= 2\mathbb{G}_{sa^\dagger}
\end{aligned} \tag{3.14}$$

3. Using the expectation value in Equation 3.12 again

$$\begin{aligned}
&\int G^*_{sbt'1}G^*_{sbt2}G_{sbt3}G_{sbt'4}\left\langle b^{(5)}_{in}\right| B^\dagger_1 B^\dagger_2 B_3 B_4 \left|b^{(6)}_{in}\right\rangle \mathrm{d}_{1234} \\
&= \langle\eta_p\rangle^2 g^{(2)}_{B,in} \int G^*_{sbt'1}G^*_{sbt2}G_{sbt3}G_{sbt'4}\beta^*\beta_3\delta_{12}\delta_{34}\delta_{23}\mathrm{d}_{1234} \\
&= g^{(2)}_{B,in}\langle\eta_p\rangle^2 \int |G_{sbt1}G_{sbt'1}\beta_1|^2 \mathrm{d}_1 \\
&= g^{(2)}_{B,in}\langle\eta_p\rangle^2 \mathbb{G}_{sb}
\end{aligned} \tag{3.15}$$

where $\mathbb{G}_{ij}$ represents the relevant integral kernel. We can calculate the $g^{(2)}$ of the initial spin-wave using the results in Equations 2.62 and 2.64:

$$g^{(2)}_{B,in} = \frac{\langle b_{in}| B_1^\dagger B_2^\dagger B_3 B_4 |b_{in}\rangle}{(\langle b_{in}| B_1^\dagger B_2 |b_{in}\rangle)^2} = \frac{2\alpha^2}{\alpha^2} = 2 \tag{3.16}$$

One might wonder why the $g^{(2)}_{AS}$ doesn't appear. This is due to the anti-normally ordered terms $\langle AA^\dagger\rangle$ and $\langle AAA^\dagger A^\dagger\rangle$ which results in $g^{(2)}_{AS} = 2$ by construction.

3.2.2 Cross-terms

We now consider the cross terms that consist of 2 creation-annihilation pairs of different operators. For example the term that has an $S^\dagger S$ pair and an $AA^\dagger$ pair[2]: $\langle S_i^\dagger S_j A_k A_l^\dagger\rangle$

$$\begin{aligned}
\langle S_i^\dagger S_j A_k A_l^\dagger\rangle = \int & G^*_{sst'1}G^*_{sa^\dagger t2}G_{sa^\dagger t3}G_{sst'4}\langle S_1^\dagger A_2 A_3^\dagger S_4\rangle + G^*_{sst'1}G^*_{sa^\dagger t2}G_{sst'3}G_{sa^\dagger t4}\langle S_1^\dagger A_2 S_3 A_4^\dagger\rangle \\
& + G^*_{sa^\dagger t1}G^*_{sst'2}G_{sa^\dagger t3}G_{sst'4}\langle A_1 S_2^\dagger A_3^\dagger S_4\rangle + G^*_{sa^\dagger t1}G^*_{sst'2}G_{sst'3}G_{sa^\dagger t4}\langle A_1 S_2^\dagger S_3 A_4^\dagger\rangle \mathrm{d}_{1234} \\
= \langle n\rangle \int & G^*_{sst'1}G^*_{sa^\dagger t2}G_{sa^\dagger t3}G_{sst'4}\delta_{14}\delta_{23}\sigma_1^*\sigma_4 + G^*_{sst'1}G^*_{sa^\dagger t2}G_{sst'3}G_{sa^\dagger t4}\delta_{13}\delta_{24}\sigma_1^*\sigma_3 \\
& + G^*_{sa^\dagger t1}G^*_{sst'2}G_{sa^\dagger t3}G_{sst'4}\delta_{13}\delta_{24}\sigma_2^*\sigma_4 + G^*_{sa^\dagger t1}G^*_{sst'2}G_{sst'3}G_{sa^\dagger t4}\delta_{13}\delta_{24}\sigma_1^*\sigma_3 \mathrm{d}_{1234} \\
= 4\langle n\rangle \int & |G_{sst1}\sigma_1|^2 |G_{sa^\dagger t'2}|^2 \mathrm{d}_{12} \\
= 4N_{mem}\cdot & N^{AS}_{spont}
\end{aligned} \tag{3.17}$$

[2]Note that the signal operators are normally-ordered whilst the anti-Stokes field are not. This is a direct consequence of the derivation of the fields, the consequences of which I'll expand on in the following section.

where we have used the results previously obtained in Section 2.3.2 in Equation 2.44 from the derivation $\langle S^\dagger S \rangle$. By extension, the sum of all the cross terms is then:

$$\langle S_{t'}^\dagger S_t^\dagger S_t S_{t'} \rangle_{XT} = 4(N_{mem} \cdot N_{spont}^{AS} + N_{mem} \cdot N_{spont}^{P} + N_{spont}^{P} \cdot N_{spont}^{AS}) \tag{3.18}$$

We are now in a position to write the numerator of Equation 3.8 as:

$$\iint \mathrm{d}t\, \mathrm{d}t' \ \left\langle S_{t'}^\dagger S_t^\dagger S_t S_{t'} \right\rangle = N_{in}^2 g_{in}^{(2)} \mathbb{G}_{ss} + 2\mathbb{G}_{sa^\dagger} + 2\langle \eta_p \rangle^2 \mathbb{G}_{sb} + 4(N_{mem}N_{AS} + N_{AS}N_P + N_{mem}N_P) \tag{3.19}$$

We recall from Equation 2.47 that $\int \mathrm{d}t \left\langle S_t^\dagger S_t \right\rangle = N_{mem} + N_{AS} + N_P$. This now allows us to rewrite the above equation for $\iint \mathrm{d}t\, \mathrm{d}t' \ \left\langle S_{t'}^\dagger S_t^\dagger S_t S_{t'} \right\rangle$

$$= 2\left(\int \mathrm{d}t \left\langle S_t^\dagger S_t \right\rangle \right)^2 - N_{in}^2(2\eta^2 - g_{in}^{(2)}\mathbb{G}_{ss}) - 2(N_{AS}^2 - \mathbb{G}_{sa^\dagger}) - 2(N_P^2 - \langle \eta_p \rangle^2 \mathbb{G}_{sb}), \tag{3.20}$$

where $\eta = N_{mem}/N_i n$. Therefore the $g_{out}^{(2)}$ can be written:

$$\begin{aligned} g_{\mathrm{out,sig}}^{(2)} &= \frac{\iint \mathrm{d}t\, \mathrm{d}t' \, \langle S_{t'}^\dagger S_t^\dagger S_t S_{t'} \rangle}{\left(\int \mathrm{d}t \, \langle S_t^\dagger S_t \rangle \right)^2} \\ &= 2 - \frac{N_{\mathrm{in}}^2(2\eta^2 - g_{\mathrm{in}}^{(2)}\mathbb{G}_{ss}) + 2((N_{\mathrm{spont}}^{AS})^2 - \mathbb{G}_{sa^\dagger}) + 2((N_{\mathrm{spont}}^{P})^2 - \alpha^2 \mathbb{G}_{sb})}{(\eta N_{\mathrm{in}} + N_{\mathrm{spont}}^{AS} + N_{\mathrm{spont}}^{P})^2} \end{aligned} \tag{3.21}$$

We now assume that, if there is no input signal; the noise due to spontaneous Raman scattering would give thermal output statistics[3] i.e. $g_{\mathrm{out}}^{(2)}(N_{\mathrm{in}} = 0) = 2$. If $N_{\mathrm{spont}}^{P} = 0$ and

[3] This is a validated assumption based on both Equation 3.16 and the thermal statistics exhibited by unheralded photons from a PDC source [23].

the thermal noise is only due to spontaneous anti-Stokes scattering:

$$g^{(2)}_{\text{out,sig}} = 2 - \frac{2((N^{AS}_{\text{spont}})^2 - \mathbb{G}_{sa^\dagger})}{(N^{AS}_{\text{spont}})^2} = 2$$

and so we can approximate $\mathbb{G}_{sa^\dagger} = (N^{AS}_{\text{spont}})^2$. Similarly if $N^{AS}_{\text{spont}} = 0$ and we only have thermal noise due to Raman scattering from the unpumped population:

$$g^{(2)}_{\text{out,sig}} = 2 - \frac{2((N^{P}_{\text{spont}})^2 - \alpha^2\mathbb{G}_{sb})}{(N^{P}_{\text{spont}})^2} = 2$$

and $\mathbb{G}_{sb} = (N^{P}_{\text{spont}})^2/\alpha^2$. With these approximations, Equation 3.21 then simplifies to

$$g^{(2)}_{\text{out,sig}} \quad = \quad 2 - \frac{N^2_{\text{in}}(2\eta^2 - g^{(2)}_{\text{in}}\mathbb{G}_{ss}))}{(\eta N_{\text{in}} + N_{\text{spont}})^2}$$

where $N_{\text{spont}} = N^{AS}_{\text{spont}} + N^{P}_{\text{spont}}$.

3.2.3 Including other sources of noise

There are also sources of technical noise we have yet to consider, resulting from the strong control pulse we use to drive the memory. The most prominent source of technical noise is considered to be fluorescence noise N_F whereby the control off-resonantly excites an atom and it radiatively decays, producing photons with some projection into the signal mode. These contributions would incoherently add to the total $g^{(2)}$. The formula for the $g^{(2)}_{12}$ of two fields $(1, 2)$ incoherently combined is given by[92]:

$$g^{(2)}_{12} = \frac{N_1^2 g_1^{(2)} + 2N_1N_2 + N_2^2 g_2^{(2)}}{(N_1 + N_2)^2}. \tag{3.22}$$

Using this to include these noise processes, we finally reach an expression for total $g^{(2)}$ of the measured retrieved state of the memory:

$$\boxed{g_{tot}^{(2)} = 1 + \frac{(\eta N_{in} + N_{spont})^2 - N_{in}^2(2\eta^2 - g_{in}^{(2)}\mathbb{G}_{ss}) + N_F^2(g_F^{(2)} - 1)}{(\eta N_{in} + N_{spont} + N_F)^2}} \tag{3.23}$$

3.3 Applications

The implications of the derivation above are severe, and point to potential issues when testing the noise level of a quantum memory. As mentioned in Chapter 1, a quantum memory should leave the statistics of the retrieved state unchanged compared to the input. The condition $g_{in}^{(2)} = g_{out}^{(2)}$ therefore seems reasonable. We must however be careful to the point eluded to in Section 2.1.1, *gain*. In the event of a non-zero input $g_{in}^{(2)}$ the Green's function describing signal $\rightarrow$ signal, $\mathbb{G}_{ss}$, becomes important. This term allows for the creation of non-spontaneous extra signal, dependent on the size (average photon number) of the input state.

The ramifications for this are, when testing with coherent states, that the size of the coherent state could mask spontaneous noise. Furthermore, there may be photons in the signal mode due to the FWM gain process[136]. The result: $g_{in}^{(2)} = g_{out}^{(2)}$ and apparently noise free (or low noise) operation. However, when tested with single photons, the output $g^{(2)}$ could be found to vary radically from the input $g^{(2)}$ and thus the memory does not perform as well as first thought when coherent states are used.

There is however a solution to this issue, and furthermore, we shall see how we can use Equation 3.23 as a tool to predict the output statistics of the memory. It should be noted that this method of considering photon statistics may be useful in a number of quantum

applications. Whenever there are single photons polluted by another source (e.g. pumping a PDC source, some leakage from the pump laser may occur), one could examine the photon statistics and deduce the impact and the amount of noise added.

3.4 Summary

In this chapter I have introduced the second-order autocorrelation function and shown how it may be calculated from Bosonic operators. I have used the previously derived Bosonic operators for the memory interaction to calculate the predicted photon-statistics for the memory's output. I then proceeded to describe how an additional noise source (i.e. fluorescence) could be incoherently added to the calculation. This calculation I have suggested may be used as a tool to predict statistics when using non-classical input states. In the following chapter I shall propose an experiment to make use of this tool to quantify the performance of a noise suppression scheme.

Chapter 4

Noise suppression experiment

> "Any sufficiently advanced technology is indistinguishable from magic."
>
> Arthur C Clarke

In Section 2.6 I described how the Raman memory has been re-examined and refined over the past decade since its conception. As the memory has moved closer to single-photon storage, it is clear that the noise associated with four-wave mixing would need to be eradicated in order to meet this goal. The anti-Stokes field involved FWM does not participate in the memory interaction and hence suppressing the anti-Stokes should have no adverse affect on the memory interaction whilst simultaneously preventing the noise associated with FWM.

P.M.L conceived the idea that suppression of the anti-Stokes field could be achieved by engineering the position of the field such that it lay on resonance with a populated transition in the atoms. This project was just in its infancy when I joined the group, led by D.J.S, with the experimental effort spearheaded by S.E.T. My theoretical contribution was that described in Chapters 2 and 3. I derived and simulated the equations of motion for the spin-wave and Stokes/anti-Stokes fields. Experimentally, as well as the day-to-day

operation of the experiment, I conceived the experiment that utilised information possessed by the photon statistics of the output state of the memory. This is the experiment that I shall detail here and was published in [137].

Furthermore, I had a significant role in aligning and designing the beam-path for spectral filtering of the control field from the retrieved signal, which will be detailed in the experimental set-up. Prior to the bulk of work from this chapter, the experiment was moved to a new lab with increased temperature stability, allowing the implementation of experiments that ran constantly for tens of hours. I redesigned the optical table set-up in the new laboratory when it was rebuilt with assistance from S.E.T.

4.1 Methods of suppression

There are a number of strategies to suppress four-wave mixing noise: 1) Via selection-rules 2) Increased relative coupling of the Stokes : anti-Stokes fields 3) Manipulation of the density of states 4) Destroy the four-wave mixing phase-matching condition.

4.1.1 Selection Rules

Walther *et al.*[138] proposed a solution to FWM in alkali vapour by applying a magnetic field to introduce Zeeman splitting and then optically pumping to an extreme Zeeman sub-level. By controlling the polarisation of the signal and control fields (specifically, by giving them σ^+ and σ^- polarisations respectively) one can forbid the control from coupling to the initial state. This is because selection rules dictate that the σ^- control could *only* change the m_F number by $+1$, to a state that doesn't exist! Hence the control cannot generate a spurious spin-wave coherence and the FWM pathway is forbidden.

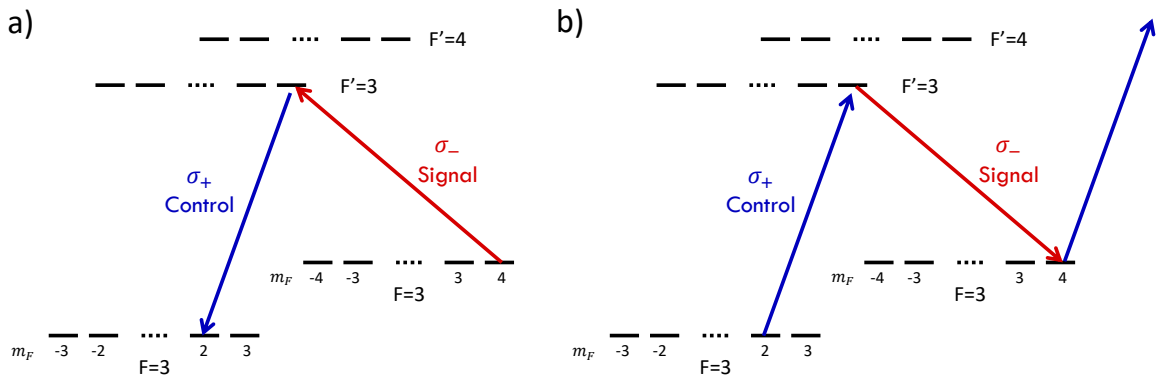

Figure 4.1: A proposed solution to inhibit anti-Stokes scattering. The atoms are initialised to the $|F = 4, m_F = 4\rangle$ state and the memory is operated with σ_- and σ_+ polarisations for the signal and control respectively. The control is unable to couple to the initial state, as selection rules dictate it would need a $m_F = 5$ sublevel which does not exist.

Sadly, whilst selection rules for this Raman coupling have been demonstrated to be able to suppress FWM noise in solid-state systems[139], it has been shown that this method is not applicable to alkali systems[140]. This is because the two transitions in the memory interaction's pathways destructively interfere; this inability to support the memory and FWM suppression simultaneously has been shown and generalised for all alkali isotopes on both the D_1 and D_2 transitions[140].

The destructive interference is a result of the Clebsch-Gordan coefficients having opposite signs. It has very recently been shown within a DLCZ scheme that this can be exploited to a Λ-system *within* hyperfine levels on the D1 line. Here they select the detuning such that the coefficients for the auxiliary FWM field exactly cancel, labelling this as a *magic detuning*[141]. Since they were working with warm vapour, the Doppler width must be less than the detuning, which it is for the D1 line, and they operate at $\sim 924\,\text{MHz}$ blue detuned from $|4', 4'\rangle$.

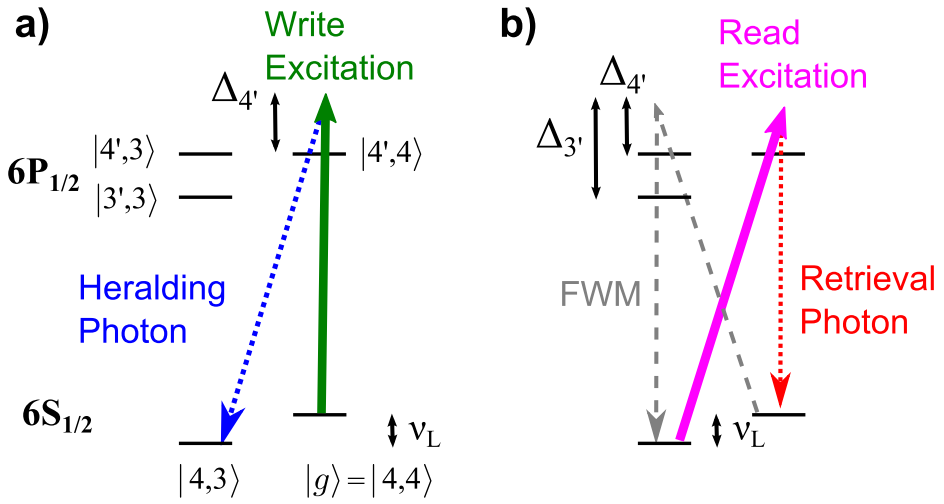

Figure 4.2: The a) write and b) read transition for the *magic detuning* from [141] DLCZ scheme where the FWM is strongly suppressed within the hyperfine λ system by the equal and opposite signs of the Clebsch-Gordon coefficients for the transition $|4,4\rangle \rightarrow |4,3\rangle$ via the $|4',3'\rangle$ and $|3',3'\rangle$ transitions.

4.1.2 Increased ground-state splitting

The difference in detuning for the Stokes and anti-Stokes fields are given by the ground-state splitting of the system; in caesium, this is the famous 9.2 GHz. As we showed in Equation 2.38 the coupling C between signal S and spin-wave B may be written $C \propto \frac{\chi\Omega}{\Gamma}$ where Ω is the Rabi frequency, Γ is the complex decay rate and χ is a constant related to the transition dipole element and defined in Equation 2.28. This may be further extended[118,121] to generalise the Raman scattering coupling as:

$$|C|^2 \approxeq \left(\frac{d\gamma}{\delta_c}\right)\left|\frac{\Omega_{\max}}{\Delta}\right|^2 \tag{4.1}$$

where δ_c is the bandwidth of the control and it is assumed we are in the adiabatic limit such that $|\Gamma| \approx |\Delta|$. The ratio of Stokes to anti-Stokes coupling, therefore, goes like $\Delta + \Delta_{\mathrm{HF}} : \Delta$. Operating the memory closer to the atomic resonance would thereby decrease the relative coupling of the anti-Stokes field. However, this potential route towards reducing the FWM

noise contribution turns out to be unfeasible for our current system due to the onset of linear absorption for $\Delta \leq 5\,\mathrm{GHz}$[1]. This could also add the risk of increased fluorescence.

Alternatively, in solid-state media one could engineer a larger ground state splitting with (for example) strain. This would naturally reduce the prohibiting FWM noise; to this end, demonstrably quantum storage[142], and indeed single-photon storage[143] via the Raman process has been shown in diamond.

4.1.3 Density of states manipulation

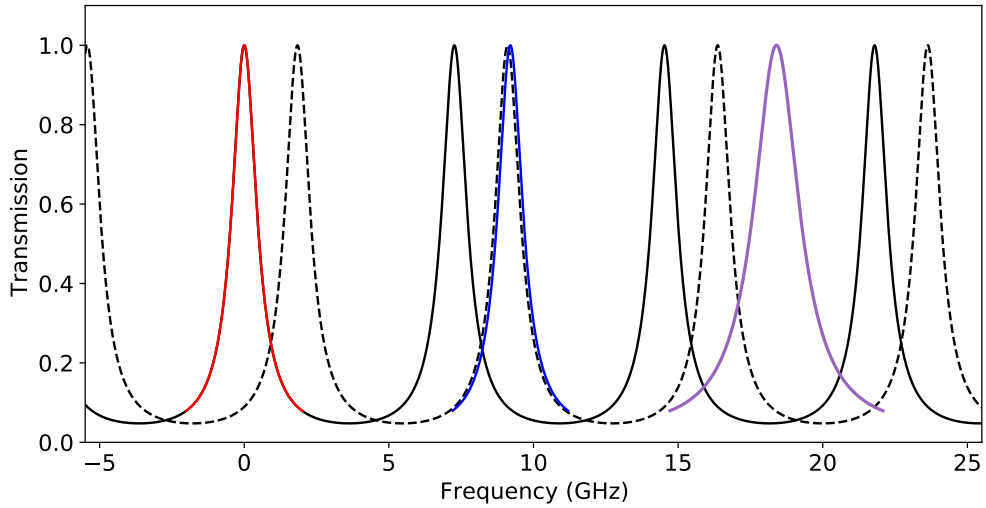

Figure 4.3: Normalised transmission function of doubly resonant cavity with orthogonal polarisations shown in black solid and dashed lines. The orthogonal signal and control are shown in red and blue respectively whilst the anti-Stokes field is in purple. The FSR of the cavity is 7.36 GHz and is shifted by 1.84 GHz for for orthogonal light. Hence both the control and signal are supported but the density of states of the anti-Stokes photons is strongly suppressed.

To prevent unwanted anti-Stokes scattering one could devise a way of manipulating the density of states such that the probability of generating AS photons is strongly suppressed. The orthogonal polarisation of the signal and control means it is possible to design a bi-

[1]The reason this is so large is due to the buffer gas, the purpose of which will appear clear in Section 4.4.1

refringent cavity that is resonant with both the Stokes and control fields (separated by 9.2 GHz) whilst simultaneously being anti-resonant with the anti-Stokes field (which is a further 9.2 GHz detuned from the control).

Whilst this method was successful in reducing the FWM noise, gains made in the signal to noise ratio were significantly hampered by intra-cavity loss [134]. It remains an open engineering challenge to design a cavity with 1) the required triply[2] resonant response *and* 2) low enough loss to successfully retrieve single photons from the memory [144].

4.1.4 Atomic Absorption

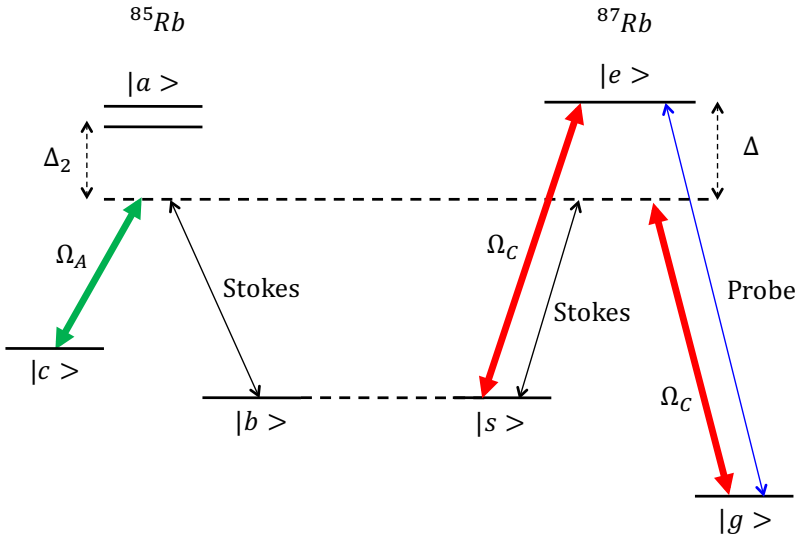

Figure 4.4: An EIT memory is operated in ^{87}Rb and the control coupling to the ground state $|g\rangle$ produces unwanted Stokes photons which would lead to four-wave mixing. By applying an strong auxilary field Ω_A, a 2-photon absorption feature for the unwanted Stokes photons is created in ^{85}Rb. Figure from [145].

The final method considered is based on the idea of using an absorption feature resonant with the anti-Stoke mode to suppress FWM. As mentioned in Section 1.3.3, EIT memories also suffer from FWM noise. This noise suppression approach was first demonstrated in

[2]Resonant with the Stokes and control fields whilst simultaneously anti-resonant with the anti-Stokes field.

rubidium by introducing a different isotope that has an atomic transition resonant with the FWM noise pathway in an EIT memory. Roamnov *et al.*[145] take advantage of the two naturally occurring isotopes in rubidium and implement the memory in ^{87}Rb and use an additional strong control field to create a two-photon absorption feature with the Stokes field in ^{85}Rb shown in Figure 4.4. They demonstrated that this method preserves the coherence in the EIT memory and suppresses four-wave mixing by up to 85%. However, since they engineer the absorption feature via an off-resonant two-photon transition, the suppression is not very strong.

In this chapter, I present a modification of this protocol to suppress FWM in the Raman memory. The memory interaction is modified by operating at a specific (*"magic"*) detuning[3]. The detuning results in the anti-Stokes frequency being resonant with the populated atomic transition of the atoms themselves, as illustrated in Figure 4.5. The anti-Stokes field undergoes strong linear absorption preventing it from being able to create coherence across the ensemble. This, therefore, stops any spurious spinwave from being generated and hence prevents FWM noise.

We posit that the suppression scheme does not have any detrimental effect on memory efficiency or lifetime; the equations of motion are unchanged, there are no additional fields involved and no cavity engineering. We also note that that this *magic detuning* would be applicable to Λ-systems in all atomic species and other systems (such as defects in diamonds[143]). Should the noise suppression scheme prove successful, it would place itself, and by extension the Raman memory protocol as a means for a technically simple, noise-free quantum memory.

[3]This is different from the magic detuning referenced in Section 4.1.1 and [141].

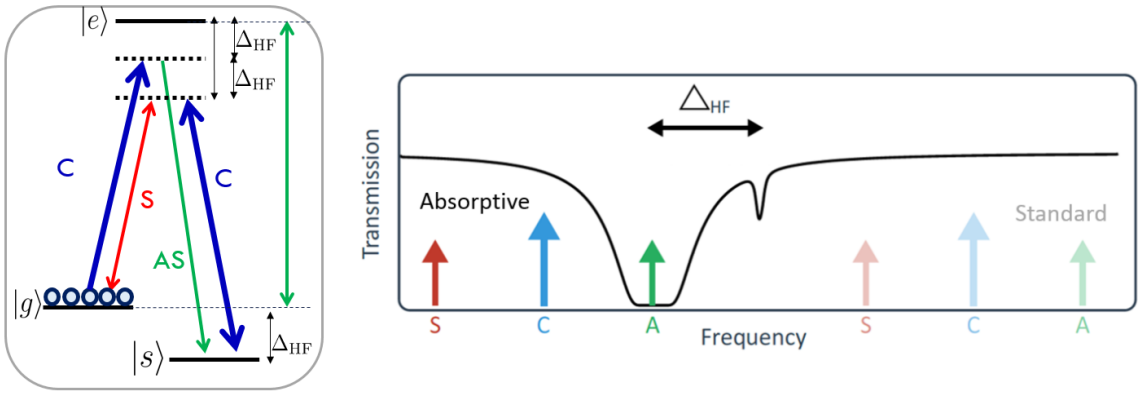

Figure 4.5: Energy level arrangement showing the fields when arranged in the *magic* detuning and in the standard configuration. The field arrangement is showing in comparsion to the transmission spectrum of the pumped Cs vapour

4.2 Theory

In Chapter 2 we derived Equations 2.38 – 2.40 (and repeated boxed below) as the equations of motion for the Raman memory interaction in an atomic Λ-system: a signal field S and strong control pulse with Rabi frequency Ω interact with an ensemble of atoms via a 2-photon Raman transition, thus generating a spin-wave excitation B. The equations additionally describe the field A produced by the unwanted control coupling which ultimately gives rise to spurious contributions to the spin-wave mode B and the four-wave mixing noise process.

$$\begin{aligned}
\left(\partial_z + \frac{1}{c}\partial_t\right)\hat{S} &= i\sqrt{\frac{d\gamma}{L}}\frac{\Omega}{\Gamma_s}\hat{B} \; - \kappa_s\hat{S} \\
\left(\partial_z + \frac{1}{c}\partial_t\right)\hat{A} &= i\sqrt{\frac{d\gamma}{L}}\frac{\Omega_{12}}{\Gamma_a}\hat{B}^\dagger - \kappa_a\hat{A} \qquad (4.2) \\
\partial_t\hat{B} = -i\Omega\sqrt{\frac{d\gamma}{L}}\left[\frac{(1-\alpha)}{\Gamma_s} + \frac{\alpha}{\Gamma_s^*}\right]\hat{S} &+ i\Omega\sqrt{\frac{d\gamma}{L}}\left[\frac{(1-\alpha)}{\Gamma_a} + \frac{\alpha}{\Gamma_a^*}\right]\hat{A}^\dagger - \left[\frac{|\Omega|^2}{\Gamma_a^*} + \frac{|\Omega|^2}{\Gamma_s}\right]\hat{B}
\end{aligned}$$

The atomic absorption and dispersion for the two fields S and A are described by:

$$\kappa_s = \frac{d\gamma}{L}\left[\frac{(1-\alpha)}{\Gamma_s} + \frac{\alpha}{\Gamma_s^* + i\Delta_{hf}}\right] \tag{4.3}$$

$$\kappa_a = \frac{d\gamma}{L}\left[\frac{(1-\alpha)}{\Gamma_a + i\Delta_{hf}} + \frac{\alpha}{\Gamma_a^*}\right] \tag{4.4}$$

where $\Gamma_{s,a} = \gamma + i\Delta_{s,a}$ is the complex detuning of the signal and anti-Stokes fields, γ is the linewidth of the atomic transition (which can be broadened due to collisions with a buffer gas), and α is the proportion of atoms that have not been successfully initialised via optical pumping to the ground state $|g\rangle$ and remain in the storage state $|s\rangle$. The optical depth of the ensemble d, can be related to the on-resonance optical depth, d_0, by $d = d_0\gamma_0/\gamma$, where γ_0 is the natural linewidth.

The *magic* condition is as follows: we choose the signal's detuning to be red-detuned by twice the hyperfine splitting $\Delta_s = -2\Delta_{\mathrm{hf}}$. Since Δ_a is defined as[4] $\Delta_a \equiv \Delta_s + \Delta_{\mathrm{hf}}$ the choice of the magic detuning has a profound effect on κ_a. By looking at Equation 4.4 in the case of perfect initialisation ($\alpha \to 0$) we can see that $\kappa_a \to \frac{d}{L}$. This in turn dictates that the absorption length for the anti-Stokes field is on the order of $\sim L/d$, which for our warm alkali vapour would be sub 100μm.

4.2.1 Spin-wave II

This section continues the description of spin-wave shown in Section 2.4 and describes the spurious spin-wave generated by FWM in both the *standard* configuration and when operating at the *magic detuning*. In this section, for the purposes of gaining a physical intuition for

[4]This definition is first used in Equation 2.34 and it is important to note that whilst Δ_s is equal to the detuning of the signal field from the populated transition, this is *not* the case for Δ_a.

this suppression technique, we shall assume both perfect pumping and that a single photon is read into the memory with unit efficiency.

Standard

In the standard configuration following read-in, the state of the atomic spin-wave ρ_B is comprised of the spin-wave created by the desired memory process ρ_I (with 1 excitation) and that created by the four-wave mixing ρ_A. The spurious spin-wave ρ_A is comprised of a combination of an ideal spin-waves with a thermal distribution and a mean excitation number κ. The relative weighting of these two contributions we denote with β.

$$\rho_A = \sum_i^N \frac{1}{(\kappa+1)} \left(\frac{\kappa}{\kappa+1}\right)^i \left|\Psi_I^{(i)}\right\rangle \left\langle\Psi_I^{(i)}\right| \tag{4.5}$$

$$\rho_B = (1-\beta)\rho_I + \beta\rho_A \tag{4.6}$$

The expectation value and $g^{(2)}$ of this spin-wave are as follows:

$$\mathrm{Tr}\Big(\rho_B B^\dagger B\Big) = \Big\langle B^\dagger B\Big\rangle = (1-\beta) + \beta\kappa \tag{4.7}$$

$$\mathrm{Tr}\Big(\rho_B B^\dagger B^\dagger BB\Big) = \Big\langle B^\dagger B^\dagger BB\Big\rangle = 0 + 2\beta\kappa^2 \tag{4.8}$$

$$g^{(2)}_{B_{\mathrm{storage}}} = \frac{2\beta\kappa^2}{(1-\beta(1-\kappa))^2} \tag{4.9}$$

Absorptive

Now we consider what happens when the atoms absorb the anti-Stokes field with absorption length λ. The length of atomic ensemble (/spinwave) is L; we can discretise the atoms into into $M = \frac{L}{\lambda}$ slices (with length λ), and each slice contains $\frac{N}{M}$ atoms. In this basis we can

group the atoms within each slice and treat it as a unit spin-wave or a *logical* spin-wave: $|1_L\rangle = 1/\sqrt{\frac{N}{M}} \sum_i^{\frac{N}{M}} \left|0_1 \cdots 1_i \cdots 0_{\frac{N}{M}}\right\rangle$

In this basis the ideal spin-wave (defined in Equation 2.48) is rewritten:

$$\left|\Psi_I^{(1)}\right\rangle = \sum_i^N \frac{1}{\sqrt{N}} |0_1 \cdots 1_i \cdots 0_N\rangle = \sum_i^M \frac{1}{\sqrt{M}} |0_L\rangle_0 \cdots |1_L\rangle_i \cdots |0_L\rangle_M \tag{4.10}$$

The absorption of the AS changes the form of the spin-wave it creates to ρ'_A. Each of the M slices is made up local ideal spin-waves with a thermal number distribution; however, since it is not possible to garner coherence across the slices, ρ'_A is a mixed state, summing over the slices. This is of the same form as the n mixed state excitations in Equation 2.60 where the number of atoms N has been replaced with the number of slices M.

$$\rho'_m = \sum_j^m \sum_{i_j}^M \frac{(M-m)!}{M!} |0_L\rangle\langle 0_L|_1 \cdots \otimes \cdots |1_L\rangle\langle 1_L|_{i_1} \cdots \otimes \cdots |1_L\rangle\langle 1_L|_{i_j} \cdots \otimes \cdots |0_L\rangle\langle 0_L|_M \tag{4.11}$$

$$\rho'_A = \sum_i^M \frac{1}{(\kappa+1)} \left(\frac{\kappa}{\kappa+1}\right)^i \times \rho'_i \tag{4.12}$$

$$\rho_B = (1-\beta)\rho_I + \beta\rho'_A \tag{4.13}$$

We can again calculate the expectation value and $g^{(2)}$ of the spin-wave:

$$\left\langle B^\dagger B \right\rangle = (1-\beta) + \frac{\beta\kappa}{M} \tag{4.14}$$

$$\left\langle B^\dagger B^\dagger B B \right\rangle = 0 + \frac{2\beta\kappa^2}{M^2} \tag{4.15}$$

$$g^{(2)}_{B'_{\text{storage}}} = \frac{2\beta\kappa^2}{M^2(1-\beta(1-\frac{\kappa}{M}))^2} \tag{4.16}$$

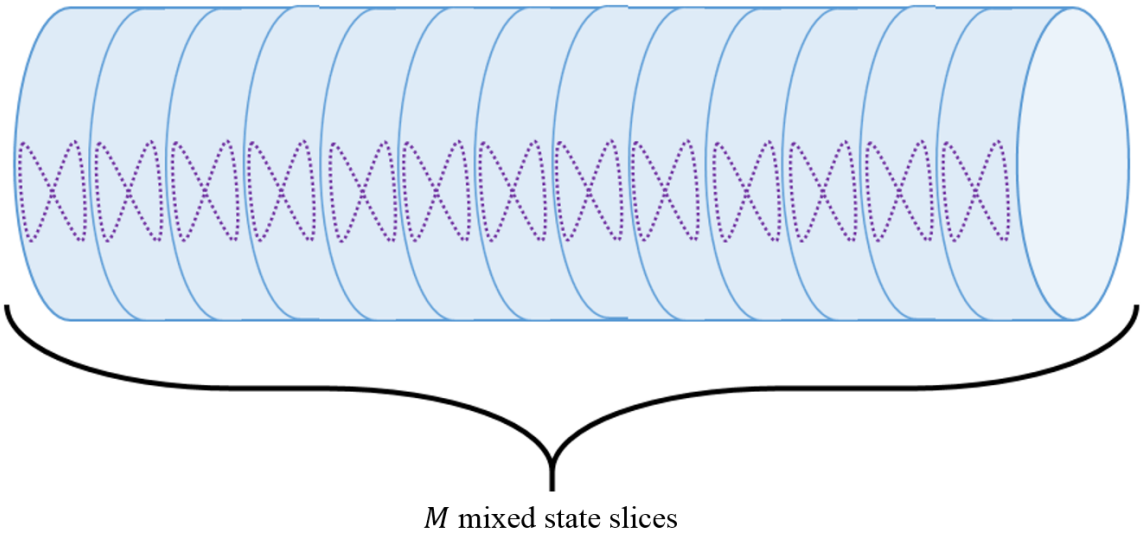

Figure 4.6: M localised spin-waves confined to localised slices.

Comparison

Whilst this is a crude model providing no information about the raw number of excitations that the FWM pollutes the storage spin-wave with, the model does give information about about the comparative merits of the suppression technique. We can also substitute nominal values for β and κ to see how the $g^{(2)}_{out}$ value varies in these cases.

If, for example, we considered that a) we have stored a single photon, with perfect efficiency and b) that there is also a spurious spin-wave generated from AS-scattering with an mean excitation number of 1 ($\kappa = 1$), and that it has equal weighting as the stored single photon ($\beta = 0.5$). In this case we see that in the standard configuration the output $g^{(2)} = 1$ whilst in the suppression case, assuming a modest optical depth of $M = 100$ the output would have $g^{(2)} = 0.0004$. In essence it has the effect of reducing the size of effective

excitations ($\bar{\kappa} = \kappa/M$) by a factor of M.

$$g^{(2)}_{B_{\text{storage}}} = \frac{2\beta\bar{\kappa}^2}{(1-\beta(1-\bar{\kappa}))^2} \tag{4.17}$$

This description describes the case in which the AS field can no longer generate a delocalised excitation over the entire atomic ensemble, as in the case of the desired memory interaction. The spatial confinement of the spurious spin-wave prevents a coherence from being built up across the ensemble, and the resultant overlap with the memory spin-wave mode is greatly diminished. The absorption of an anti-Stokes photon acts as a measurement process which prevents the build up of coherence of the noise excitation and significantly limits the occupation of the noisy spin-wave, in a way that is akin to the quantum Zeno effect [146].

We can alternatively describe this suppression technique by considering the different propagation conditions that the Stokes and anti-Stokes fields experience. The anti-Stokes field undergoes a large amount of dispersion if placed on resonance with a transition, and this prevents the phase-matching condition from being met. By selecting the detuning of the signal field such that there is an absorption feature at the anti-Stokes frequency, we can ensure that the four-wave mixing process is no longer phase-matched and strongly suppressed.

4.2.2 Phase-matching condition

The wave vectors of the Stokes, control and anti-Stokes fields are:

$$\begin{aligned} k_s &= \frac{\omega_s}{c} + \frac{d\gamma}{L}\left[\frac{(1-\alpha)}{\gamma + i\Delta} + \frac{\alpha}{\gamma - i(\Delta - \Delta_{hf})}\right] \\ k_c &= \frac{\omega_c}{c} + \frac{d\gamma}{L}\left[\frac{(1-\alpha)}{\gamma + i(\Delta + \Delta_{hf})} + \frac{\alpha}{\gamma - i\Delta}\right] \\ k_a &= \frac{\omega_a}{c} + \frac{d\gamma}{L}\left[\frac{(1-\alpha)}{\gamma + i(\Delta + 2\Delta_{hf})} + \frac{\alpha}{\gamma - i(\Delta + \Delta_{hf})}\right] \end{aligned} \tag{4.18}$$

where we recognise the latter terms of each as describing the absorption and dispersion from Equations 4.3-4.4. Dispersion between the Stokes and anti-Stokes fields leads to a FWM phase mismatch given by $\delta k = 2k_c - k_s - k_a$. The FWM interaction is subject to the constraint of both energy and momentum conservation. Energy conservation requires $2\omega_c = \omega_a + \omega_s$ whilst momentum conservation imposes the phase-matching condition[147] $2\boldsymbol{k_c} + \boldsymbol{k_a} + \boldsymbol{k_s} = 0$. The explicit expression for the phase mismatch δk is given by:

$$\begin{aligned} \delta k = -2\Delta^2 \frac{d\gamma}{L}\Bigg[&\frac{1-\alpha}{(\gamma + i\Delta)[\gamma + i(\Delta + \Delta_{hf})][\gamma + i(\Delta + 2\Delta_{hf})]} \\ &+ \frac{\alpha}{[\gamma - i(\Delta - \Delta_{hf})](\gamma - i\Delta)[\gamma - i(\Delta + \Delta_{hf})]}\Bigg] \end{aligned} \tag{4.19}$$

where energy conservation is assumed.

In the limit of perfect pumping ($\alpha \to 0$) this mismatch becomes proportional to $1/[\gamma + i(\Delta + 2\Delta_{hf})]$. Hence when $\Delta = -2\Delta_{hf}$, the phase mismatch undergoes rapid oscillation modulo 2π and the FWM process goes in and out of phase.

4.3 Simulations

In Section 2.5 I described the framework for simulations I performed in Python; using a combination of the Runge-Kutta method and Chebyshev iteration method to numerically solve Equations 2.38 – 2.40. As stated earlier, the most rudimentary demonstration to test this noise suppression method is to simply turn the FWM terms in the equations *"on"* and *"off"* – and then compare the two. Practically this amounts to setting Ω_{12} (the unwanted control coupling) to zero and removing the anti-Stokes field. Finally we can additionally consider the *standard* configuration where all the fields are blue-detuned – we consider this such that the coupling at the *magic detuning* $\Delta_S = -18.4\,\text{GHz}$ and the $\Delta_S = +18.4\,\text{GHz}$ (blue-detuned) case are the same.

Figure 4.7 shows two simulations from an initial demonstration where we consider an atomic ensemble heated to 83 °C in a 7 cm cell with no pressure broadening, ($\gamma = \gamma_0 = 5.2$ MHz); yielding an optical depth of $d = 2\times10^4$. This allows us to explore how the system behaves in a parameter regime where the number of steps in z required to capture the anti-Stokes absorption is around $N_z = 20$, which is not prohibitively large (computationally). Figure 4.7a uses the rudimentary definition of noise:

$$\text{Noise} = \frac{|N_{\text{out}} - N_{\text{mem}}|}{N_{\text{out}}} = |\eta - \eta_{\text{ideal}}| \tag{4.20}$$

This quantifies the magnitude of the field that is retrieved from the memory due to four-wave mixing rather than the true memory interaction. This metric was calculated for the Raman memory operating over a range of detunings around the *magic detuning* case where the anti-Stokes field is exactly on resonance with the atoms. The simulation show

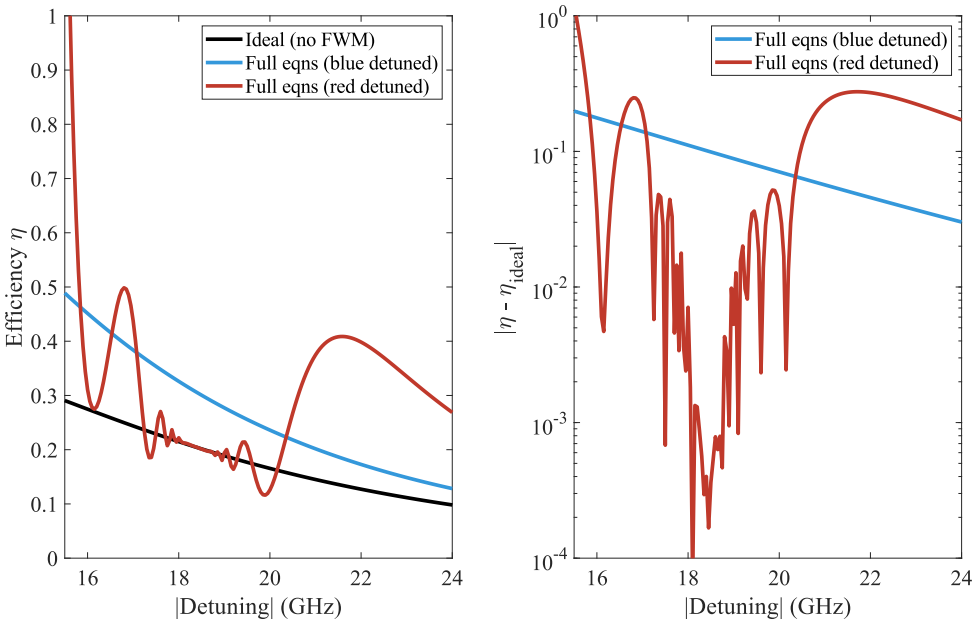

Figure 4.7: Numerical simulations for the output of the Raman memory as a function of detuning. Left: Efficiency of the Raman memory as a function of detuning for three configurations: blue-detuned from resonance in the standard Raman memory configuration (blue); red-detuned from resonance where the built-in noise suppression occurs at the *magic detuning* $\Delta = -2\Delta_{hf} = -18.4\,\text{GHz}$ (red); and the ideal equations of motion with no four-wave mixing (black). Right: The difference in efficiency in the blue and red detuned cases compared to the ideal equations. These simulations were performed with an optical depth $d = 2000$ and a control pulse power of 700pJ.

the possibility of reducing the FWM noise (as measured by this metric) by nearly 4 orders of magnitude. The scale of this suppression qualitatively agrees with the value of optical depth, as implied in the simple spin-wave picture described in the previous section.

We note that when away from the *magic detuning* region the red detuned case has significant excess signal when compared to the ideal equations. We can understand this by noting that the Raman coupling strength in Equation 4.1 has $C \propto 1/\Delta$. When red-detuned, the AS-field's detuning is less than the signal's and as such, has a larger coupling, producing more AS-scattering. This increased AS scattering in turn produces large amounts of extraneous photons in the signal mode (via FWM), leading to apparent efficiencies $\eta > 1$.

The oscillations seen on either side of the *magic detuning* warrant further analysis, and

can be best described when considering the phase-matching condition of the FWM process. We mentioned earlier how δk oscillates modulo 2π in this regime and hence $\sin(L \times \delta k)$ oscillates. This can be thought of as energy transfer between the four fields involved in the mixing and a net transfer of excitation between the matter spin-wave and the optical Stokes/anti-Stokes fields and is shown in Figure 4.8.

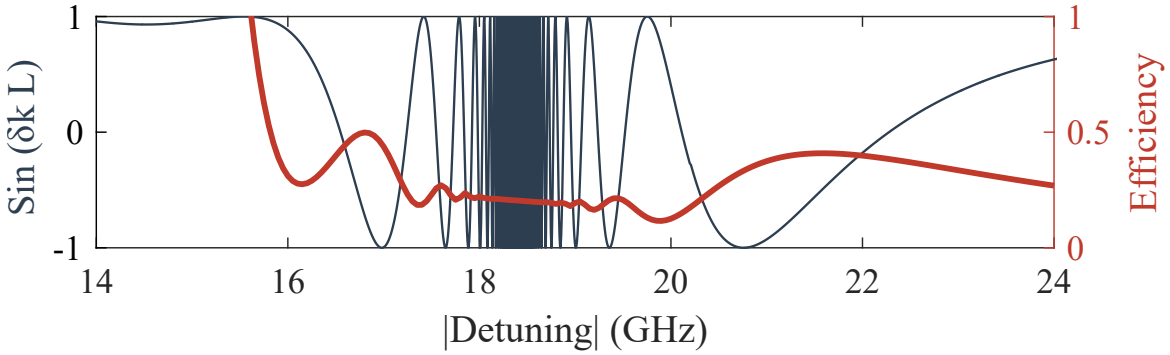

Figure 4.8: Phase matching condition and memory efficiency as a function of detuning.

The simulations of the memory equations 4.2 do not describe all the noise pathways; the simulations therefore only give a minimum for the amount of noise that might be observed. The simulations do however, not only quantify the noise linked to the prohibitive FWM but also show large suppression of this noise source. The dramatic reduction in the noise demonstrates that this absorptive suppression scheme could provide a way for successful storage and retrieval of a quantum state.

4.4 Experiment

We saw in Section 3.2.3 that there is technical noise caused by the strong control pulse that is used to drive the memory and derived an expression for the output statistics given *all*

noise sources in Equation 3.23 and stated again below:

$$g^{(2)}_{tot} = 1 + \frac{(\eta N_{in} + N_{spont})^2 - N_{in}^2(2\eta^2 - g^{(2)}_{in}\mathbb{G}_{ss}) + N_F^2(g^{(2)}_F - 1)}{(\eta N_{in} + N_{spont} + N_F)^2}. \tag{4.21}$$

When testing the memory with coherent state storage it is easy to vary the average photon number in the input state N_{in} – one simply adjusts the attenuation applied to the input signal mode. Since we have the output $g^{(2)}$ as a function of N_{in}, it should be possible to derive values for unknown parameters based on the relationship of $g^{(2)}$ with N_{in}. We can rewrite Equation 4.21 as:

$$g^{(2)}_{tot} = 1 + \frac{AN_{in}^2 + BN_{in} + C}{(\eta N_{in} + D)^2} \tag{4.22}$$

with the following parameters:

Parameter	Meaning	Obtained how
N_{in}	Number of photons in	Measured per run, controlled parameter
$g^{(2)}_{tot}$	Measured $g^{(2)}$	Directly measured
η	Measured efficiency	Directly measured
A	$g^{(2)}_{in}\mathbb{G}_{ss} - \eta^2$	From fit
B	$2\eta N_{spont}$	From fit
C	$N_F^2 + N_{spont}^2$	From fit
D	$N_{spont} + N_F$	Directly measured

Table 4.1: Table showing the parameters in Equation 4.22

Using this information I conceived the following experimental procedure to quantify the reduction in noise due to the suppression method.

(i) We perform storage of coherent states using a constant control field and vary the size of the input state N_{in}. By averaging over many runs we can measure the $g^{(2)}$ of the

output state of the memory. Over these runs we can assume that neither the efficiency η nor the number of photons produced spontaneously (N_{spont} and N_F) changes.

(ii) Fit the data according to Equation 4.22 to obtain values for A, B and C.

(iii) $B/2\eta$ gives an estimate of the number of photons produced by both spontaneous Raman scattering due to imperfect pumping N^{P}_{spont}, and from spontaneous FWM N^{AS}_{spont}. This will give an indication as to the effectiveness of the noise suppression scheme.

(iv) Whilst there is no way to disentangle those two types of spontaneous sources from each other, we'll see in Figure 4.17 we can investigate how spontaneous noise varies as a function of pumping efficiency α. By extrapolating the pumping efficiency to 100% ($\alpha \to 0$) we can assume the remaining noise to come from spontaneous FWM and fluorescence.

(v) Model what would happen in the event of sending in a single photon with a $g^{(2)} = 0$. This will reveal if the suppression scheme has worked enough to maintain non-classical statistics of the output.

4.4.1 Experimental Setup

In this section I shall describe the experimental architecture used to implement the suppression scheme. This includes the vapour-cell, the preparation of optical fields and the filtering. I shall then give the results and describe the future implications that the results yield.

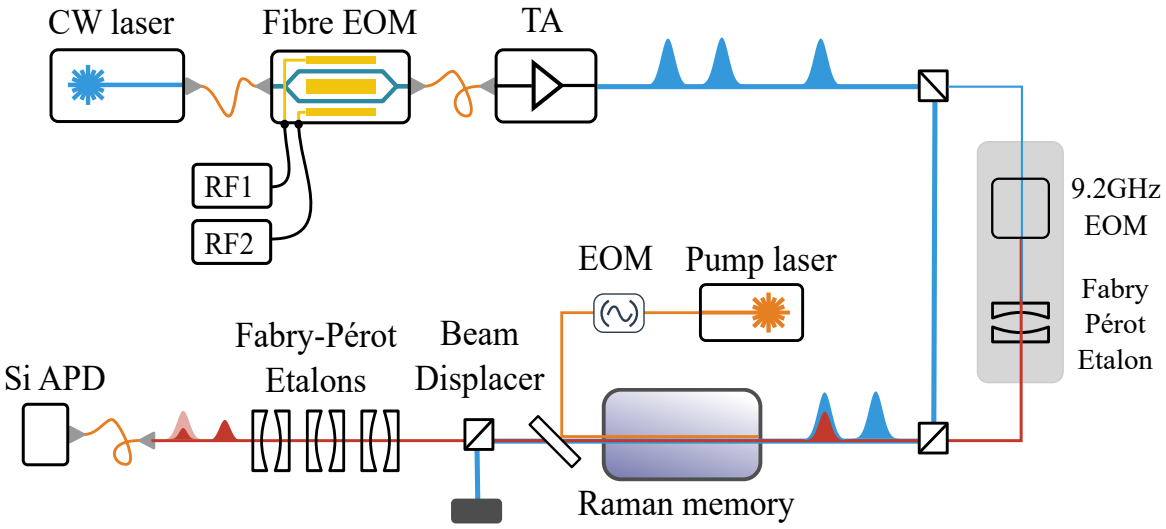

Figure 4.9: Experimental setup of the Raman memory. The signal and control pulses are carved from a CW laser using a fibre integrated electro-optic interferometer (Fibre EOM) driven by RF signals from two arbitrary waveform generators. The pulses are amplified using a tapered amplifier (TA) and split into two arms. The signal pulses pass through an EOM driven at 9.2 GHz to generate a sideband at the signal frequency, and delayed in time to overlap with the strong control pulses. The pulses interact with an ensemble of warm caesium atoms, which is heated to 83°C and initialised in $|g\rangle$ by a counter-propagating optical pumping laser. After the memory the control pulse is filtered from the signal using a beam displacer and Fabry-Pérot etalons, before the signal is detected using a silicon single-photon avalanche photodiode (Si APD).

Storage Medium

In Section 2.2 we derived the equations of motion for a generic atomic Λ-system. For our experiment we implement the Raman interaction in caesium (^{133}Cs) on the D_2 line at 852 nm shown in Figure 4.10. The $F = 3$ and $F = 4$ states of the $6^2S_{1/2}$ ground-level hyperfine manifold serve as the initial and storage states $|g\rangle$ and $|s\rangle$ respectively. These two ground states are dipole decoupled [148] and separated by 9.2 GHz. This large ground state splitting is due to the strong magnetic dipole coupling between the nuclear and electronic spins and has been made famous by their use as *clock states*[5]. This relatively large splitting is the

[5]The second is defined as being equal to the time duration of 9,192,631,770 periods of the radiation corresponding to the transition between the two hyperfine levels of the fundamental unperturbed ground-state of the caesium-133 atom [149].

largest of all stable alkali metals[6]; when used in the Raman Λ memory protocol, the ground state splitting bounds the possible memory bandwidth since the signal and control pulses must not be so broadband as to address both the initial and storage states simultaneously.

We connect the two ground states with the $D2$ line via the upper $6^2P_{3/2}$ manifold which comprises of four hyperfine states $F = 2, 3, 4$ and 5. These states, are separated from one another by approximately 200 MHz [151] are not resolved in this chapter's memory experiments due to Doppler broadening at room temperature. This allows us to treat the upper level manifold as the single excited state $|e\rangle$.

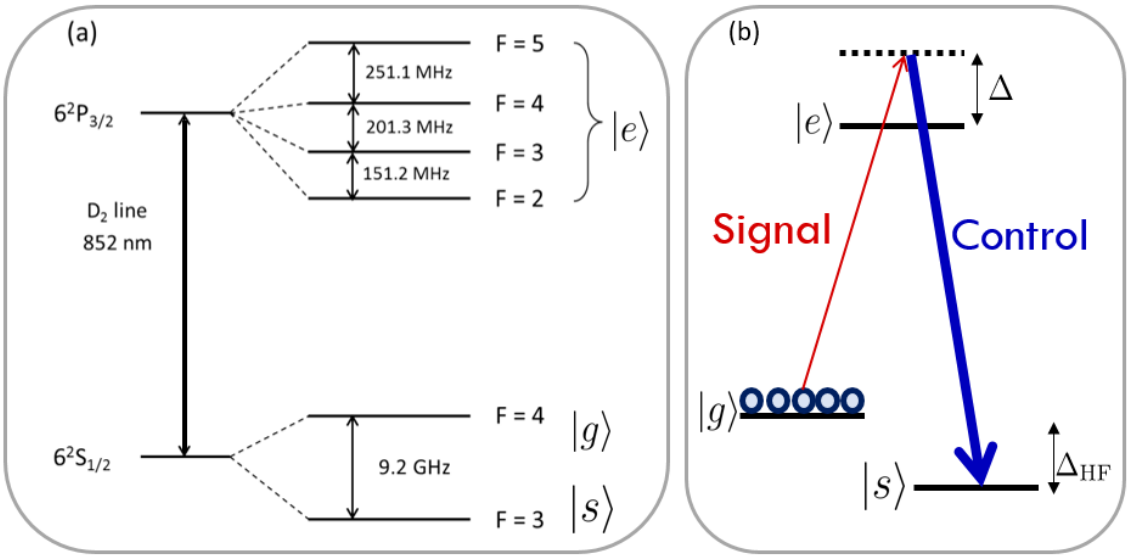

Figure 4.10: (a) Hyperfine structure of the caesium D_2 line (not to scale). The frequency splittings of the excited states are taken from [151]. (b) Energy level diagram of the Raman memory where the signal and control are detuned by Δ from the excited state.

Caesium has historically been used in the Raman memory experiments performed by the research group; chosen as it is the heaviest stable element in the group of alkali metals and thus has the longest diffusion time. Since the storage acts as a spatial hologram, the memory

[6]Francium has a larger ground state splitting, but the most stable isotope (Fr 223) has a half-life of approximately 22 minutes [150].

lifetime is fundamentally limited by this diffusion in the z direction – a process known as Doppler dephasing[7]. A buffer gas of 5 Torr[8] of N_2 is mixed with the caesium vapour to increase this diffusion time. Collisions with nitrogen atoms are spin-preserving and therefore do not affect the hyperfine Raman coherence, since no magnetic dipole interaction can occur between the caesium and the nitrogen nuclei. The effect of the collisions is that the caesium atoms experience a random walk and hence extend the diffusion time, ultimately extending the lifetime by this mechanism to of order tens of microseconds.

The vapour is contained inside a cylindrical glass cell of length 7 cm and with anti-reflection-coated windows and placed inside a μ-metal shield such to protect the spin-wave from magnetic dephasing. The optical depth d, introduced in Section 2.2.6 dictates the interaction strength of the memory interaction. We therefore heat the vapour to 83 °C yielding an on resonance optical depth of 3.65×10^4. The temperature of the cell was adjusted using an ohmic heating system of counter-wound wires which cancel magnetic fields arising from the heating current and maintained using a constant voltage source until an equilibrium temperature was reached.

Optical Pumping

The initial step in any storage process by the Raman memory is to prepare the atomic ensemble into the inital ground state ($F = 4$ of the $6^2S_{1/2}$ manifold) by optical pumping. Since memory efficiency is dictated by coupling constant it is beneficial to maximise the caesium number density (and therefore optical depth) by increasing the temperature. This increased temperature however has the negative impact of limiting the maximum pumping

[7] This will be examined in more detail in Section 6.1. This is the process which results in the dehabilitatingly short lifetime in the ORCA memory protocol in warm vapour.

[8] Torr is a historic unit of pressure equal to 133.32 Pa.

efficiency via a process known as *radiation trapping* [152,153]. At low atomic number-density, continuous excitation of one of the ground states via a pumping laser will eventually result in a spin polarised ensemble; at high atomic densities however, this emitted photon has an increased probability of exciting another atom in the ensemble – hence limiting the maximum pumping efficiency.

Prior to my time in the group, S.E.T. demonstrated a method known as *quenching* [154] whereby a molecular buffer gas provides a non-radiative decay pathway of the atoms from the excited state. It was shown that by pumping on the $D_1(895\,\text{nm})$ line one can achieve spin-polarisation in excess of 99.5% up to 90 °C. [136] By utilising this method we achieve the high pumping efficiency of 99.85% used in this experiment.

Optical pumping is achieved with a Toptica distributed feedback diode laser (DFB) which has a linewidth of 4 MHz and is demonstrably stable to within 10 MHz over days. The laser linewidth is significantly smaller than the Doppler-broadened transition and as such only a small portion of atoms corresponding to a specific velocity class will be initially pumped.

All atoms in the ensemble will nevertheless be pumped due to collisions between the caesium atoms and the buffer gas causing redistribution of the atoms velocity classes. Over the course of ~ 100 ns each atom will have been of the correct velocity class to be addressed by the pumping laser.

To reduce the possibility of pollution from the pump laser reaching the detectors, the pump beam is counterpropagating with the signal and control pulses. The pumping field would obviously have a detrimental effect on the storage spin-wave so an EOSpace fibre-based electro-optic modulator (EOM) is used to switch the pumping on and off. The EOM

achieves an extinction ratio of 200:1 with a rise-time of approximately 5 ns. Over the course of experiments I completed in the group the EOM degraded limiting the extinction – this ultimately limited the memory lifetime in this chapter's experiments to ~ 625 ns.

Pulse Preparation

Operating at the *magic detuning* fixes the detuning of the signal and control to $\Delta = -18.4$ GHz. To benchmark the efficiency of the suppression scheme we shall perform identical measurements at $\Delta = +18.4$ GHz in the standard configuration. This ensures that the coupling of the memory interaction is the same, the pumping and state preparation doesn't need to change, and minimal alterations are required for the filtering.

To begin we carve three 10 ns pulses from a Toptica DL Pro external-cavity diode laser (ECDL), which we are able to set to the control frequency using a HighFinesses wavelength meter. The exact mechanism for carving is described in the following chapter but as an overview, pulses are carved from the continuous ECDL laser using a fibre EOM. The pulses are then amplified using a tapered amplifier (TA).

The two-photon resonance condition of the Raman interaction requires that the frequencies of the control and signal pulses are separated by hyperfine splitting of the ground states $|g\rangle$ and $|s\rangle$. Modulating another EOM in the signal arm, sidebands are generated at ± 9.2 GHz from the central frequency of the control. The red-detuned sideband corresponds to the signal frequency which is isolated the from the other frequency using an air-spaced planar Fabry-Perot etalon with a free spectral range (FSR) of 36.8 GHz. The blue-detuned sideband is shown to be attenuated by $\sim 10^{-2}$ relative to the signal frequency [80] by angle-tuning the etalon.

The signal arm is delayed relative to the control by 250 ns such that the first pulse through the signal arm overlaps with the second pulse on the control arm (as shown in Figure 4.9). These are recombined on a second PBS prior to the memory. The orthogonally polarised[9] signal and control pulses are then focused to a waist radius of $w_0 = 130\,\mu\text{m}$ in the centre of the caesium vapour cell. This waist was chosen such that the Rayleigh range, $z_R = \pi w_0^2/\lambda$, is equal to the length of the cell ($\approx 6\,\text{cm}$).

Filtering, detection and measurement

Of the utmost importance for successful demonstration of a quantum memory is the unadulterated detection of the signal – free from any contributions due to extraneous sources. Firstly the pump laser is counter propagating to the signal, but to ensure the signal remains isolated; a narrow-bandpass filter $840 - 860\,\text{nm}$ is used to isolate the 852 nm signal from the 895 nm pump light.

As mentioned above the strong control pulse is orthogonally polarised to the signal. Initial filtering of the control can be achieved with a calcite beam displacer which provides 50 dB extinction of the control. The signal is then coupled into a single-mode fibre in order to ensure spatial isolation. The control is then spectrally removed from the signal with a series of air-spaced Fabry-Perot etalons; two of which have FSR of 18.4 GHz, and a third with an FSR of 103 GHz and each of which are double passed. 18.4 GHz FSR is chosen to maximally suppress the control field (which is 9.2 GHz away from the signal).

I designed the etalon configuration shown in Figure 4.11 which, combined with temperature tuning the 18.4 GHz etalons, meant transmission of each pass through the etalons 1 and 2 was 90%, and 70% through etalon 3. This yielded a factor of 20 improvement on previous

[9] As required by the selection rules for the Raman memory interaction [119].

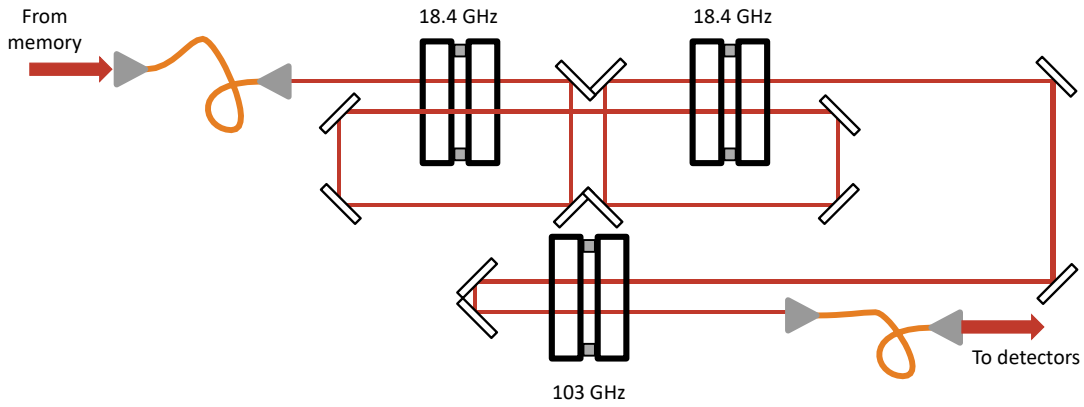

Figure 4.11: Configuration of the planar Fabry-Pérot etalons with fixed spacers as seen from above, comprising of 3 etalons all double passed, two with free spectral range of 18.4GHz to maximally suppress the control and another with 103GHz to filter spontaneous emission (from both the atoms and the tapered amplifier).

iterations, with total transmission increased from 0.5% to 10% with the temperature stability provided by Oxford Instruments MercuryiTC temperature controller. The enhanced stability of this design was critical in allowing the multiple-hour long measurements required to calculate photon-statistics for low photon numbers.

Following the polarisation and spectral filtering, the signal is coupled into a multi-mode fibre and detected using a single-photon avalanche photo-diode (APD) with a QuTools QuTAU photon counting module. This enables us to generate histograms for photon arrival times across multiple runs of the three-pulse train. When measuring the $g^{(2)}$ a PBS is added and a second APD used, as shown in Figure 3.1.

The average photon number of the coherent state incident on the memory can be estimated by accounting for all transmission losses between the front of the vapour cell and the detector - including the APD detection efficiency ($\eta_{\text{det}} = 45\% \pm 5\%$). Hence we estimate N_{in} as:

$$N_{\text{in}} = \frac{N_{\text{det}}}{T_{\text{tot}} \cdot \eta_{\text{det}}} \tag{4.23}$$

where the total transmission $T_{\text{tot}} = T_{\text{smf}} \cdot T_{\text{etl}} \cdot T_{\text{mmf}}$ where the total transmission is (respectively) the product of the single mode fibre coupling efficiency, the etalon system's transmission and the coupling efficiency into the multi-mode detection fibre prior to the APDs.

There are 3 shutter configurations of interest using the shutters shown in Figure 4.9:

1. Shutter 1 closed – just the signal incident on the memory. This enables us to record just the input signal, and calculate the number of signal photons incident on the memory: N_{in}.

2. Shutter 1 & 2 open – both the signal and control pulses are incident on the memory. This is the configuration at which storage occurs and the ratio of the retrieved signal to the incident signal from configuration 1 yields the memory efficiency: η

3. Shutter 2 closed – just the control field pulses incident on the memory. This measures the noise generated in the output bin by just the control: $N_{\text{spont}} + N_F$.

Looking at Equation 4.22 and Table 4.1 we can see these sets of measurements, provide all the required data to produce a model for the $g^{(2)}$ as a function of N_{in}.

4.4.2 Results

Memory operation for the standard Raman and noise suppressive absorption cases are tested via the storage of weak coherent states using the experiential set-up described and shown in Figure 4.9. Using pulses of 10 ns FWHM and a storage lifetime of 150 ns, Figure 4.12 shows a typical arrival time histogram of the memory experiment with a weak coherent state and a memory efficiency of $\approx 15\%$. The three histograms correspond to the three shutter

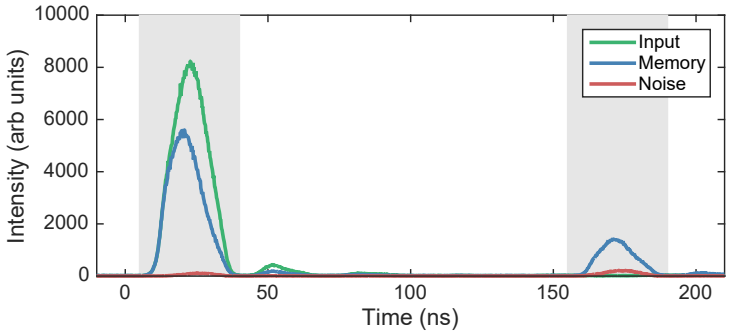

Figure 4.12: Typical histogram plot for memory experiment. Green corresponds to configuration 1 (input signal), blue to configuration 2 (memory on) and red to configuration 3 (spontaneous noise). Due to the nature of the carving shown in Figure 4.9, the shape of the control pulses (both read-in and read-out) follow the signal pulse exactly, including the small ringing after the primary pulse.

configurations described. The counts for each bin (binwidth = 81 ps), for each combination of fields, is found by summing the histograms within the shaded integration window (set to 35 ns).

Allowing for less than perfect filtering, photons, both from the control and fluorescence induced by the control, can reach the detector. In order to calculate the memory efficiency we must take these into account. Labelling the 3 shutter configurations as subscript $(1, 2, 3)$ and the two integration windows as superscript *in* and *out* we have that the counts from the input signal is N_1^{in} experimental efficiency is:

$$\eta = \frac{N_2^{\text{out}} - N_3^{\text{out}}}{N_1^{\text{in}} - N_3^{\text{in}}}. \tag{4.24}$$

This takes into account any control induced noise photons and we have implictly assumed that the amount of control field leakage and fluorescence is independent of the signal field. We can also calculate the μ_1 parameter. As stated in Chapter 1, the μ_1 represents the noise-to-signal ratio for a retrieved state from the memory and is given by

$$\mu_1 = \frac{\langle n_{\text{noise}} \rangle}{\eta} = \frac{\langle N_3^{\text{out}} \rangle}{\eta} \tag{4.25}$$

where the expectation value is the number of noise photons per trial; but it's important to remember that the true metric for a noise-free memory would be the fidelity of the retrieved state compared to the input.

Before looking at the effectiveness of our noise suppression scheme, we will first examine the memory performance itself, namely lifetime and efficiency. These measurements were taken in partnership with S.E.T and hence some of which also appear in [120].

Storage Time

The top graph in Figure 4.13 shows the memory lifetime by plotting how the efficiency changes by delaying the read-out control pulse with respect to the read-in. The efficiency experiences the expected exponential decay, in these cases due to the imperfect suppression of the pump beam by the EOSpace EOM. The residual pump field obviously empties the storage state and hence depletes the stored spin-wave. The lifetimes for the two cases would be expected to be the same, however due to the photorefractive damage to the EOM, the extinction varied in the measurement of the two cases. The calculated $1/e$ decay time for the absorptive configuration is 625 ± 36ns compared to 294 ± 26ns in the standard case.

Whilst measuring the memory lifetime (configuration 2) we can also study how the number of noise photons caused by the second control pulse (configuration 3). We note that the noise in the standard Raman decays as the gap between the two control pulses increases whilst the noise is constant (and significantly less) in the absorptive case. The decay lifetime is calculated to be 380 ± 36ns which is comparable to the memory lifetime;

this is consistent with the supposition that a significant portion of noise comes from a spurious spin-wave being created by the read-in control pulse. The noise during read-in is constant with storage time in both cases – but significantly lower in the absorptive case. This is of course unsurprising, the read-out control pulse should have no impact on the read-in.

Using Equation 4.25 we can see how the μ_1 parameter varies with storage time. For all storage times the μ_1 is significantly lower in the absorptive case which is shown in the bottom panel of Figure 4.13. The μ_1 comparison shows that, despite the lower efficiency, the impact of the noise suppression scheme is clearly evident.

Control pulse power

The control pulse energy used for the lifetime measurement in Figure 4.13 was 930 pJ which we saw the effect that the efficiency is lower in the absorptive case. We can examine this in detail by investigating how the efficiency varies with control power. Figure 4.14 shows the result of this experiment and corresponding simulation. We again see the large discrepancy between the efficiencies which we attribute to two factors. Firstly there is a subtle difference between the two configurations, despite the coupling strengths being equal (as the magnitude of the signal's detuning is equal), the control field when using the *magic detuning* is significantly closer to an atomic transition. As shown in Figure 4.5 the control is only 9.2 GHz detuned leading to a much more significant impact caused by the AC-Stark shift (we recall this is quantified by $|\Omega|^2/\Gamma$ as seen in Equation 2.40). At low control field powers the efficiency is expected to scale quadratically with power – as indeed it does – shown in Figure 4.14. With increasing control field power, however, the A.C. Stark shift

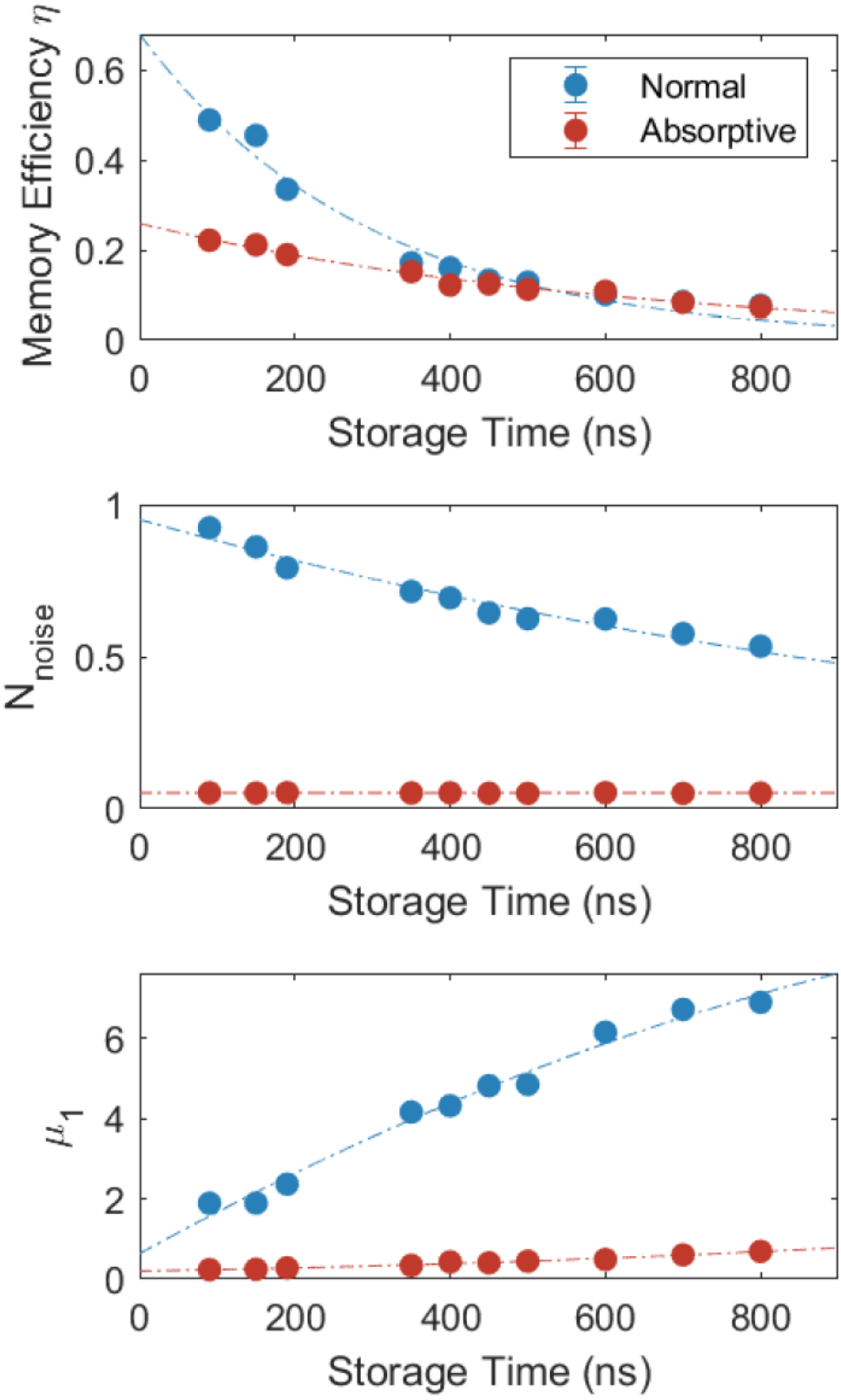

Figure 4.13: Top: Decay of memory efficiency with storage time in the normal and absorptive Raman cases. Dashed lines refer to the calculated $1/e$ decay times. Middle: Number of noise photons in the readout bin as a function of storage time. Dashed line is a fitted $1/e$ decay time in the standard configuration and a constant value in the absorptive case. Bottom: How the μ_1 varies with storage time. Dashed line calculated from the upper plots using Equation 4.25. The control pulse energy is 930 pJ in both cases and the error bars are within the marker size.

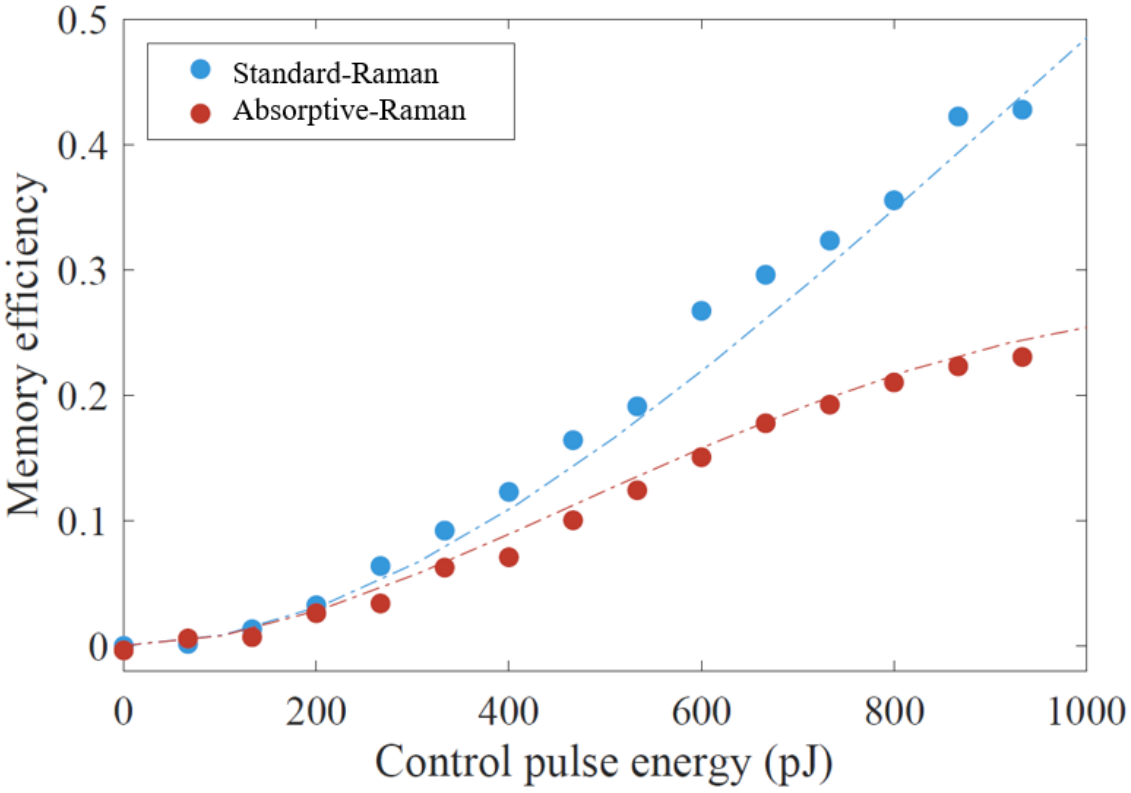

Figure 4.14: Memory efficiency as control pulse energy varies in absorptive (standard) case shown in red (blue). The average photon number is (3.5) 3.2 for the coherent states used and the memory storage time is 150 ns. Experimental parameters such as pumping efficiency, cell temperature were the same between experiments. Dotted lines show efficiency from numerical simulations performed with the same parameters as described in Section 2.5.

begins to perturb the Raman resonance, thus limiting the attainable memory efficiency. If the control Rabi frequency is increased further, the efficiency reaches a maximum value for a given optical depth, and this is the rollover that can be starting to be seen when using the noise suppression scheme. The same rollover would be observed for the standard Raman, but at a higher power/efficiency.

In the following chapter we shall look at how shaping the signal field[10] can compensate for the AC-stark shift and remove this maximum efficiency limit [144].

[10] As determined by the principle mode of the calculated Green's function and its single value decomposition – discussed in 2.5.2.

As well as the AC-Stark shift reducing efficiency the second thing to remember is that the measured efficiency (and the efficiency in simulations) does nothing to remove the *non*-spontaneous noise or (alternatively) gain-like noise. These would be signal photons that are produced via the FWM pathway, seeded by the input signal. We first encountered this using our rudimentary definition of noise from Equation 4.20 and we see it again here. The efficiency in the standard Raman is necessarily higher because it includes these contributions (indeed the recorded efficiency in these cases could exceed 100% as shown here [136]).

We can again study the impact on the number of noise counts N_{Noise} per pulse in the read-out bin by varying the control pulse energy. Figure 4.15 shows the number of noise photons growing quadratically in the standard Raman configuration and linearly when at the *magic detuning*. This is the second instance of radically different behaviour in N_{Noise} between these two schemes. Firstly the constant vs the exponential decay of the noise in Figure 4.13 and now the linear vs quadratic increase in noise with control pulse energy. A quadratic gain is indicative of the Raman coupling and hence four-wave mixing noise whilst the linear scaling in the absorptive case suggests simply technical such as fluorescence.

The information garnered investigating the behaviour of noise as storage time and control power vary all indicated that the anti-Stokes field is being suppressed and hence four-wave mixing is not happening when the *magic detuning* is chosen. Furthermore despite (apparent) lower efficiency the measured μ_1 is also significantly improved, showing that this choice of detuning doesn't appear to be prohibitive to storage. We now move to the measurement of photon statistics and the experimental procedure outlined in at the start of this section.

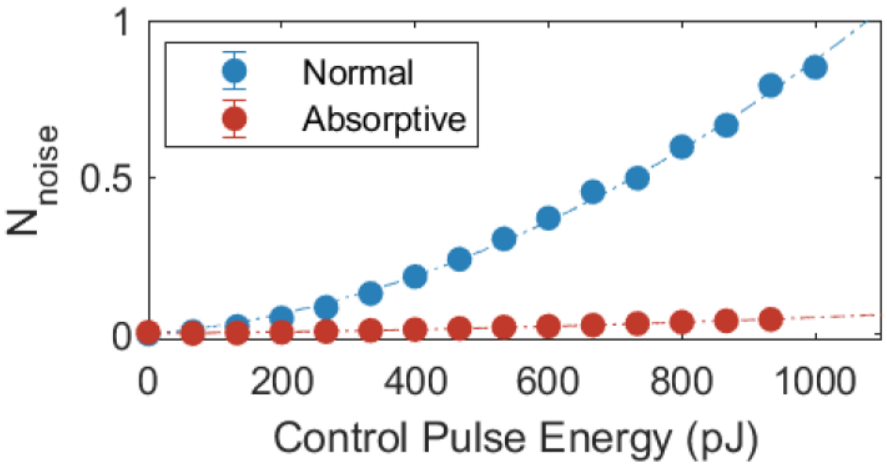

Figure 4.15: Number of noise photons as control pulse energy varies in absorptive (standard) Raman case shown in red (blue). The memory storage time is 150 ns. Dotted lines show a proportional (quadratic) fit.

Photon statistics

We now experimentally measure the $g^{(2)}$ using the formula in Equation 3.7 using a Hanbury-Brown-Twiss set-up. Practically this involved putting the output of the memory on a 50:50 beam splitter and using a fibre-coupled avalanche photodiode on each output. The correlation function and coincidence logic was measured using a Swabian Instrument TimeTagger 20.

The measurements are performed with a storage time of 150 ns and control pulse energy of 330 pJ with 10 ns FWHM pulses. The relatively long storage time ensures no cross-talk in the correlation measurement. Figure 4.16 shows the result on the output $g^{(2)}$ of varying the average photon number of the coherent state input between $N_{\text{in}} \approx 0.5$ and $N_{\text{in}} \approx 80$. We also include a $g^{(2)}$ measurement of no input state (configuration 3), measuring the statistics of N_{noise}. Since the number of photons in N_{noise}, and for small input states is low, in order to gain meaningful results with a low Poissonian error, measurements had to be taken for

many hours[11].

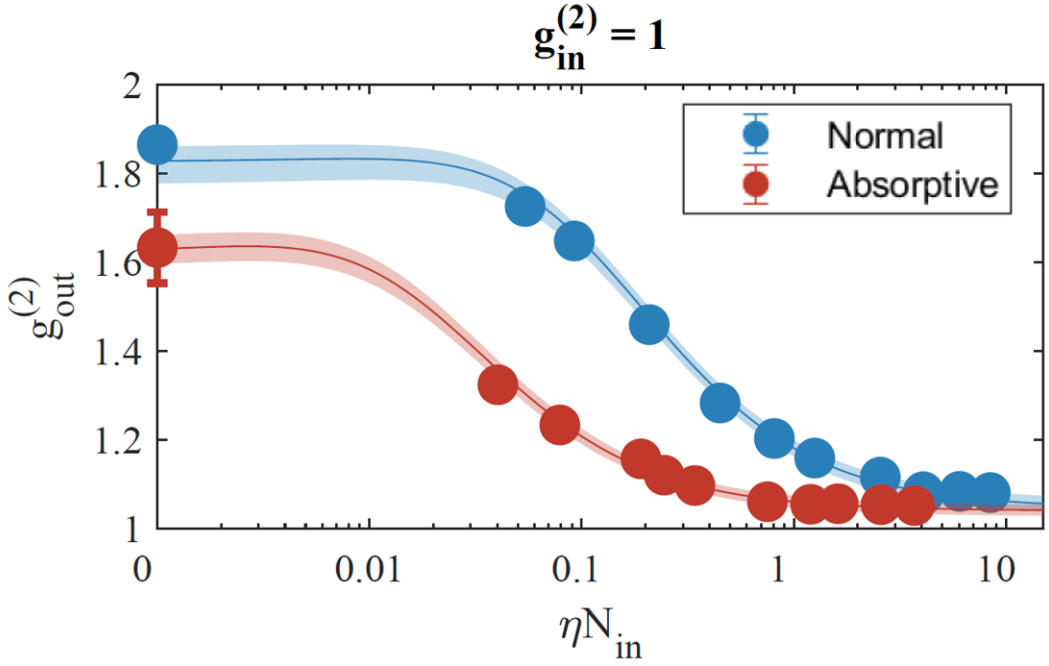

Figure 4.16: Output $g^{(2)}$ as a function of size of the coherent input states used N_{in}. The memory storage time is set at 150 ns, with control pulse energy and duration at 330 pJ and 10 ns FWHM. The shaded regions around the solid line show a 95% confidence region around the fit to Equation 4.22.

The measurements taken allow us to fit the parameters in Table 4.1 and Equation 4.22. The result of this fit is also shown in Figure 4.16 with the 95% confidence region shown by the shaded regions.

The two free parameters in our fitting are $\mathbb{G}_{ss}$ and the ratio of N_{spont} to N_F, as everything else is constrained by direct measurements. We remind ourselves that N_{spont} comprises of both spontaneous Raman scattering due to imperfect pumping and spontaneous FWM. In principle a decrease in $\mathbb{G}_{ss}/\eta^2$ would also signify a reduction in four-wave mixing since it describes the gain process. We do see a small reduction in the calculated parameter $\mathbb{G}_{ss}$ going from $11.0(2) \times 10^{-3} \rightarrow 10.9(1) \times 10^{-3}$ but the uncertainty on these measurements

[11] Allowed by, in part, the increased stability of the filtering etalon setup and the fibre EOM used to carve the pulses.

and the relatively low efficiency (10.2%) and control power restrict the implications that we can draw from this measurement.

Before describing the other results of the fit, it is worthwhile to see if we can separate the two components of spontaneous noise. To do this we measure N_{noise} as a function of pumping efficiency α. This relationship is shown in Figure 4.17 along with the predicted linear relationship. By extrapolating the pumping efficiency to 100% we are able to extract the contribution caused by spontaneous four-wave mixing.

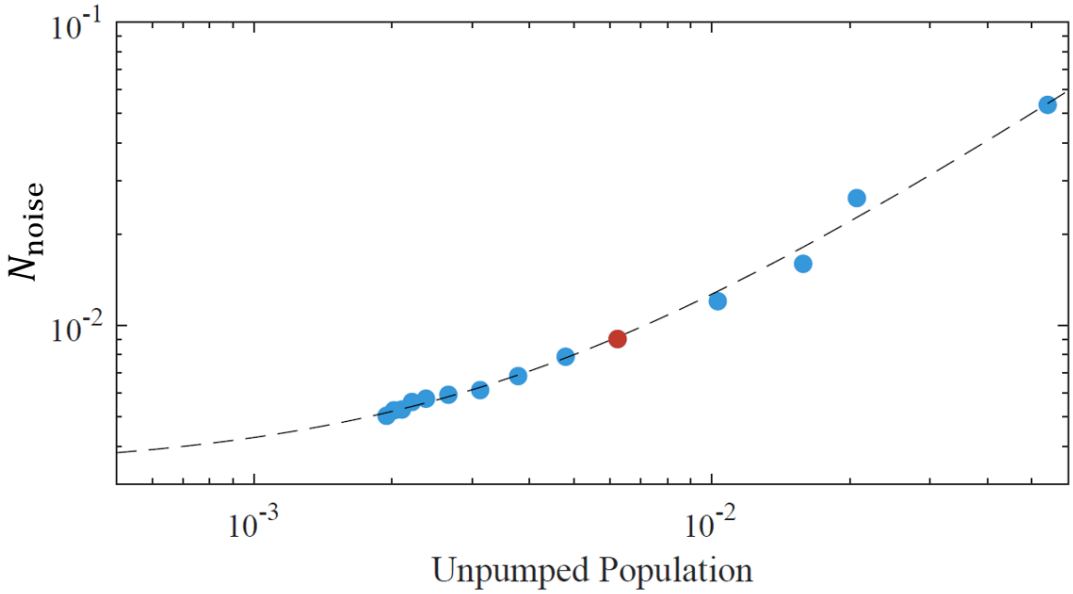

Figure 4.17: Number of noise photons produced by control pulse as a function of pumping efficiency (α). Dashed line shows the expected linear fit. The red data point indicates the pumping efficiency that was used for the $g^{(2)}$ results presented in this chapter.

The reduction in the amount of noise is summarised in Table 4.2, showing dramatic reduction in not only the raw noise counts but also the ratio of spontaneous noise to fluorescence noise. Furthermore we can estimate how much of N_{Spont} is produced by imperfect pumping. The extrapolation from N_{noise} indicates that with perfect pumping, the remaining noise (from spontaneous FWM and fluorescence) would be $(5 \pm 2) \times 10^{-3}$ photons per pulse.

This is in good agreement to the $(3.8 \pm 0.5) \times 10^{-3}$ noise photons per pulse attributed to fluorescence; indicating we have all but eradicated noise from four-wave mixing! Pumping efficiency and spectral filtering of fluorescence become the remaining limitations.

Table 4.2: Table showing how the noise in the readout time bin compares, as calculated from the fit to Equation 4.22. The parameters for this comparison were chosen to be as close as possible, including pumping efficiency, coupling strength and control pulse energy. Due to the nature of the noise suppression scheme the detuning of the control is different in the two cases; in the standard configuration it is 27.6 GHz detuned from the populated transition compared to only 9.2 GHz in the absorptive case.

	$N_{\mathrm{Noise}}(\times 10^{-3})$	$N_{\mathrm{Spont}}(\times 10^{-3})$	$N_{\mathrm{F}}(\times 10^{-3})$
Standard Raman	90.0	81 ± 2	9 ± 3
Absorptive Raman	14.8	11.0 ± 0.4	3.8 ± 0.5

4.4.3 Outlook

As can be seen from Figure 4.17 at the time of the $g^{(2)}$ measurements, our pumping efficiency (and by extension the spontaneous noise) is not the best recorded value. This pumping efficiency could potentially be improved further; we intend to use a high speed Pockels cell to switch the pumping on and off. A Pockels cell would enable both a higher power when the pump is "on" and a better extinction ratio, thereby both the efficiency and noise level due to imperfect pumping will improve.

So whilst we have demonstrated that operating the memory at this *magic detuning* significantly reduces the noise, we have not yet answered the question *"is single photon storage possible?"*. We know that in previous experiments FWM was identified as the limiting factor in single-photon storage so it is important to see if it is now possible. From our experiments we have determined all of the parameters in Equation 4.22. We can change our memory input from a coherent state with $g^{(2)} = 1$ and an average photon number $\langle \alpha \rangle = N_{\mathrm{in}}$ to a single photon $g^{(2)} = 0$ and some probability of being incident on the memory

which we call heralding efficiency η_h. We use heralding efficiency as a nod towards using parametric down conversion as a heralded single photon source but would be completely analogous to probability of single-photon generation by other means such as quantum dots.

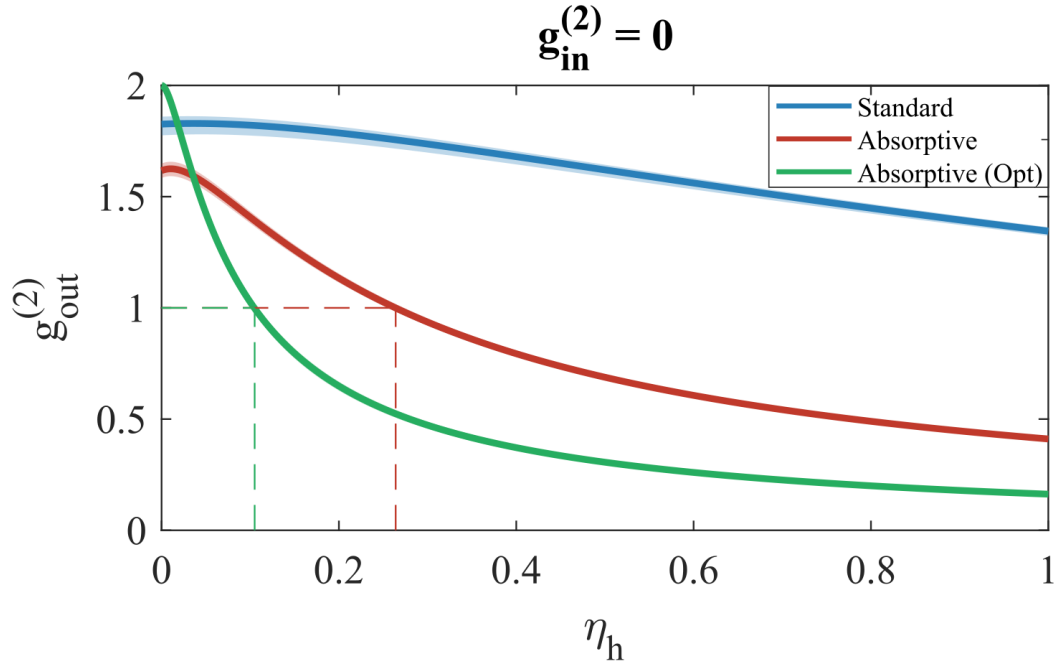

Figure 4.18: Output $g^{(2)}$ as a function of heralding efficiency of an input single photon with a $g^{(2)} = 0$. The memory storage time is set at 150 ns, with control pulse energy and duration at 330 pJ and 10 ns FWHM. The shaded regions around the solid line show a 95% confidence region around the fit to Equation 4.22. The green shows an optimised scenario where noise associated to imperfect pumping is at the minimum recorded level.

Figure 4.18 shows the effect of varying heralding efficiency on the $g^{(2)}$ of the retrieved state from the memory. We note that even when the signal is certainly a single photon ($\eta_h = 100\%$) the standard Raman memory conditions are unable to produce a non-classical retrieved state – as predicted. We also see that our suppresion scheme has worked! When a photon has a greater than 26.4(5)% probability of being input to the memory, the retrieved state will have non-classical statistics. Furthermore, by improving the pumping to the level demonstrated in Figure 4.17 we can acheive the green curve shown in Figure 4.18. This

drops the required heralding efficiency for $g^{(2)} < 1$ to 6.5(6)% or would, in the case of a deterministic photon source, retrieve a state with $g^{(2)}_{\text{out}} = 0.14 \pm 0.02$. This optimisation would give a $\mu_1 = 0.05$, which can be used to calculate an upper bound of $\mathcal{F} = 0.95$[72] for the fidelity of the retrieved state, compared to the input state.

The final question remains, before attempting single photon storage in the future, *"can the noise level get any lower?"*. We have removed (to the limit at which we can distinguish it) four-wave mixing noise; a Pockels cell improves the noise from imperfect pumping; what remains is the technical noise from the control interacting with atoms and producing fluorescence noise N_{F}. We recall that the first 2 Fabry-Perot etalons in Figure 4.11 (and we pass through each one twice) are designed to maximally suppress the control field 9.2 GHz away by having an FSR of 18.4 GHz. The *magic detuning* is of course $\Delta = -18.4$ GHz meaning that when the etalons are aligned with the signal they are also spectrally aligned with the atomic transition[12]. Future iterations of the experiment will incorporate etalons that have an FSR of 40 GHz such to effectively filter this on resonant fluorescence.

4.5 Conclusions

This chapter has focused on a specific method to eliminate four-wave mixing from the Raman memory whereby I have outlined possible methods that have been considered before focusing on the method of atomic absorption. This method works by arranging the fields such that the undesired anti-Stokes scattering is on resonance with the populated transition. This is done by selecting a so called *magic detuning* for the signal (and by extension the control).

[12] We note that by definition they are aligned with the anti-Stokes field, and historically AS photons would be recorded by the single photon detector, leading to the addition of the 103 GHz etalon. This was before the realisation of four-wave mixing's detrimental effect on the non-classicality of the stored state.

To test this method I completed extensive theoretical modelling, considering the ideal equations of just the memory interaction, and comparing the simulations to models with the full equations. Opting to investigate the memory at $\Delta = \pm 18.4\,\mathrm{GHz}$ where the minus sign indicates the *magic detuning* and we investigate at the positive detuning as that has the same coupling strength, allowing a comparison for the noise suppression scheme.

I then designed a experiment using the statistics of the output of the memory to benchmark the success of the suppression. Completing the experiment I demonstrated both a dramatic change in the noises' characteristics as well as an order of magnitude drop in noise. All indicative of the noise suppression method working as intended. Finally I used the information gained from studying the memories' behaviour with weak coherent states to infer the retrieved state's properties if a heralded single photon was used as an input. This allowed me to predict non-classical recall if the probability of a single photon incident to the memory is greater than $(26.4 \pm 0.5)\%$, which can be reduced to $(6.5 \pm 0.6)\%$ after some small improvements to the experimental pumping design. The remaining noise is attributed to fluorescence and I suggest some ways to investigate and reduce that noise, further improving either the required heralding efficiency or the non-classicality of the retrieved state.

To date, operating the memory at this *magic detuning* has been proven to provide a technically simple means to store a single photon and retrieve it, whilst maintaining the state's non-classicality. These encouraging results pave the way for future single photon experiments.

Chapter 5

Temporal Modes

"Time is the wisest counsellor of all."

Pericles

This chapter details the memory's interaction with temporal modes of light such as those reviewed by Brecht *et al.* [52] and again more recently by Raymer and Walmsley[53]. In this chapter I introduce temporal modes and describe how the memory may be used to utilise them.

5.1 Introduction to temporal modes

In Section 1.2.2 I introduced temporal modes as a degree of freedom that can be used to encode quantum information. To date, approaches towards operating on a qudit basis of TMs are based on non-linear optical interactions. A quantum pulse gate based on dispersion-engineered sum-frequency generation in lithium niobate waveguides has been realised [155] and recent results put forward ways of addressing single TMs with high fidelities [156]. In such a device the addressed TM is converted to a different wavelength and can be subsequently

separated with standard optical components[1]. However, such TM-manipulation devices are limited to pulses of a few pico-seconds or shorter (bandwidths $\gtrsim$ 100 GHz), which are not compatible with many atomic based sources of quantum light (e.g. Quantum dots) which typically operate in the MHz-GHz regime.

After having shown in the last chapter that the Raman memory can operate at a low enough noise level for quantum operation, we can now focus on its applications. In this chapter I explore the memory's capability to store and manipulate temporal modes. In Section 1.3.2 we discussed multi-modality of quantum memories and how, in the context of a field of quantum repeaters, a memory exhibiting this property would enable a larger quantum network. In this chapter I invert that notion and investigate what it implies if a quantum memory is strictly *single*-moded.

5.2 Multi-mode photon statistics

As in Chapter 2 we define our photon Fock state as:

$$\left|n_{\sigma}^{(1)}\right\rangle = \int \frac{\sigma(t_1)(S_1^{\dagger})^n}{\sqrt{n!}} \left|0\right\rangle \mathrm{d}t_1 = \frac{1}{\sqrt{n!}} \int \sigma(t_1)(S_1^{\dagger})^n \left|0\right\rangle \mathrm{d}t_1 \tag{5.1}$$

where the temporal mode is given by $\sigma(t)$ where $\int |\sigma(t)|^2 \mathrm{d}t = 1$. The simplest description is that σ represents the electric field profile of the pulse, but temporal modes could equally be described by the Fourier transform in frequency space. If we consider the infinite set of Hermite-Gaussian modes, derived from Hermite polynomials[158], we can use them to develop an infinite dimensional Hilbert space.

[1] See [157] for a review on the quantum pulse gate.

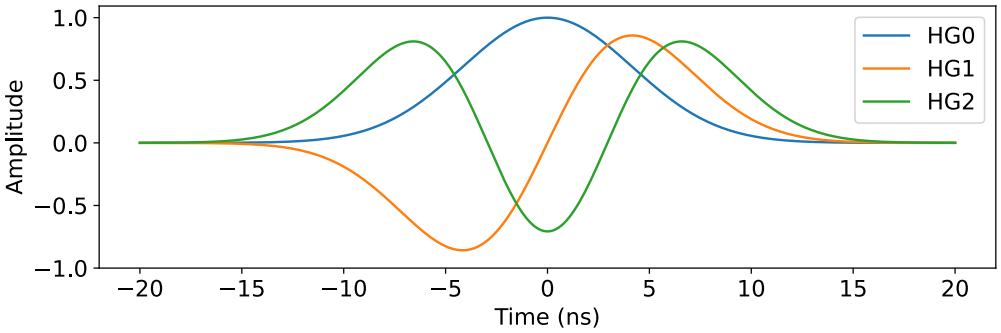

Figure 5.1: The first three Hermite-Gaussian temporal modes, where the zeroth mode is a Gaussian pulse with $t_{\mathrm{FWHM}} = 10\,\mathrm{ns}$

Figure 5.1 shows the 0th, 1st and 2nd order Hermite-Gauss modes, and it is important to reiterate that even though these modes fully overlap in polarisation, space, frequency, time and spatial mode, they are orthogonal with respect to a time/frequency integral. This property also makes them, as a basis, insensitive to stationary or slowly varying medium perturbations such as linear dispersion [52].

It is clear from Equation 5.1 that two orthogonal temporal modes (say σ and δ) will not interfere, and as such we can use a HOM interference to determine the overlap between two single photons of unknown temporal modes, as discussed in Section 1.2. This is a purely one-dimensional metric however. To decompose an unknown temporal mode into the Hermite-Gauss basis would require some degree of tomography.

5.2.1 Distinguishing temporal modes

We consider a method for quantifying the overlap between two temporal modes, an experimental setup for which is shown in Figure 5.2. Instead of single photon states, we instead consider weak coherent states. Two temporal modes with pulse width t_{FWHM}, separated by Δt (with $\Delta t \gg t_{\mathrm{FWHM}}$) are incident on an unbalanced Mach-Zender interferometer. The

outputs of the second beam-splitter are sent to single-photon counting module and coincidences between the two detectors are recorded. If we label the pulses as 1 and 2, and the paths as early e and late l we can see there will be 3 time-bins of interest.

Table 5.1: Table showing the detection time-bins possible from the experimental arrangement in Figure 5.2.

Time-bin	Pulse, path	Arrival time
1	$1, e$	0
2	$1, l$ and $2, e$	Δt
3	$2, l$	$2\Delta t$

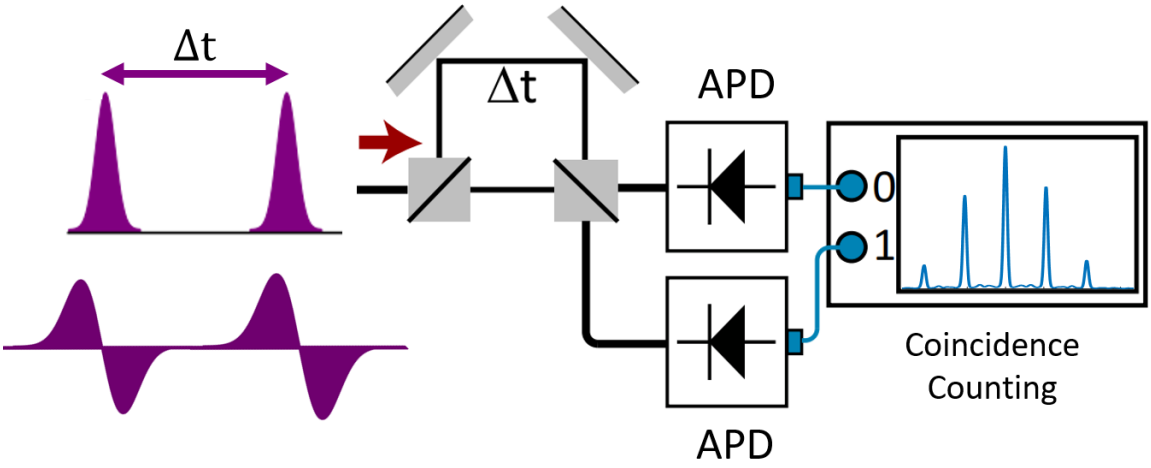

Figure 5.2: Experimental arrangement for quantifying the overlap fo two temporal modes of weak coherent states. Two successive pulses are incident on an unbalanced Mach-Zehnder and coincidneces between the two output ports are detected by detectors $D1$ and $D2$. Figure adapted from [159].

We can also look at coincidences between the two detectors in Figure 5.2, and we note that there will be 5 possible times for coincidences between the two detectors $D1$ and $D2$. The simplest are for coincidences separated by $\pm 2\Delta t$. These can only occur by $D1$ firing in time-bin 1 and $D2$ firing in time-bin 3 (and vice-versa). A separation of $\pm\Delta t$ can occur for $D1$ firing in time-bin 1 (or 2) and $D2$ in time-bin 2 (or 3). Finally, the most interesting case is for zero time between detectors firing. Because we are considering coherent states, each pulse could split at the second beam-splitter, creating a coincidence with zero delay.

Additionally, pulse 1 can take the longer path and pulse 2 can take the shorter path; both pulses will arrive at the final beam-splitter at the same time. This is where we can look for HOM interference.

HOM interference, described by Equations 1.3-1.6, occurs when two single photons are incident on a beam-splitter. The probability of them exiting from different ports is given by $p_{1,1} = \frac{1}{2}\left(1 - |\langle\psi_a|\psi_b\rangle|^2\right)$ (i.e. they *bunch* when identical). If pulses 1 and 2 were comprised of single photons then the only time a coincidence could occur would be when there was some degree of distinguishably between the photons. However, using coherent states complicates matters. A coherent state with, average photon number $\langle n\rangle = |\alpha|^2$, is written in the Fock basis as:

$$|\alpha\rangle = e^{-\frac{|\alpha|^2}{2}} \sum_{n=0}^{\infty} \frac{\alpha^n}{\sqrt{n!}} |n\rangle \,. \tag{5.2}$$

The probability of an individual pulse to have n photons in is therefore given by:

$$P(n) = |\langle n|\alpha\rangle|^2 = e^{-|\alpha|^2} \frac{|\alpha|^{2n}}{n!}. \tag{5.3}$$

If a small α is used, then there will be a significant number of occasions when both pulses will contain just a single photon. When both pulses contain a single photon, assuming that the photons are indistinguishable, bunching occurs and the number of coincidences seen with zero delay is reduced.

Experimentally, the degree of indistinguishability can be quantified from the mean areas

of the correlation peaks (-2,-1,0,1,2) in Figure 5.2 which are calculated as [159,160]:

$$A_0 = \left[(R_1T_1R_2^2 + R_1T_1T_2^2)(1+2g^*) - 2V(1+\epsilon)^2R_1T_1R_2T_2\right]$$

$$A_{-1} = N\eta^{(2)}\left[R_1T_1R_2^2(1+2g^*) + R_1T_1T_2^2\right] \quad A_{+1} = N\eta^{(2)}\left[R_1T_1R_2^2 + R_1T_1T_2^2(1+2g^*)\right]$$
$$A_{-2} = N\eta^{(2)}R_1T_1R_2^2 \qquad A_{+2} = N\eta^{(2)}R_1T_1T_2^2 \tag{5.4}$$

where N is the number of repetitions, $\eta^{(2)}$ is a combined $>$ 2-photon per pulse generation and detection efficiency, R and T are the reflection and transmission intensity coefficients of the beamsplitters, $(1+\epsilon)$ is the interferometer visibility and V is the overlap of the two wavepackets. To account for multi-photon events g^* is linked to the multi-photon probability and is given by:

$$g^* = \frac{P(n \geq 2)}{P(n=1)}. \tag{5.5}$$

The two-photon HOM interference is quantified by the areas A_0 and $A_{\pm1}$:

$$M = \frac{A_0}{A_{-1}+A_{+1}} = \frac{1+2g^*}{2(1+g^*)} - V\frac{(1+\epsilon)^2R_1T_1R_2T_2}{(1+g^*)(R_1T_1R_2^2 + R_1T_1T_2^2)} \tag{5.6}$$

where in the case of a single photon ($g^* = 0$), this M parameter varies from 0 to 0.5 as the overlap of two photons varies from indistinguishable to distinguishable ($V = 1 \rightarrow 0$). This range of M assumes perfect interferometer visibility ($(1+\epsilon) = 1$) and a perfect splitting ratio on both beamsplitters ($T = R = 0.5$).

I demonstrated this method experimentally with assistance from J.N.B using weak coherent states with $\langle n \rangle = 1.1$. The interferometer visibility was measured with CW light as

$((1+\epsilon) = 1)$ and the reflectivity of the second beamsplitter[2] was determined to be $R_2 = 0.4$. As V varies from $\{0 \to 1\}$, with these parameters, M varies from $\{0.740 \to 0.499\}$.

5.2.2 Pulse carving

In the pulse preparation section of Section 4.4.1 we described the production of carved pulses using a fibre Mach-Zender interferometer (MZI). Here we expand on that procedure. The input CW field is split equally along both arms of the interferometer and separate phases, $\phi_1(t)$ and $\phi_2(t)$, are applied to each arm before recombining. With full control over the applied phases, we are free to modulate the phases such to generate any arbitrary output pulse of light.

This is achieved experimentally by using a fibre based electo-optic modulator Mach-Zehnder, shown in Figure 5.3. Applying a voltage to an EOM changes the refractive index of the non-linear medium and therefore light undergoes a phase shift which is linearly proportional to the applied voltage. We use two arbitrary waveform generators (Tektronix AWG70000) to generate the necessary time-dependent voltage signals to apply to the EOMs such that we can control the phase shift of the two arms of the interferometer.

The transmitted field has a complex temporal profile $E_{\text{out}}(t)$ which may be expressed as:

$$E_{\text{out}} = \sin\left[\pi\left(\frac{V_1 + V_2}{V_\pi}\right) + \phi_0\right] \exp\left(\left[i\pi\left(\frac{V_1 - V_2}{V_\pi}\right)\right]\right) \tag{5.7}$$

where $V_{1,2}$ is the voltage applied to the respective arm, V_π is the response of the EOM, and ϕ_0 is the bias phase. Ideally the bias phase would be zero; however thermal effects and

[2]This was a fibre beamsplitter whilst the first was a polarising beam cube, allowing us control of the splitting ratio which we set to 50:50.

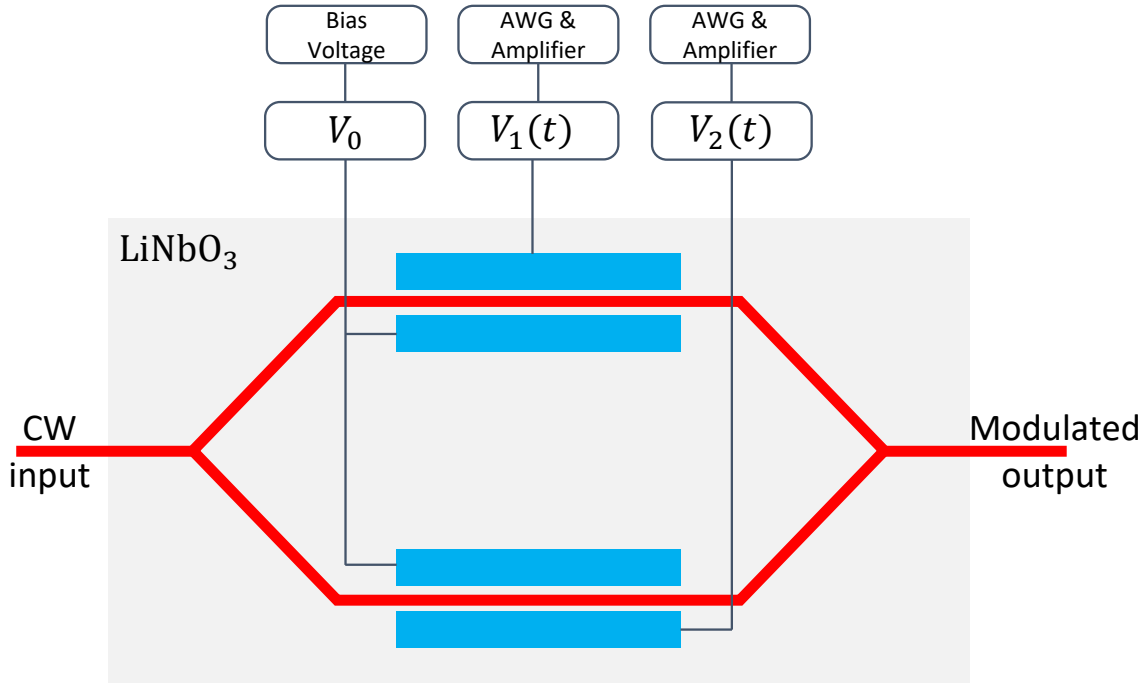

Figure 5.3: Lithium niobate fibre EOM whereby applying an RF field controls the phase on each arm of this Mach-Zender interferometer. Each arm of the interferometer is driven by an arbitrary waveform generator (Tektronix AWG70000), sampling at 50Gs/s. The two AWGs are synchronized (Tektronix AWGSynch) and their outputs amplified with a 10.7Gb/s driver amplifier (PicoSecond Pulse Labs 5868). A bias voltage is used to apply a global phase.

motion of the charge carriers within the EOM cause ϕ_0 to drift. To mitigate this we perform symmetric biasing and apply a square wave $[-V_\pi, +V_\pi]$ at 10 Hz to the bias voltage in order to minimise the macroscopic motion of the charge carriers and stabilise ϕ_0. We monitor the transmission of the EOM using a pickoff and use a gradient ascent/descent algorithm to maximise the pulse visibility by monitoring the intensity and offsetting the square-wave to the bias voltage accordingly. There is a limit to the bandwidth of pulses we can generate experimentally. The signals from the AWGs have to be amplified to drive the EOM and these RF amplifiers have a bandwidth of 12GHz which limits the minimum pulse durations we can carve, smaller than which we begin to see ringing after the pulse. The software interface for this pulse-carving set-up was built by J.D.H.M with details provided in [121],

and the following experiments were conducted by myself and S.E.T, with assistance from J.N.B and P.M.L.

5.3 Experiments with temporal modes

This section will detail the experiments that I conducted with S.E.T (2-4) and J.N.B (1) using temporal modes. All the memory experiments are conducted with the infrastructure described in Section 4.4.1. I present the following work with the final three discussing interfacing temporal modes with the Raman memory and demonstrate 4 key results:

1. **Overlap of carved modes:** Here I experimentally combine the work of the previous two sections by measuring the orthogonality of carved Hermite-Gaussian modes using the setup described in Figure 5.2. I then discuss how it may be used as a tool to evaluate the Raman memories temporal mode manipulation.

2. **Maximising the efficiency of the Raman memory:** This is achieved by pulse carving the signal to compensate for the AC-Stark shift. A time-varying phase applied across the signal ensures the signal and control remain in two-photon resonance throughout the interaction, thus maximising the efficiency. I theoretically calculate the optimised mode and evaluate the changes to efficiency.

3. **Mode selectivity:** The Raman memory is inherently single-moded, only one particular temporal mode, defined by the control field, will be stored in the memory and all orthogonal modes will be transmitted. I experimentally demonstrate the attempted storage of sub-optimal modes and discuss the power dependency of this behaviour.

4. **Mode manipulation:** A result of the excitation being stored within a single-mode is

that the retrieval control field pulse is decoupled from the read-in pulse. This means that shaping the read-out pulse can alter the temporal mode compared to the read-in without any adverse affects. The memory therefore acts as a quantum gate within this high-dimensional Hilbert space.

5.3.1 Overlap of carved modes

Figure 5.4 shows the coincidence trace and results of interfering pulses of weak coherent states with a FWHM 10ns and average photon number $\langle n \rangle = 1.1$. The M value for each coincidence trace is shown and varies from 0.506 ± 0.005 in the maximally interfering case to 0.736 ± 0.006 in the orthogonal cases. Equation 5.6 relates V and M, and we can use it to calculate the corresponding overlaps, which in the maximal case are 97.1(1)% to 1.49(3)% respectively. Table 5.2 below shows the interfered modes, their measured M value, and corresponding overlap.

Table 5.2: Results showing the interference from twocarved Hermite-Gaussian modes sent through the unbalanced mach-Zender shown in Figure 5.2.

HG modes and polarisations	M Value	V Overlap
$(0, H)$ and $(0, V)$	0.726	5.65%
$(0, V)$ and $(0, V)$	0.506	97.1%
$(1, V)$ and $(0, V)$	0.736	1.49%
$(1, H)$ and $(1, V)$	0.732	3.15%
$(1, V)$ and $(1, V)$	0.525	89.3%

This proof of principle experiment shows how we can observe HOM interference with weak coherent states to characterise temporal modes. It could further be used to perform a tomography on an unknown temporal mode state through repeated measurements. The imperfect measurement of overlap/orthogonality between both orthogonal polarisations and

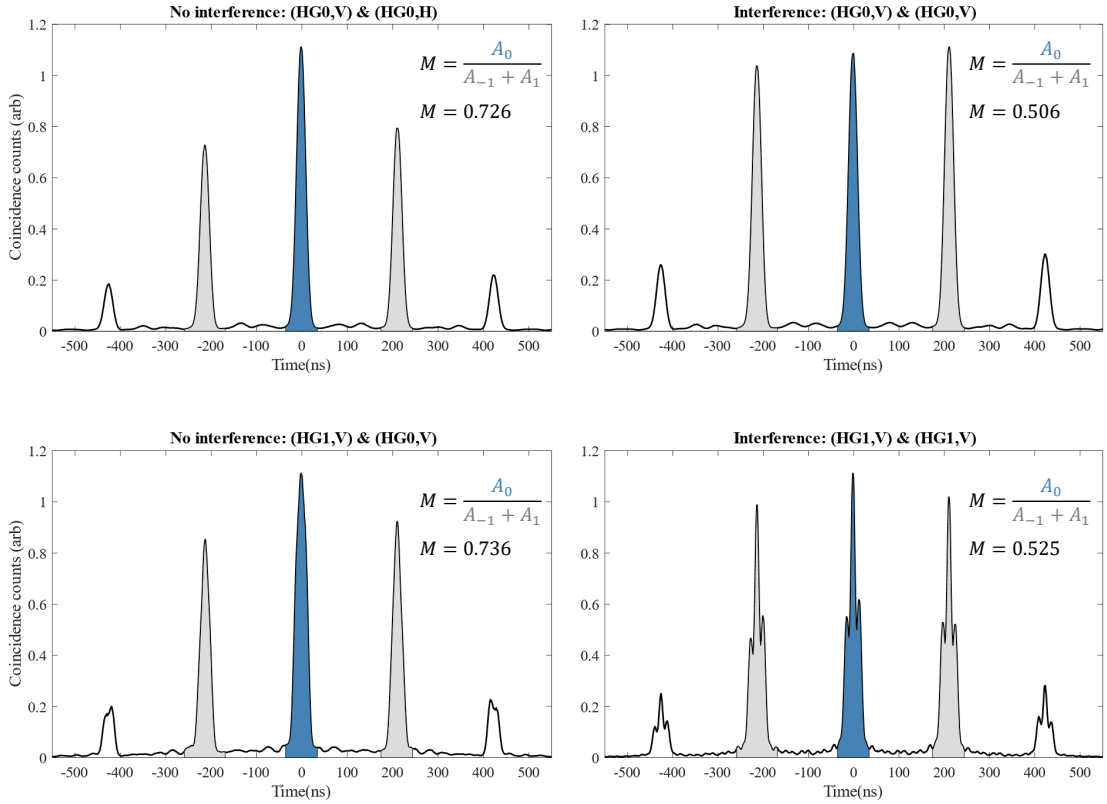

Figure 5.4: Coincidence traces for 4 configurations of input temporal modes. All temporal modes are 10ns FWHM, and separated by 200ns. Top left: Pulse 1 and 2 are both $HG0$ but have orthogonal polarisation. Top right: Pulse 1 and 2 are both $HG0$ and have the same polarisation. Bottom left: Pulse 1 is $HG1$ and pulse 2 is $HG0$ and have the same polarisation. Bottom right: Pulse 1 and 2 are both $HG1$ and have orthogonal polarisation.

orthogonal temporal modes is limited by the stability of the interferometer whilst the uncertainty can be improved by measuring for a longer time. There is a trade-off between the size of the coherent state used and the waiting time required to gain precise values.

5.3.2 Maximising the efficiency of the Raman memory:

We recall in Sections 2.5.1 and 2.5.2 that for a given control field and power, we can calculate the optimum signal mode by performing a single value decomposition. As described in

Section 2.5.1 we construct the Green's function G_{ss} as:

$$G_{ss} = \sum_{i=0} \hat{M} \left|\sigma_i\right\rangle \left\langle\sigma_i\right| \tag{5.8}$$

where the $\hat{M}$ operator represents the memory interaction for a given control field and power, and σ_i represents the i^{th} Hermite-Gauss mode. The SVD of G_{ss} recasts the Green's function to the form:

$$G_{ss} = \sum_{i=0} \lambda_i \left|u_i\right\rangle \left\langle u_i\right| \tag{5.9}$$

where λ_i are the singular values corresponding to this new (but equally complete) $|u_i\rangle$ basis. Since the output of the memory $|\psi_i\rangle = G_{ss}\,|u_i\rangle = \lambda_i\,|u_i\rangle$, the efficiencies are given by $\eta_i = \langle\psi_i|\psi_i\rangle = \lambda_i^2$. From the SVD we can define the Schmidt number[161] which represents the mode capacity of the Green's function and memory. This is a measure of how single-moded the memory is and is given by:

$$K = \frac{1}{\Sigma_i (\eta_i')^2}, \quad \text{where} \quad \eta_i' = \frac{\eta_i}{\Sigma_i \eta_i}. \tag{5.10}$$

The input signal $|u_i\rangle$ with the largest value of λ_i corresponds to the optimum mode that can be stored in the memory. For low-powered control fields, the optimum mode is closely matched to the control field, however at high-power the AC-Stark effect perturbs the Raman 2-photon condition between signal and control. In practice, a time varying phase in the signal field can maintain the condition, increasing the efficiency. Figure 5.5 shows how the memory efficiency can be optimised by increasing the power and using the optimum mode for the control field power. One might expect the optimised case to be monotonically

increasing with control field power. The slight decreases observed in Figure 5.5 (such as at 200pJ and 3600pJ) are likely due to simulation artefacts whereby the required number of HG basis states were used to generate the optimum mode. The number of basis states required increases with power, and for each power, an additional mode is considered to see if the efficiency changes greater than a threshold $\epsilon \ll 1$. Constraining ϵ to a smaller value would likely yield the monotonically increasing behaviour expected. Future experiments will combine this high efficiency with the *magic* suppression scheme of Chapter 4 to produce a high efficiency, noise free memory.

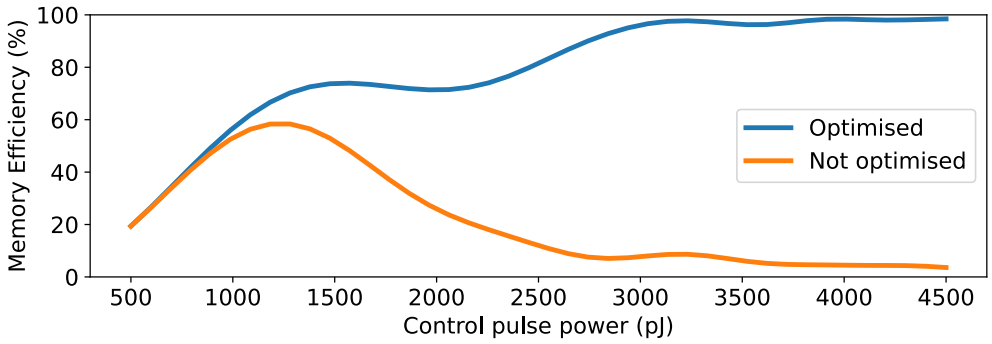

Figure 5.5: Memory efficiency for a HG0 control field with varying power. In the blue, optimised case, the signal is derived from the principle mode of the SVD of the Green's function whilst and in the orange case a HG0 signal pulse is used. The same, HG0 pulse is used for the control in both cases.

5.3.3 Mode selectivity

The Schmidt number K assigned to a memory implementation describes the number of modes that can be stored within the memory, using the specified control field. A useful illustration would be if there were three orthogonal modes $|u_{1-3}\rangle$ that all had the same efficiency, and the efficiency of all other modes is zero. In this case K equals 3 by definition from Equation 5.10 and does equal the number of modes stored with the same efficiency.

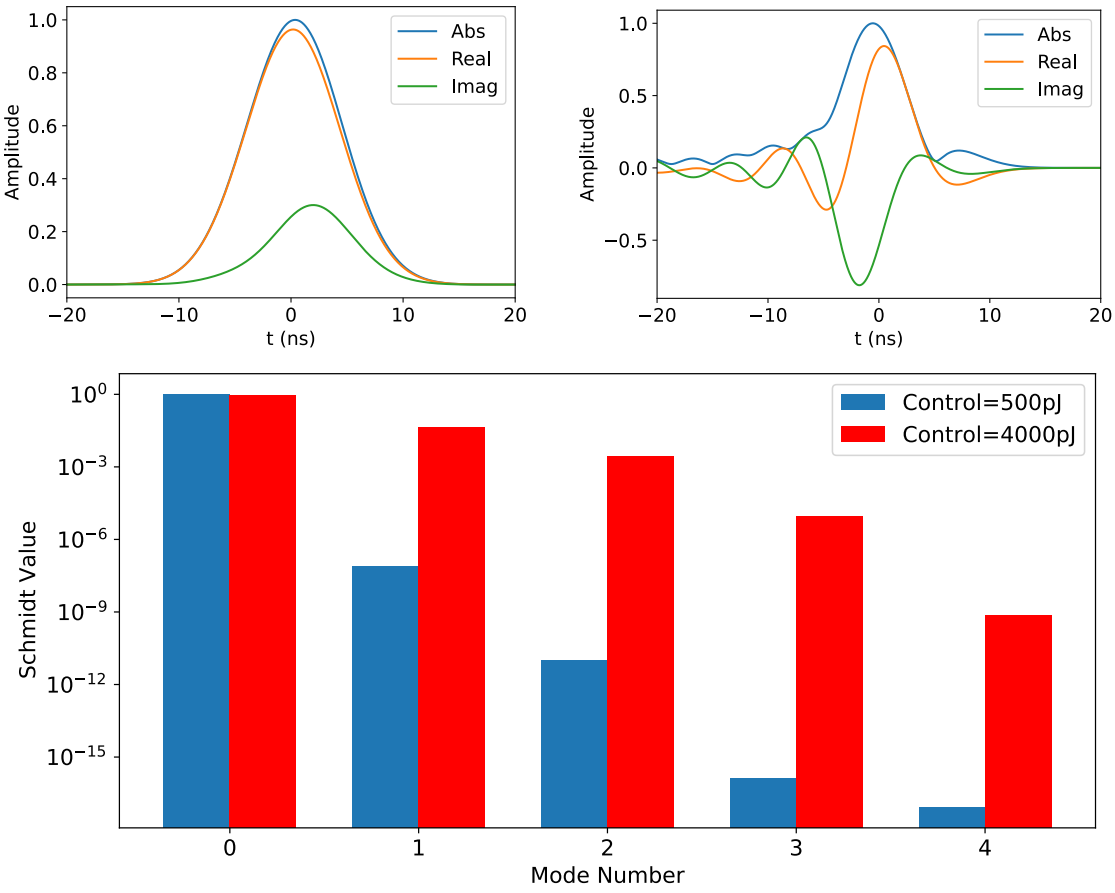

Figure 5.6: Top: The absolute (blue), real (orange) and imaginary (green) amplitudes of the signal corresponding to the principle mode of the SVD of the memory process given a control pulse power of 500pJ (left) and 4000pJ (right). The same, HG0 mode, is used for the control in both cases. Bottom: Increase in multi-modality of the memory at the two powers with the bars from each case summing to 1. The principle Schmidt value in each case is $(1 - 2.3 \times 10^{-8})$ at 500pJ and 0.976 at 4000pJ.

In general, for the Raman protocol, $K = 1$ i.e. there is just one input mode $|u_0\rangle$ that has non-zero memory efficiency. This single-mode property lends itself to two applications:

1. **Photon source purification:** Many photon sources emit into many modes; PDC for example has the photon projected into a mixed state following the measurement of the herald. Specific mode-engineering of a source is possible [162] for a given, desired application (for example to operate at a specific wavelength), but this is not a general

solution. Spectral filtering enables the generation of approximately pure photons, but significantly reduces the source's brightness[163].

A solution has been proposed in the form of a single-mode TM device[164], and more recently the ORCA memory protocol has been shown to be able to optimally filter InGaAs quantum dot emission[74]. This approach to enhance photon purity could be improved by implementing with the Raman protocol given the flexibility that a longer storage time offers, and the Raman protocol is, in general, more single moded. There is however, a trade off shown in Figure 5.6 which shows the modal distribution at both low and high power within the Raman memory. The low-power case is entirely single mode with a principle Schmidt value of $K = 1 + 1.64 \times 10^{-7}$ whereas the high-power case has near unit efficiency but at the cost of $K = 1.1$.

2. **Encoding conversion:** When operating in the single-mode regime, the Raman memory protocol provides a natural interface between temporal mode (orthogonal basis states given by $|u_i\rangle$) and time-bin qubits (orthogonal states given by $|v_a\rangle$). One could imagine the idealised case where a superposition of $\frac{1}{\sqrt{2}}(|u_{0,a}\rangle + |u_{1,a}\rangle)$ incident on the memory in a single-mode configuration where $\eta_i = \eta\delta_{0,i}$ and $\eta_{\text{read}-\text{in}} = 1$. The part of the quantum state corresponding to $|u_0\rangle$ is stored, delayed and may be retrieved at will, placed into any desired time-bin $|v_b\rangle$ leading to the conversion:

$$\frac{1}{\sqrt{2}}(|u_{0,a}\rangle + |u_{1,a}\rangle) \rightarrow \frac{1}{\sqrt{1+\eta^2}}(|v_a\rangle + \eta\,|v_b\rangle), \tag{5.11}$$

thus converting a superposition in spectral-temporal modes to a time-bin superposition. There is a useful parallel to be drawn from the noise analysis of anti-Stokes

noise; when the memory is not single-moded, part of the sub-optimal mode(s) will be stored. This will then be converted to the read-out mode and thereafter indistinguishable from the desired stored mode. This is analogous to FWM having produced extraneous photons in the signal mode which cannot be removed. Whilst FWM noise was only apparent when examining the $g^{(2)}$, this multi-moded "noise" would reduce the photons purity and hence become apparent in a HOM measurement. The retrieved photon purity would be equal to the reduced Schmidt number[3].

Control \ Signal	HG0	HG1	HG2
HG0	39.4%	0.074%	2.5%
HG1	0.11%	41.1%	1.8%
HG2	1.8%	2.2%	44.2%

Table 5.3: Table showing the experimental read-in efficiencies corresponding to the first three Hermite-Gauss modes applied as signal and control fields to the Raman memory. The effiencies correspond to the timetraces in Figure 5.7.

Figure 5.7 and Table 5.3 show the mode selective property of the Raman memory when operated at 500pJ control field pulse energy. When the signal and control have orthogonal temporal modes the read-in efficiency is almost zero and the signal transmits straight through the memory, as shown in the off-diagonal plots. In the case, however, where the control and signal modes are the same and well-overlapped, there is significant memory read-in. Future experiments will improve the read-in efficiency by using the optimal modes, as shown in the previous section, however we haven't reached that capability yet. Using the orthogonal basis provided by the SVD will have the added advantage of lowering the read-in efficiency for orthogonal modes.

[3]Where the reduced Schmidt number is when only the relevant modes are considered. For example in Equation 5.11 only TMs 0 and 1 are considered, hence only modes 0 and 1 would appear in the reduced Schmidt definition in Equation 5.10, even if $\lambda_2 \neq 0$.

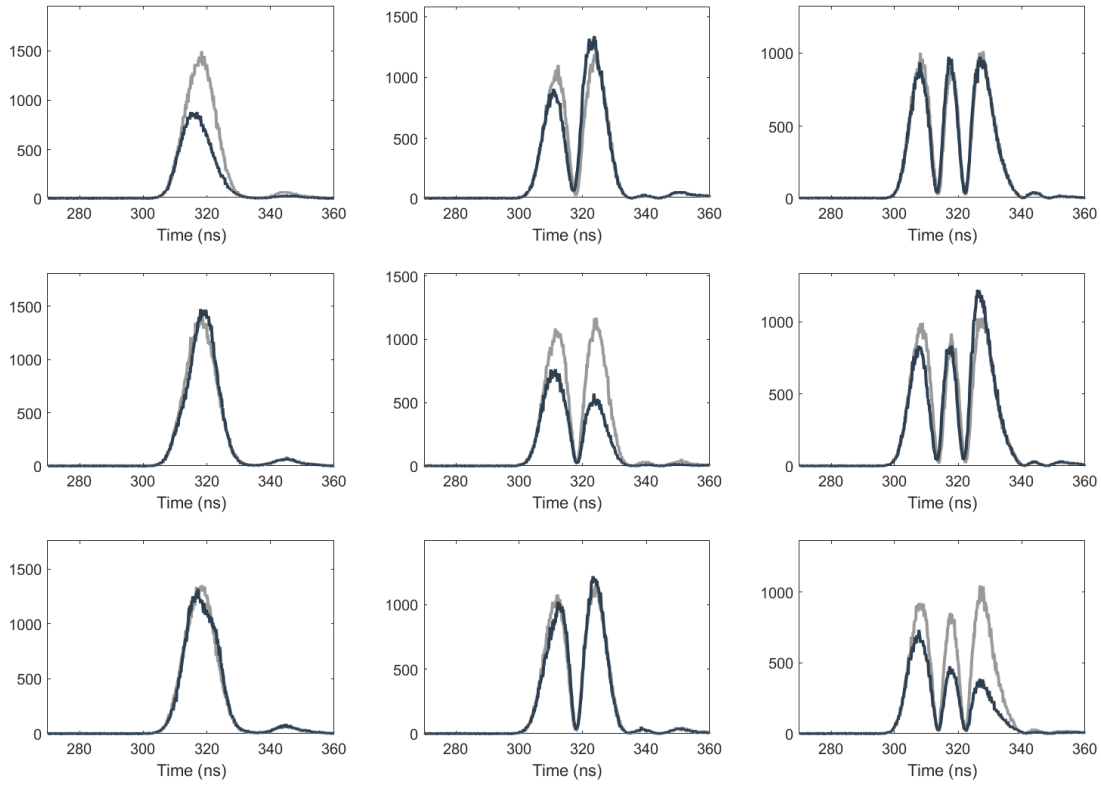

Figure 5.7: 3x3 grid showing the attempted read-in the first three HG modes being used as signal and control fields. Each column refers to one the first three HG modes being used as the input signal, whilst the row corresponds to different HG modes in the control. The diagonal elements therefore use the same HG mode for signal and control whilst the off-diagonals use orthogonal HG modes. The grey line refers to the input signal, whilst the black to the transmitted – following attempted read-in. The corresponding read-in efficiencies are given in Table 5.3.

5.3.4 Mode manipulation

The final application I shall consider is mode-conversion, both within the temporal mode Hilbert space but also to interface between devices. The simplest illustration of this would be pulse length/bandwidth manipulation – turning a short (spectrally broad) pulse into a long (spectrally narrow) pulse and vice-versa. The former transformation may be performed with a passive bandpass filter, whilst the latter could be achieved with, for example, the MZI-EOM or a Pockell's cell, but at a significant efficiency cost depending on device transmission and rise/fall times. Figure 5.8 shows both bandwidth compression and expansion, and

compares experimental results to that of a passive filter. Although the efficiencies are relatively modest, these proof of principle experiments demonstrate the capacity for the Raman memory to be utilised in this way, and indeed for a large compression factor, the memory outperforms a bandpass filter.

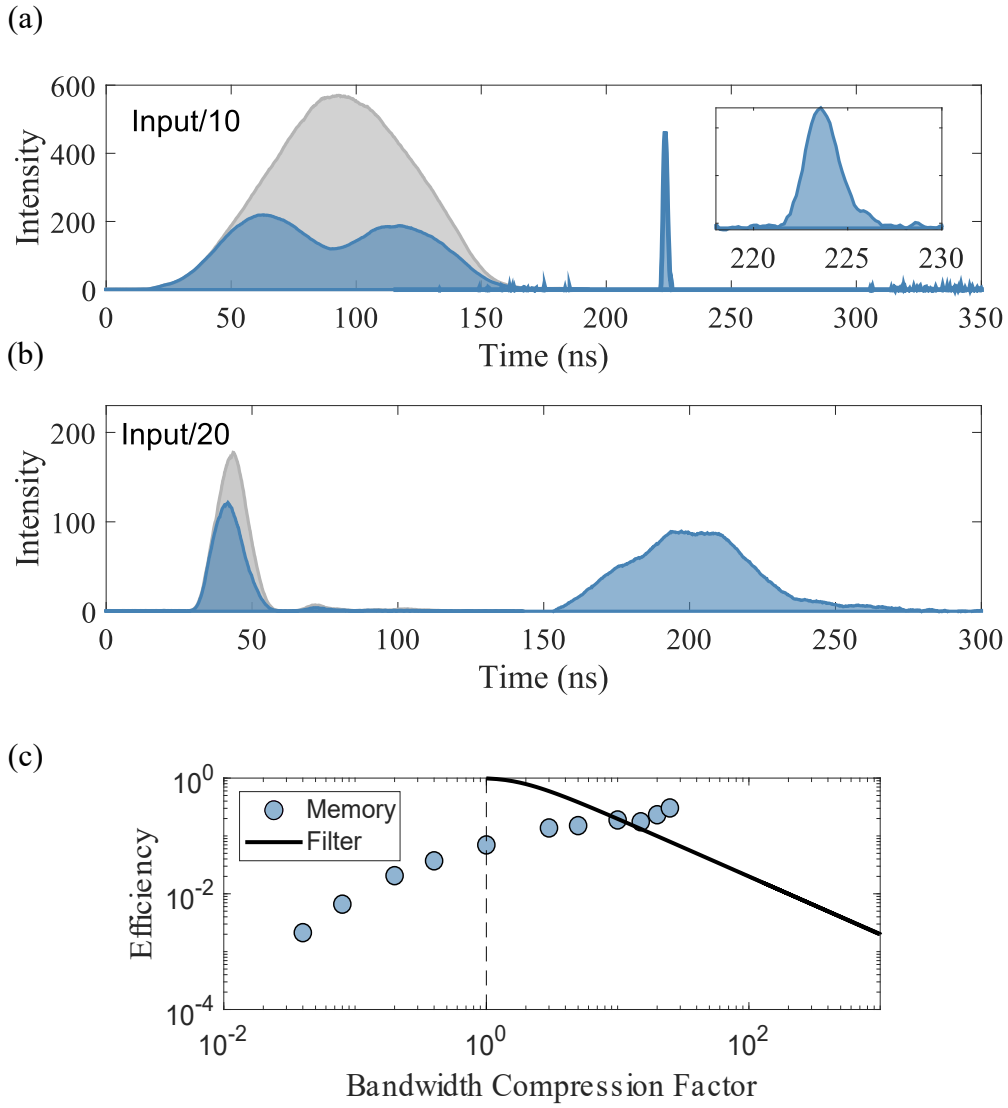

Figure 5.8: a) Bandwidth conversion showing conversion of a 50 ns (FWHM) pulse to a 1 ns pulse. b) A 10 ns pulse is converted to a 100 ns pulse c) Efficiencies of bandwidth compression performed with the Raman memory with the solid line representing a top-hat bandpass filter.

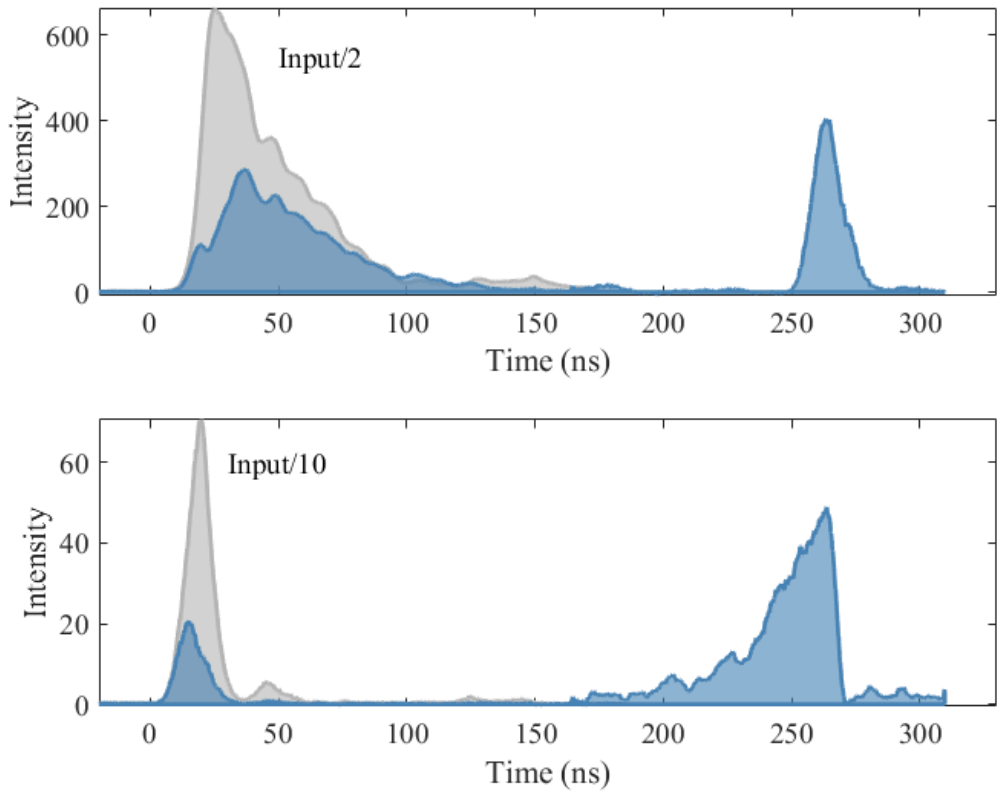

Figure 5.9: a) Storage of a falling exponential profile retrieved as a HG0 temporal mode with read-in efficiency of 48% and total memory efficiency $\eta = 12.2\%$. b) Storage of a HG0 Gaussian pulse retrieved as a rising exponential temporal profile with read-in efficiency of 69.4% and total efficiency $\eta = 13.1\%$.

Another intuitive example would be attempting storage from a photon-source, the temporal profile of which is a falling exponential (such as spontaneous decay from a two level atomic system). The read-in control field could be shaped for optimal storage of the exponential, whilst the retrieved pulse could be in a Hermite-Gauss mode [165], allowing for better performance when interfaced in a quantum network. Figure 5.9 shows conversion between a falling exponential to a HG0 Gaussian pulse, and also the reverse process.

Finally, we consider manipulation with the Hilbert space defined by Hermite-Gaussian temporal modes. Figure 5.10 shows conversion from the first two HG modes to the first

three. When the Raman protocol is performed in the single-mode regime, the efficiency is independent of the input mode, which is demonstrated here for all conversions. The conversions shown here describe quantum gate operations within this high-dimensional QIP basis.

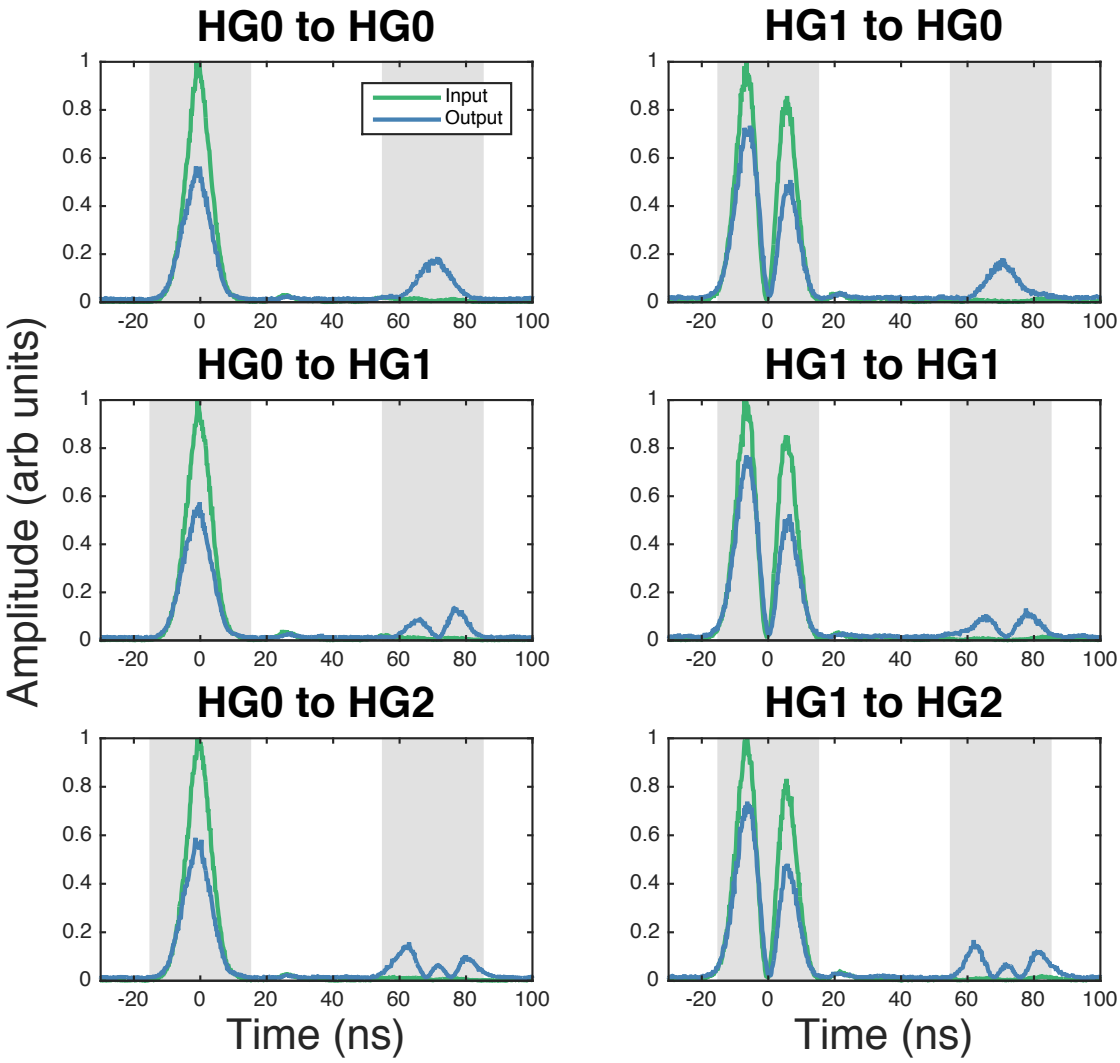

Figure 5.10: Storage of the zeroth and first Hermite-Gauss modes (left and right column respectively) which are subsequently retrieved as each of the first three HG modes. The control pulse energy is kept constant between modes and memory efficiency also remains constant at approximately $\approx 15\%$.

Unfortunately, we only have intensity measurements for the data presented here, and as such cannot check the modal overlap between the input and retrieved mode. Future experiments will integrate the method described in Section 5.2.1 with the output of the memory, allowing measurement of the overlap between the input and retrieved modes. There is an experimentally simple way to realise this; if we recall the pulse sequence used, we note that after the retrieved pulse is a copy of the control field used for read-in, but in the signal mode. Engineering the gap between this pulse and the retrieved state to equal Δt of the unbalanced interferometer in Figure 5.2 provides a natural solution to measure the overlap between these states. Such measurements allow us to assign a fidelity on this mode-conversion operation.

To understand the Raman interaction, we can perform process tomography on the system. This would involve probing the memory with a set of input states that span the complete state of the memory. An obvious choice for such inputs would be a set of mutually unbiased bases (MUBs), each of which have constant overlap with each of the basis vectors. In the qubit system of HV polarisation, these correspond to inputs of diagonal/anti-diagonal and left/right circularly polarised light. These can be constructed for higher dimensions, yielding an overlap of $1/d$ where d is the number of dimensions[166]. Probing the memory in 2D temporal mode space would involve sending input signals of (HG0 $\pm$ HG1) and (HG0 $\pm\, i$HG1), and recording the read-in efficiencies. Unfortunately some of MUBs for the temporal modes have very sharp (instantaneous) phase changes over the pulse, making them experimentally difficult to carve with the EOM-MZI. This could be mitigated by using the method described in Section 5.2.1 to characterise the accuracy of the carved MUBs and performing additional measurements as required.

5.4 Conclusion

In this chapter I have demonstrated the versatility of the Raman memory when operating with temporal modes of light and how temporal modes may be used to enhance the memory's capabilities. The key achievements demonstrated in this chapter are as follows:

- After introducing temporal modes as a desirable basis for quantum information, Section 5.2.1 showed the creation of a proof of principle experiment to measure the overlap between weak coherent, temporal modes of light. This was tested and shown to not only measure polarisation orthogonality, but was additionally used to confirm that the pulse carving system was producing orthogonal temporal modes.

- Section 5.3 showed the results of four experiments, including the testing of the orthogonality measurement. The other three experiments related directly to the Raman memory, began by optimising the memory efficiency by using the principle mode of the single-value decomposition of the Green's function that describes the interaction. This demonstrated potential to significantly enhance the memory efficiency by counteracting the effects of the AC-Stark shift.

- The final two experiments showed temporal mode-selectivity and manipulation, demonstrating the ability for the Raman memory to act as a key device within a quantum network based on this high-dimensional encoding that makes optimum use of the time-frequency degrees of freedom. It also showed how pulse-carving could be used to optimise the interface between different systems, be that between their temporal emission profile or their bandwidth.

In conclusion combining the applications demonstrated in this chapter with the low-noise capabilities proven in Chapter 4 perfectly places the Raman memory as a device to interface with this exciting basis for quantum information at the single-photon level.

Chapter 6

Warm Vapour AFC

> "An experiment is a question science poses to Nature, and a measurement is Nature's answer."
>
> Max Planck

This chapter details the work undertaken with P.M.L and D.J.M which, tangential to the work on the Raman memory protocol, investigates a velocity selective pumping strategy for suppressing motion induced dephasing in warm vapour quantum memories. What began as a demonstration of the ability to selectively pump a single velocity class developed into the world's first demonstration of an atomic frequency comb memory implemented in warm vapour. The following sections are based on the publications [167] and [168]. The velocity selective pumping idea was conceived by D.J.S and an early experimental design constructed by S.G. The experimental implementation and and theoretical analysis were conducted by D.J.M (under my instruction) and myself. The repurposing of the detection scheme and the measurement of the combs and associated echoes was completed by P.M.L. P.M.L was also responsible for overseeing and supervising the work.

6.1 Velocity selective pumping

Gao *et al.*[74] recently posited the ORCA memory's single-moded nature for use as a quantum buffer. A single-mode memory (like ORCA or the Raman memory) can optimally filter out temporal spectral noise from many imperfect photon sources to produce identical photons. As discussed in Section 1.3.3, the ORCA memory suffers from a comparatively short lifetime when implemented in a warm vapour. This is due to the thermal motion of the atoms and the comparably short length of the spatial hologram of the spin wave. However, if the protocol is implemented with only the atoms belonging to a single longitudinal velocity class (e.g. those atoms with $v_z = 0$), the lifetime could be significantly extended.

6.1.1 Introduction

In Chapter 2 we introduced the delocalised excitation in the form of the Dicke-like state given by Equation 2.48. Up until now, we have not considered the motion of the atoms[1] despite the excitation taking the form of a spatial hologram across the atomic ensemble. We can incorporate the motion of the atoms into this spin-wave description by writing the state of the collective excitation in the time-dependent form

$$|\psi(t)\rangle = \sum_{i}^{N} \frac{1}{\sqrt{N}} e^{i\boldsymbol{\delta k}_r \cdot \boldsymbol{r}_j(t)} |0_1 \cdots 1_i \cdots 0_N\rangle \tag{6.1}$$

where $\boldsymbol{r}_i(t)$ is the position of the i^{th} atom at time t, and $\boldsymbol{\delta k}_r = \boldsymbol{k}_s - \boldsymbol{k}_c$ is the wavevector associated with the created spin-wave, given by the difference in wavevectors between the signal and control fields. Having the spin-wave excitation created at time $t = 0$ and retrieved at time $t = t_1$ we can consider how the excitation decoheres given the atoms move according

[1] The reason for this will become clear when we apply the lifetime calculation to the Raman memory.

to $\boldsymbol{r}_i(t) = \boldsymbol{r}_i(0)+\boldsymbol{v}_i t$. Given the beam propagation in the z direction we can restrict ourselves to considering only longditudinal velocities in the z direction; yielding the overlap of inital and final spin-waves to be:

$$\langle\psi\,(0)|\psi\,(t_1)\rangle = \frac{1}{N}\sum_{j=1}^{N} e^{i\boldsymbol{\delta k}_r\cdot\boldsymbol{v}_j t_1} \rightarrow \int f\,(v_z)\, e^{i\delta k_r v_z t_1}\mathrm{d}v_z, \tag{6.2}$$

where $f(v_z)$ is the velocity distribution of the ensemble (of atoms partaking in the memory protocol). We recognise Equation 6.2 as the Fourier transform of the velocity distribution, meaning that the the width of the velocity distribution δv and the phase mismatch $\delta k_r t_1$ are complementary variables. We can use this Fourier relationship to estimate a timescale for the motion induced dephasing:

$$\tau_D = \frac{1}{(\delta k_r)(\delta v)} \tag{6.3}$$

In atomic vapours, the velocities will be distributed according to a Maxwell–Boltzmann distribution, leading to Doppler broadening of the optical transition to a linewidth of $\sim$ 1 GHz at room temperature [169], far exceeding that of the natural linewidth of the transitions ($\sim$ 5.2 MHz).

When using the Raman quantum memory on a three-level system in a Λ configuration in a warm vapour [170], δk_r is small leading to a motion-induced dephasing timescale of $\sim 20\,\mu$s in caesium[2]). In the ladder configuration used in ORCA, δk_r is much larger. This leads to a 5.4 ns storage time for the $6S_{1/2}$-$6P_{3/2}$-$6D_{5/2}$ ladder in caesium [171] and a 100 ns storage time for the $5S_{1/2}$-$5P_{3/2}$-$5D_{5/2}$ ladder in rubidium [172].

[2]We see now this isn't the dominant decoherence mechanism and as such are safe to have neglected it earlier.

Clearly, to extend the dephasing time in ORCA we can either reduce (δk_r) or (δv). Reducing (δk_r) to zero would involve operating at degeneracy with the signal and control having the same frequency. This is generally incompatible with the protocol as the control would introduce unwanted excitations in addition to the desired storage excitation. Normally reducing the width of the velocity distribution requires atomic trapping techniques, greatly increasing experimental complexity. Finkelstein *et al.* [173] recently removed the Doppler dephasing in the FLAME protocol by continually dressing the storage state with an auxiliary sensor state to generate a velocity insensitive collective state. This does require additional, high-power lasers applied continuously throughout the protocol, again significantly increasing experimental complexity.

Our approach to combat Doppler dephasing is via *velocity selective optical pumping*. Using standard optical pumping techniques, we pump all the atoms out of the ground state into an auxiliary state not participating in the quantum memory; we then use a narrowband laser to pump back a single velocity class into the ground state used by the quantum memory. In theory this would reduce δv to zero but in practice the width of the velocity class is limited by the natural linewidth of the pump laser.

6.1.2 Experiment

To perform and characterise the success of our velocity selective pumping technique, we use a three stage process, shown in Figure 6.2, and performed with the experimental set-up laid out in Figure 6.1.

1. **Preparation:** In this stage, we empty the ground state by optically pumping all atoms to an auxiliary state. We begin with a paraffin-coated caesium cell of length

25 mm and diameter 10 mm at room temperature. The paraffin coating maintains the spin-polarisation of the ensemble when the atoms collide with the cell wall ($\sim$ 1000 collisions). However, upon collision, the the atom will change to another velocity class. This is crucial as it allows for the entire ensemble to be pumped using only a narrowband laser[174,175], if applied for long enough and at a high power to enable power-broadening of the transition. Hence, the preparation stage consists of applying a 20 mW CW laser (852 nm Sacher Lasertechnik ECDL) to the $F = 4 \rightarrow F' = 4'$ $D2$ transition to empty the $F = 4$ ground state into the $F = 3$. By using acousto-optic modulators (AOM) to time-gate the fields, we pump for approximately 1 ms, at which point the entire ensemble is efficiently prepared in the $|F = 3\rangle$ state.

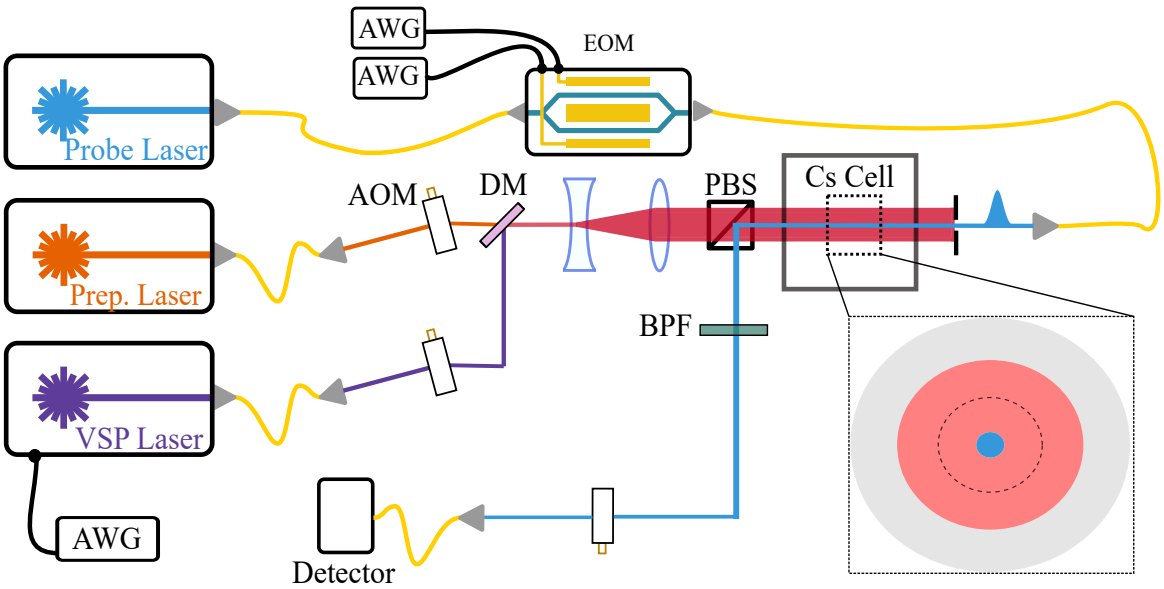

Figure 6.1: Experimental setup to perform and characterise velocity selective pumping. The preparation and velocity selective pumping lasers are time-gated with acousto-optic modulators (AOM) and combined with a dichroic mirror (DM). The probe uses the same EOM from Section 4.4 and a narrow bandpass filter (BF) is used to prevent contamination at the detector. Arbitrary waveform generators (AWG) are used to carve the probe signal and modulate the VSP laser during the AFC experiment. Insert:Cross-section of the caesium showing the pumping and probe modes. The beam waist of the VSP pump and probe modes are 4 mm and 0.3 mm respectively. The dotted line marks a 3σ length-scale that corresponds to the distance from the probe mode an atom would travel in 2μs while moving with a radial velocity of three standard deviations of the velocity distribution ($3v_{th}$).

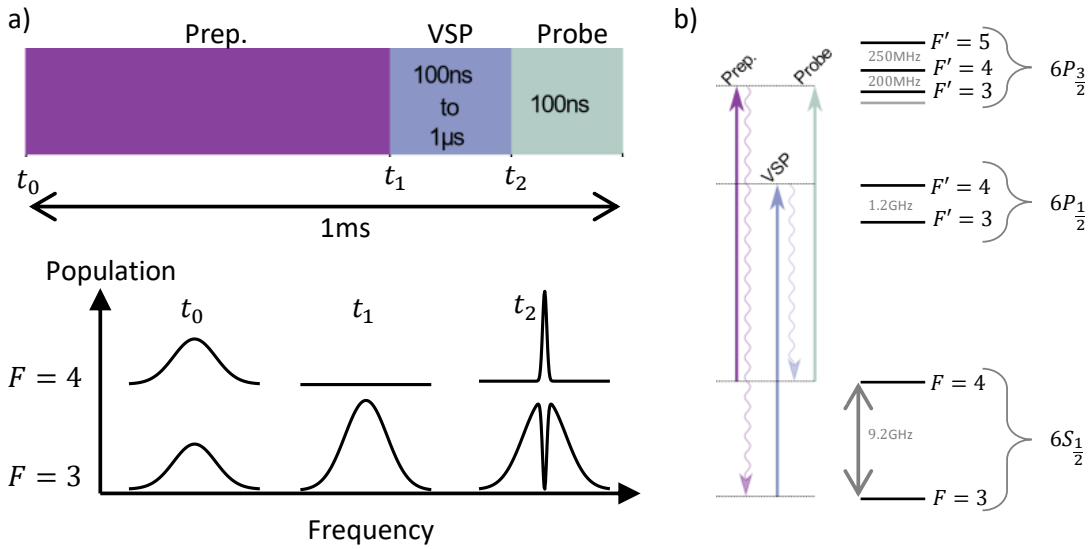

Figure 6.2: Velocity-selective pumping principle. a) Timescales associated with the pump sequence as well as a qualitative indication of the ground state population velocity distribution. b) Caesium hyperfine levels for the $6S_{1/2}$ ground and $6P_{1/2}$, $6P_{3/2}$ excited states together with the corresponding pump modes. The 'Prep.' mode initialises the $F = 4$ ground state via the $6P_{3/2}$ excited state. The 'VSP' (velocity-selective pump) mode prepares the velocity selected population via the $6P_{1/2}$ excited state. Finally, the 'Probe' mode probes the spectral response of the prepared feature via the $6P_{3/2}$ excited state.

2. **Velocity selective pumping:** We then apply a second, narrowband ($\sim$ MHz) laser (Toptica DFB) for time τ_p resonant to the $D1$ $F = 3 \rightarrow F' = 4'$ 852 nm transition, pumping-back a single velocity class to the $|F = 4\rangle$ state. This transition is chosen due to the excited state hyperfine splitting being larger than the Doppler broadening (in contrast to the D2) – ensuring that a single velocity class from a single transition is addressed. This results in the $F = 4$ ground state now being populated with just a single velocity class. We varied both the power and time τ_p of this stage to characterise the effects on the resulting velocity distribution.

3. **Probe:** A narrowband, CW scanning laser (Toptica DL Pro) was used to perform absorption spectroscopy on the $F = 4 \rightarrow F' = 3, 4, 5$ transitions in the D_2 line. By keeping the waist much less than that of the preparation and selective pumping beams

means a true reflection of the pumping can be obtained. Furthermore, the power is kept well below the saturation intensity, and the probe is time gated in the VSP measurements to ensure it doesn't perform any additional pumping[3].

This three step process allows us to determine the effect of varying the power and pulse duration of the velocity selective pumping stage. Based on my simulations for the Raman memory, D.J.M was able to simulate the rate equations and numerically simulate the process. Using a numerical fitting scheme, it was possible to extract a velocity distribution from the measured absorption spectra, thus allowing estimation of the motion-induced dephasing timescale – the details of these simulations are given in [167]. The measured spectra and the fitted simulated spectra for a range of selective pumping times and powers are shown in Figure 6.3. They show very good qualitative agreement between the model and the experimental data. As the power is increased, power broadening occurs, saturating the central velocity class and transfers more atoms from a broader range of velocity classes into the $F = 4$ state. This effect is exacerbated at longer pump times and powers to a point at which atoms from nearly every velocity class are addressed to some degree (indeed this makes sense; if it occurred for too long, and/or at too high a power, the process becomes analogous to the preparation stage).

Atomic drift

At some time after velocity selective pumping, atoms exit the pumped region (cross section of the Cs cell shown in Figure 6.1), collide with the cell wall (retaining their spin-polarisation due to the paraffin coating) and re-enter the probe region in a different velocity class. This

[3]The probe was not time-gated from the atoms in the AFC measurements, but there was no discernible difference to the produced spectra with and without the gating.

happens on a timescale quicker than we can scan the probe across the $F' = 3, 4, 5$ levels. To avoid the erroneous results that attempting to probe the entire spectrum would yield, we instead repeat the pulse sequence given in Figure 6.2 many times, each time probing a different region of the spectrum which we can then piece together to give a complete spectrum.

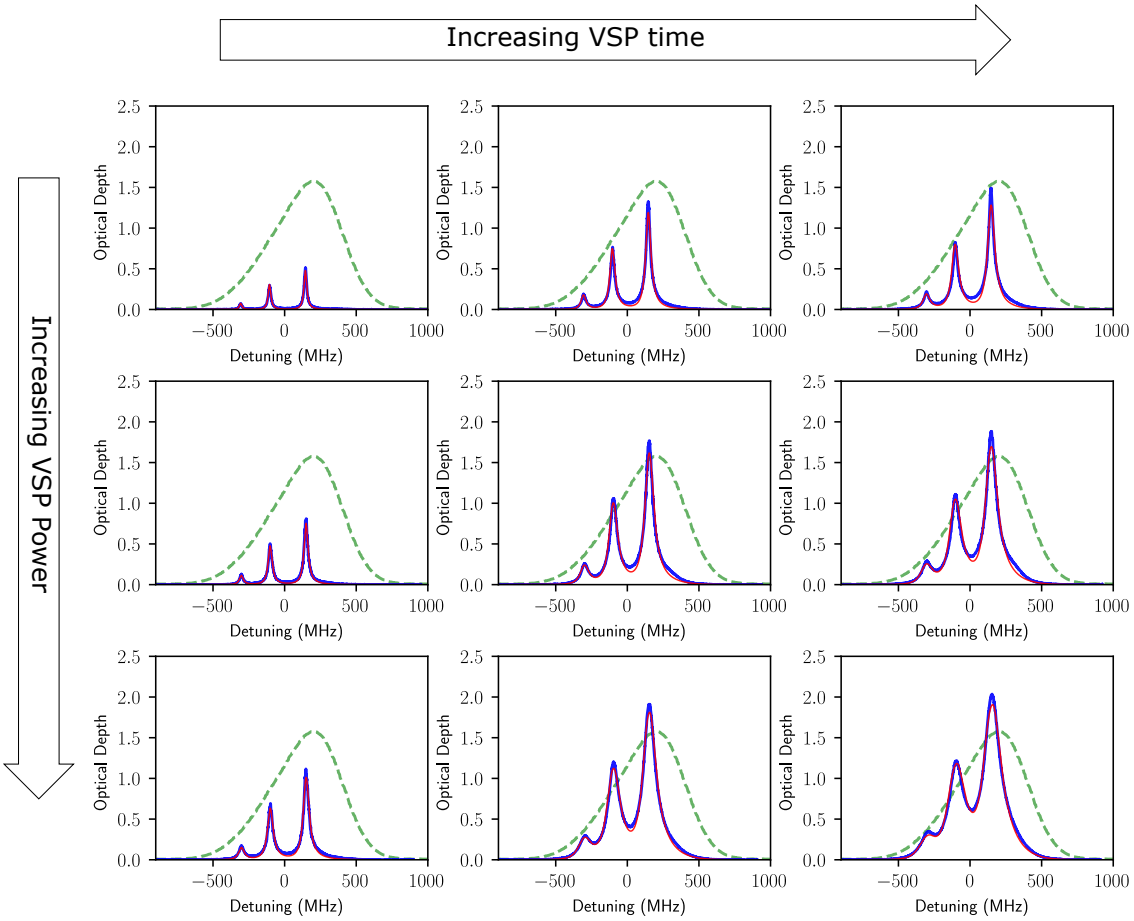

Figure 6.3: Velocity-selective pumping spectra. The blue lines are the optical depths of the D_2 $F = 4 \rightarrow F' = 3, 4, 5$ transitions as a function of frequency for various VSP pump times and powers at 23 °C. The horizontal axis is the detuning from the transition between the $F = 4$ hyperfine level in the $6^2S_{1/2}$ manifold and the $6^2P_{3/2}$ manifold. From top to bottom, the VSP powers are: 0.86 mW, 4.1 mW, and 10.5 mW. From left to right, the VSP times are: 0.2 µs, 1.2 µs, and 2 µs. The red lines are the simulated spectra. The green line is the unpumped, Doppler broadened spectrum.

6.1.3 Results

Obviously there is a significant trade-off between the number of atoms pumped back to the ground state used by the memory and the width of the velocity distribution of these atoms. For the ORCA protocol this manifests in the optical depth (coupling strength) vs Doppler dephasing time. Figure 6.4 shows how these two parameters respond as the power and duration of the selective pumping stage are varied. The Doppler dephasing time is extracted by fitting the spectrum measured by the probe to a velocity distribution $f(v_z)$ which was derived from numerical simulation of the rate equations.

Whilst having not integrated the VSP technique into the ORCA protocol, we have demonstrated strong agreement with simulation and can therefore be confident of our predictions regarding the extension of the ORCA memory's lifetime. Utilising a ladder scheme, the level structure of both caesium and rubidium allows storage of photons in the telecom frequency band. These could be, (for example) the $5S_{1/2}$-$5P_{3/2}$-$7S_{1/2}$ ladder in Cs with an upper transition at 1470 nm and a 1528 nm transition using the $5S_{1/2}$-$5P_{3/2}$-$5D_{5/2}$ pathway in Rb. Without suppressing the Doppler dephasing, the wave-vector mismatch gives a debilitatingly short lifetime for these ladders, however were they to be performed by a single velocity class, the dephasing time could increase significantly. The potential to interface the memory with telecom photons is an exciting prospect given the infrastructure that already exists in telecom photonics and the ability to create large scale quantum networks.

Table 6.1 shows the enhancement factor β that can be made to the Doppler lifetime in the aforementioned cases. The VSP power and time were taken to be 1 mW and 0.1 µs respectively. We modelled selecting the zero-velocity class and took the linewidth of the velocity selective laser to be 6 MHz. After mitigating the Doppler dephasing, there are of

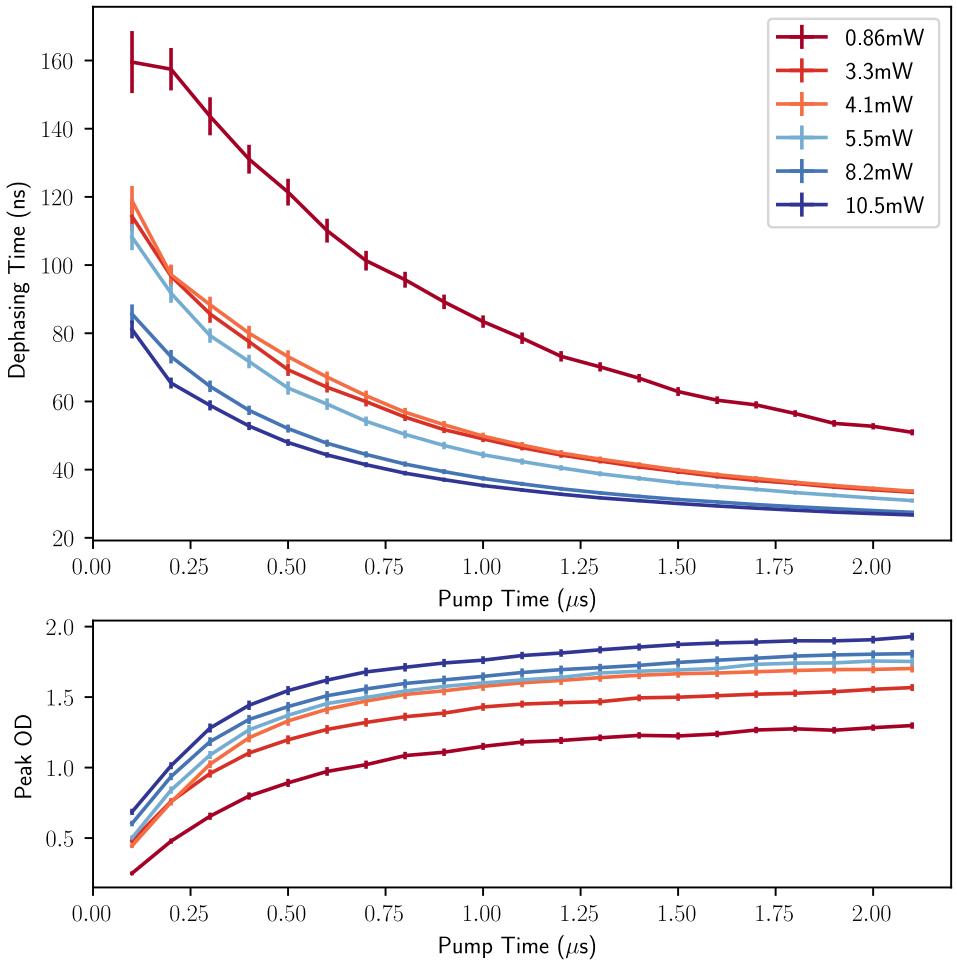

Figure 6.4: Dephasing times (top) and peak optical depths (OD) (bottom) at different pump powers as a function of VSP pump time for 23 °C.

course additional decoherence mechanisms such as hyperfine beating, and atoms drifting out of the beam that would dominate[176]. However, this shows how velocity selective pumping can be used to reduce Doppler dephasing, the dominant decoherence mechanism.

In this section we have described an implementation of a technique for suppressing the primary decoherence mechanism for the implementation of the ORCA quantum memory protocol in warm vapour. This scheme is technically simple and has been shown to be particularly useful in improving the extremely short lifetimes that occur when there is a large

Table 6.1: Predicted $1/e$ timescales for the Doppler dephasing component of the ORCA memory lifetime protocols implemented in Caesium and Rubidium, with and without the application of velocity selective pumping (VSP). In each case we consider two potential upper levels that could be used to form the ladder memory. The enhancement factor, β, is defined as the ratio between the timescales with and without velocity selective pumping.

	Upper Level	Wavelength	No VSP	VSP	β
Cs	$6D_{5/2}$	917 nm	12.5 ns	47.4 ns	3.8
	$7S_{1/2}$	1470 nm	2.3 ns	19.0 ns	8.3
Rb	$5D_{5/2}$	776 nm	97.9 ns	217.4 ns	2.2
	$4D_{5/2}$	1528 nm	1.4 ns	18.9 ns	13.5

wavevector disparity between the signal and control fields. This would enable interfacing of telecom photons with quantum memories, a key step towards the development of a *quantum internet*.

6.2 Atomic Frequency Comb

We notice that the VSP method above is exactly comparable to spectral hole burning [177]: we have taken an inhomogeneously broadened transition and created transparencies at specific frequencies within the transition. In Section 1.3.3, we saw applications of spectral hole burning where it is used to prepare solid state media for quantum memory protocols such as the atomic frequency comb [178], controlled reversible inhomogeneous broadening [179], electromagnetically induced transparency [180], and the spectral-hole memory protocol [181].

In Section 1.3.3, we saw how a photon with a spectral profile spanning periodic spectral-absorption peaks separated by Δ within such a transition can be absorbed. Figure 6.5 shows the properties of an example comb with spacing given by Δ, optical depth d, tooth width γ and total width Γ. The dashed line refers to the orginal inhomogeneously broadened line and d_0 refers to any remaining absorbing background. If the system evolves freely,

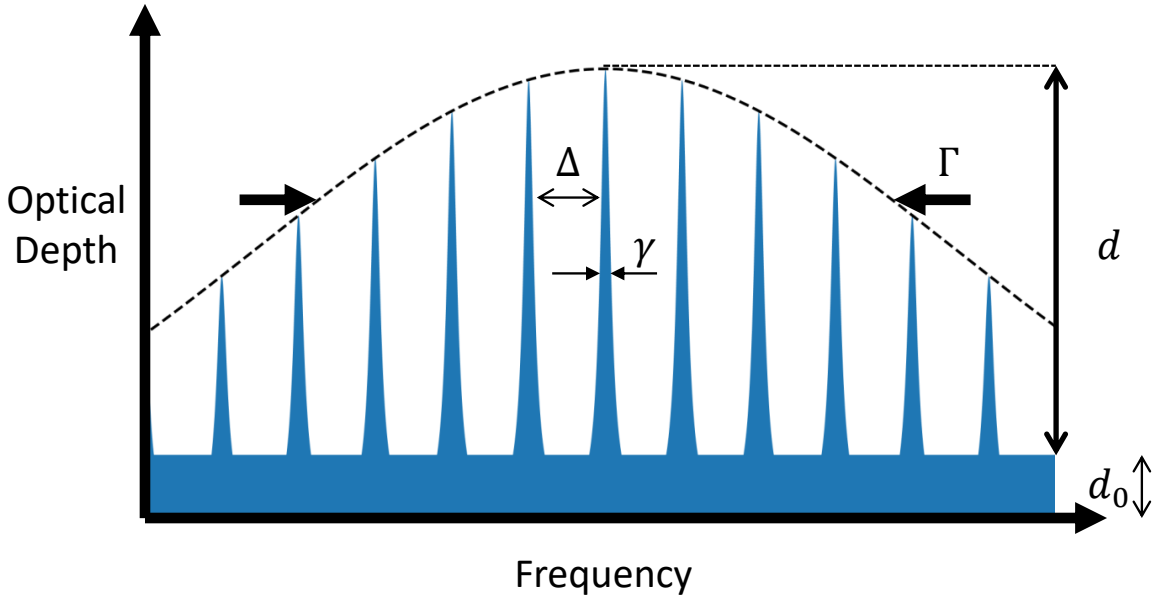

Figure 6.5: Properties of an example atomic frequency comb with comb spacing Δ, optical depth d, tooth width γ and total width Γ. The dashed line refers to the orginal inhomogeneously broadened line and d_0 refers to any remaining absorbing background.

the photon will be coherently re-emitted at time $\tau = 2\pi/\Delta$, as a photon echo. In this section, we apply the VSP technique, outlined in the previous section, to prepare atomic frequency comb structures in warm caesium vapour. We then demonstrate the storage of weak coherent states of light and display the multi-moded nature of the memory.

6.2.1 Velocity selective pumping

Figure 6.6 shows a larger version of the top-centre of Figure 6.3 where a single velocity class is pumped into the $F = 4$ ground state and then probed on the $D2$ transition. From fitting the velocity profile, the width is calculated to be 45 MHz. To extend this scheme to create an AFC we follow the procedure as before with a small change. Applying an RF frequency (from a Agilent RF signal generator) via the bias-T to the VSP laser creates side-bands about the laser's central frequency. Now, instead of a single velocity class being pumped,

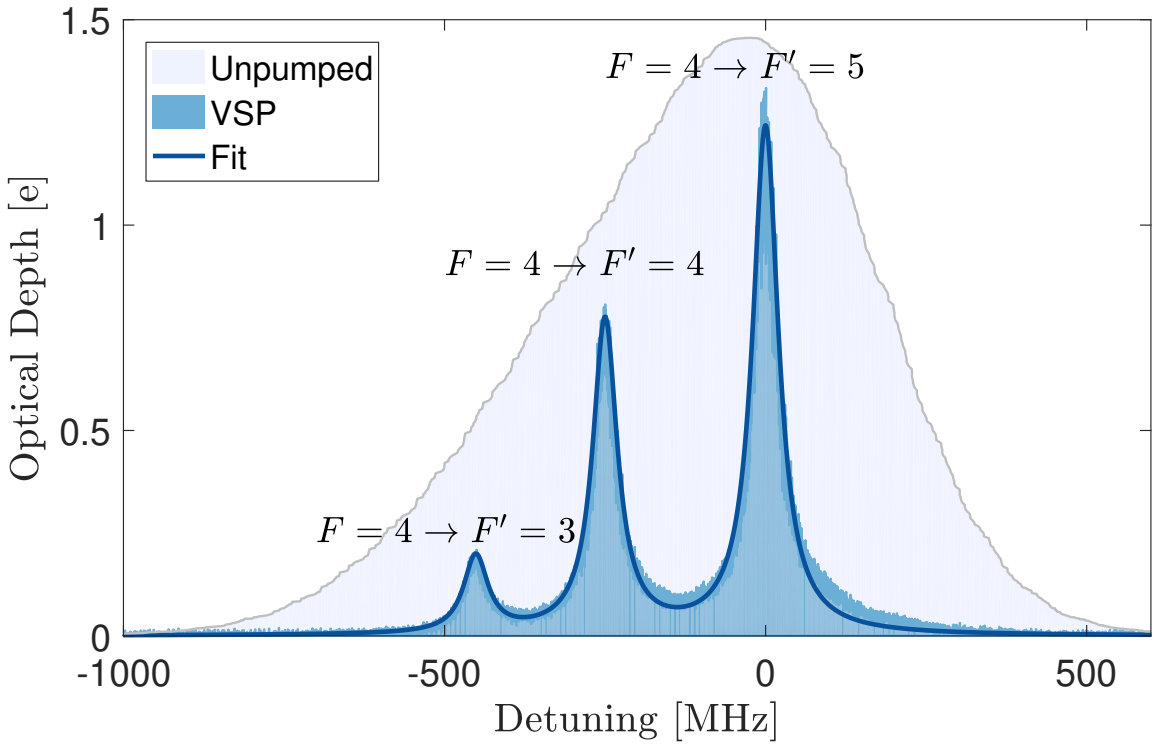

Figure 6.6: Velocity selective optical pumping. A single velocity class is pumped back into the $F = 4$ hyperfine ground state of a caesium vapour. The zero of the frequency axis represents the $F = 4$ to $F' = 5$ transition. The unpumped case is included for comparison. A fit is made to the features, giving a width of about 45 MHz.

multiple velocity classes are pumped to the $F = 4$ state by the side-bands.

By carefully choosing the modulation frequencies we can create comb-like features in the absorption profile of the $D2$ transition, regions of which can have equally spaced teeth. Relative to the $F = 4 \rightarrow F = 4'$ transition the $F' = 3$ and the $F = 5'$ transitions are at -201 MHz and $+251$ MHz respectively. Modulating at a frequency of 125.5 MHz would therefore create the following absorption peaks:

Transition	Absorption peaks MHz
$F = 4 \rightarrow F' = 3$	-326.5, -201,-75.5
$F = 4 \rightarrow F' = 4$	-125.5, 0, +125.5
$F = 4 \rightarrow F' = 5$	+125.5,251,376.5

We can see that the transitions to the $F' = 4$ and $F' = 5$ are linearly spaced with a

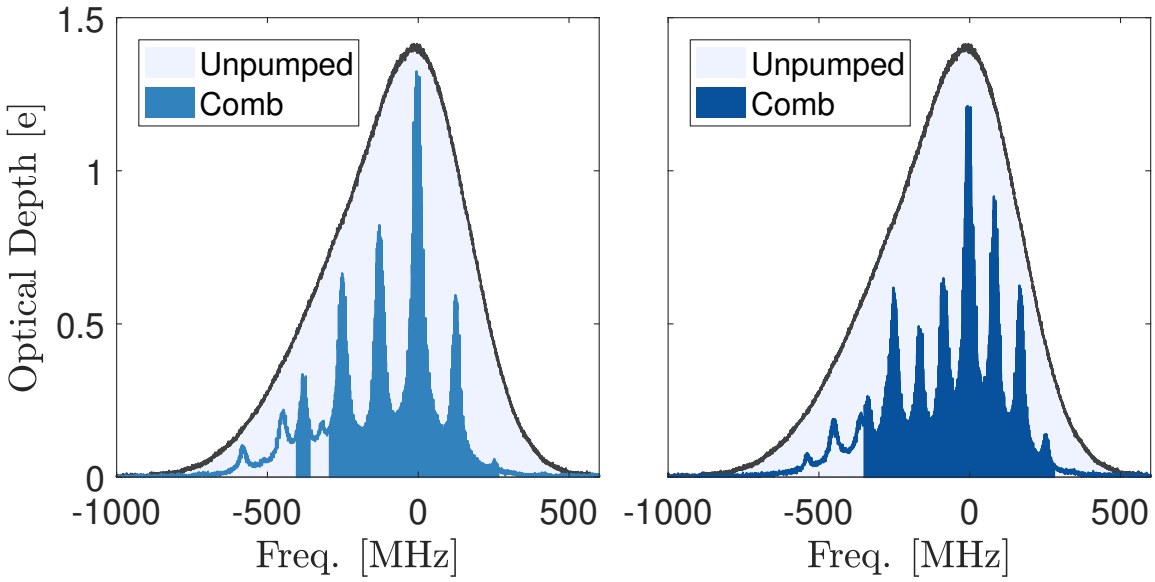

Figure 6.7: Atomic frequency comb spectra prepared in the $F = 4$ hyperfine ground state of caesium. The left panel shows the spectrum for a tooth spacing of $\Delta = 125.5\,\text{MHz}$ while the right panel shows the case for $\Delta = 83.7\,\text{MHz}$. The unpumped $F = 4$ hyperfine ground state is also shown in both panels. The peaks that constitute the AFC are highlighted, indicating a bandwidth of around 0.6 GHz in both cases.

spacing $\Delta = 125.5\text{MHz}$, forming a 5 toothed comb spanning 500 MHz. We also modulate at 83.7 MHz and 167.4 MHz to create the following peaks (only considering the $F' = 4$ and $F' = 5$ transitions):

Transition	Absorption peaks (MHz)
$F = 4 \rightarrow F' = 4$	-167.4, -83.7, 0, 83.7, 167.4
$F = 4 \rightarrow F' = 5$	83.6, 167.3, 251, 334.7, 418.4

These 10 transitions create an 8-toothed comb spanning nearly 0.6 GHz and a tooth spacing $\Delta = 83.7\,\text{MHz}$. The relatively large bandwidth means, if operated as a AFC memory, it would be able to interface with a wide range of photon sources. This relaxes the requirement on developing near MHz single photon sources required for interfacing AFCs based on rare-earths with narrow hyperfine splittings[182]. Figure 6.7 shows absorption spectra of the caesium vapour after we select multiple velocity classes through modulation of the

VSP laser at frequencies 125.5 MHz and 83.7 & 167.3MHz . We have shaded the peaks that constituent the atomic frequency comb with uniform spacing. The VSP duration and power is optimised to give a tooth width of ~ 45 MHz.

6.2.2 Storing a pulse

After preparing the AFC, we propagate a 2ns (FWHM) pulse[4] through the ensemble and record the temporal response. The pulses have $\mathcal{O}(10^3)$ photons in them at the memory, and are recorded on the same avalanche photo-diodes and single photon counting module as described in Section 4.4.1, following attenuation by neutral density filters. We again use an AOM to timegate the light to the detectors, protecting them from the preparation lasers.

Figure 6.8 shows the resultant time-traces when pulses of equal amplitude are propagated through each of the combs. The efficiencies η of the two AFC memories are calculated by centering a 5 ns integration window around each pulse and measuring the ratio of the area of the retrieved pulse to that of the input pulse. The input pulse is measured while performing only the preparation stage of the velocity selective optical pumping (emptying the F=4 stage); omitting the selective pumping stage. The table below summaries the results:

Comb Spacing (Δ)	Time of echo ($1/\Delta$)	Efficiency η (%)
125.5 MHz	7.97 ns	9.3 ± 0.6
83.7 MHz	11.95 ns	3.4 ± 0.3

6.2.3 Multi-modality and conclusion

One of the primary advantages of the AFC memory protocol is its multi-modality [183]; the mode capacity is not limited by optical depth but rather the number of peaks in the comb. This is equivalent to the number of pulses which can be "fit" into the storage time. The

[4] As before, the pulse is carved from a CW Toptica DL Pro laser.

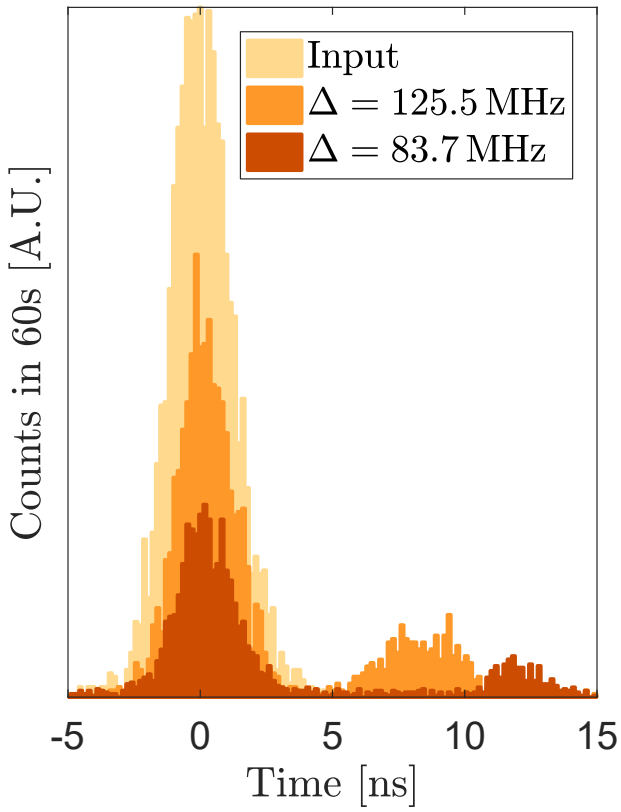

Figure 6.8: Time trace showing the input and resultant echo when sending a 2 ns pulse into the frequency combs shown in Figure 6.7. The storage times of 7.97 ns and 11.95 ns for the $\Delta = 125.5$ MHz and $\Delta = 83.7$ MHz combs respectively. The efficiency is calculated from a 5 ns integration window, centred around the relevant temporal mode.

$\Delta = 83.7$ MHz comb can comfortably accommodate an additional 2 ns pulse before the resultant echo 11.95 ns later. To test if this is possible in our vapour AFC, we send two 2 ns pulses with centres separated by 6 ns. The centre of the pulses we would expect to detect in the series of (input 1, input 2, echo 1, echo 2) are at times (0, 6, 11.95, 17.95)ns respectively. Figure 6.9 shows the timetrace when performing this experiment, and demonstrates that the storage efficiency has remained unchanged.

Afzelius *et al.*[184] derived an analytical expression for the efficiency of an AFC based on

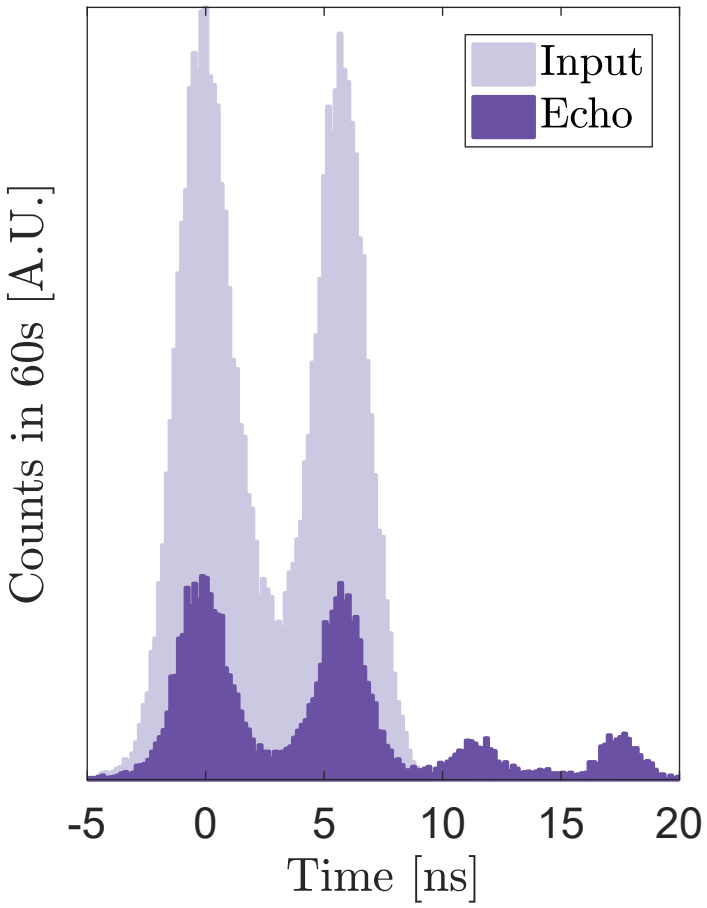

Figure 6.9: Two 2 ns temporal modes separated by 6 ns are stored in the $\Delta = 83.7\,\text{MHz}$ vapour AFC for a duration of 11.95 ns, demonstrating the multimodal capacity of the memory.

the properties of the frequency comb shown in Figure 6.5:

$$\eta_{\text{AFC}} = (d/F)^2\, e^{-d/F}\, e^{-7/F^2}\, e^{-d_0}, \tag{6.4}$$

where $F = \Delta/\gamma$ is the finesse of the AFC, d is the optical depth experienced by the pulse, and d_0 is the absorbing background (occurring when troughs of the comb do not reach full transparency). From probing the spectrum of the $\Delta = 83.7\,\text{MHz}$ comb, we measure the tooth width to be 45 MHz, the tooth depth $d = 0.55$ and the background to be $d_0 = 0.2$. Inputting these parameters into Equation 6.4 yields a predicted efficiency of $\simeq 0.70\%$, which

is nearly five-times less than the measured 3.4%. Understanding the intricacies of this disparity is an active area of research but it is suspected this enhancement is a result of quantum interference. As shown earlier, the $\Delta = 83.7\,\mathrm{MHz}$ comb is comprised of 8 teeth, but the result of 10 peaks, with 2 overlapping. Alternatively this could be considered as two independent combs, one on each transition. Should the echoes from each individual comb be in-phase with one-another the two fields would constructively interfere potentially explaining the observed enhancement.

This chapter has described the development of a velocity selective pumping technique, originally proposed to extend the lifetime of the ORCA memory protocol. The velocity selective pumping scheme was then utilised to demonstrate not only the first AFC memory storage in warm vapour but also demonstrated the potential to store multiple temporal modes. It has also shown the possible enhancement by creating overlapping combs on multiple transitions. Included in the following chapter is an extension that could be made to liken this protocol to the full-AFC memory protocol to make it on-demand instead of a passive delay determined by the tooth spacing.

Chapter 7

Outlook and conclusions

> "There is no real ending. It's just the place where you stop the story."
>
> Frank Herbert

The work presented here represents the latest evolution in the Raman memory experiment. Having been conceived in 2007, the Raman memory has grown and developed into a competitive memory protocol with which to store and retrieve quantum states of light. Previous iterations have made it evident that a solution to the four-wave mixing noise was required before the Raman memory could take its place as a practical candidate for photonic quantum information technologies. Offering broadband storage, a high time-bandwidth product and room temperature operation, the Raman memory is particularly well suited to temporal multiplexing tasks. More recently, exploitation of a photon's temporal-spectral degree of freedom has led to a host of applications for which the Raman memory is also particularly well suited. Finally, my work on atom-light interactions within warm vapour also yielded the demonstration of an atomic-frequency comb memory; the first demonstration of this protocol in warm vapour. This further expands the applications of warm-vapours for quantum memory applications.

Below I will summarise my achievements described in this thesis.

7.1 Summary

After establishing the principles of quantum memories, Chapter 2 presented a derivation of the Raman memory interaction. The significance, compared to early derivations, was the inclusion of the anti-Stokes field to the equations of motion. I then described how I numerically simulated the memory process in Python and outlined a brief history of the Raman memory. With the focus on four-wave mixing noise, Chapter 3 saw the conception of a tool with which to analyse noise emanating from the Raman memory. By examining the photon statistics of the retrieved state, the various noise contributions could be inferred. This tool is then tested in Chapter 4, and shows the resounding success of a novel noise suppression scheme. By engineering the Raman memory detuning such that the anti-Stokes scattered light is placed on resonance with the populated transition, we are able to show near-total eradication of FWM noise. Furthermore, we are able to predict non-classical recall from a single-photon source with a heralding efficiency greater than a modest 10.5%.

Given the possibility for this iteration of the Raman memory to function at the single-photon level, I go on to consider temporal-spectral manipulation to bolster the applications of the memory. Before applying temporal modes to the memory, in Section 5.2.1, I construct a proof-of-principle experiment to measure the overlap between two temporal pulses. I then proceed to show how the Raman memory's efficiency can be enhanced by increasing the control power and carving the optimum signal mode. This optimum mode compensates for the AC-Stark shift that would otherwise occur at high control field powers and is derived from the singular-value decomposition of the Green's function of the memory interaction.

Following this, I go on to demonstrate the memory as a single-mode device which can separate and convert between temporal modes of light, including bandwidth conversion and perform quantum gates in the high-dimensional QIP alphabet given by Hermite-Gauss modes.

Chapter 6, describes a velocity selective technique which can be used to reduce Doppler-dephasing of an atomic memory's spin-wave. Using this technique we show how an ORCA protocol memory's lifetime can be significantly extended, and posit the application to further interface with telecom-band photons. This is otherwise very difficult as the large wave-vector mismatch between the signal and control severly impacts the storage lifetime due to Doppler dephasing. The velocity selection method comes at the cost of optical depth, and hence efficiency, as fewer atoms are participating in the memory protocol. This technique is then used to create an atomic-frequency comb in warm Cs vapour, and we demonstrate both storage of a weak coherent state using two different tooth-separations and the multi-modality of this AFC storage protocol.

There are many exciting avenues with which to continue the research contained within this thesis and I discuss them in the following section.

7.2 Future Experiments

7.2.1 Single Photon Storage

The Raman memory has so far been tested with weak coherent states, showing significant suppression of noise created by four-wave mixing. The logical progression of the work in Chapter 4 is the storage of heralded single photons, when operating at the *magic* detuning. We have already demonstrated that we have reached the threshold required to maintain

the non-classicality of a single-photon state, but further noise suppression is possible. The remaining noise is the result of imperfect pumping and fluorescence due to linear absorption of the control. Improved pumping effiency, and therefore less spontaneous Raman scattering, can be achieved by using a Pockels cell instead of an EOM as discussed in Section 4.4.3. That section also discusses improvements that could be made to the filtering set-up. At the moment, two of the three double-passed spectral-filtering etalons have an FSR of 18.4 GHz. This means, when the signal is at the *magic* detuning $\Delta = -18.4\,\text{GHz}$ they transmit fluorescence noise. Using etalons with varying FSRs will enable large suppression of the fluorescence noise. With these improvements, I am confident single-photon storage will be possible, paving the way for the following three experiments.

7.2.2 Multi-photon rate enhancement

An important example of temporal multiplexing is shown in Section 1.3.1 with the synchronisation of probabilistic heralded photon sources. The time-bandwidth product of the Raman memory is such that significant gains can be made to the rates of these photon sources. The simplest proof-of-principle demonstration of this can be achieved with just a single SPDC source and a single memory. The memory is initalised by storing a heralded photon, and following the detection of a second herald photon, the stored excitation is retrieved. The retrieval is performed such that the retrieved photon coincides with the second SPDC photon from the source. By comparing the coincidence rate to the probability of generating two photons from independent sources[1] we can demonstrate the enhancement offered by the memory. Future experiments, demonstrating the synchronisation of large

[1]The probability of two photons from two independent sources is given by the product of the heralding efficiencies of the sources.

multi-photon states involving multiple sources and multiple memories could then follow.

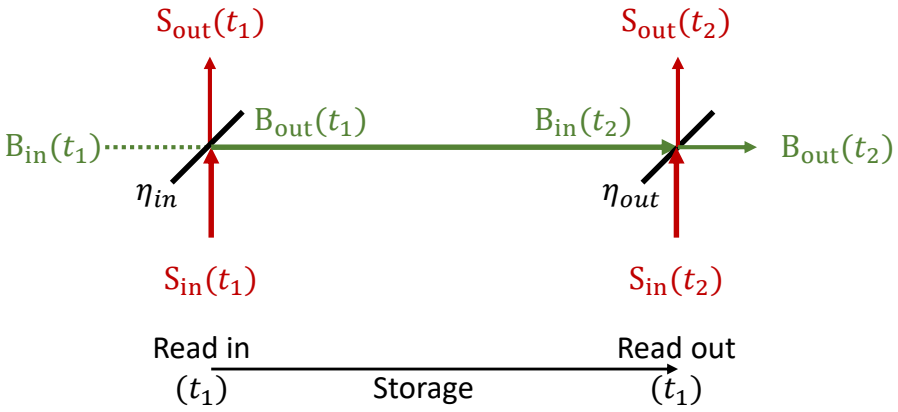

Figure 7.1: The Raman memory interaction as a beam splitter for optical $S_{in/out}$ and spin-wave modes $B_{in/out}$. Under normal operation $S_{\text{in}}(t_2)$ would be vacuum, however during the HOM experiment it is a photon to produce the state $\frac{1}{\sqrt{2}}(|2,0\rangle + |0,2\rangle)$.

7.2.3 Light-Matter HOM

Beam-splitter interactions have proved a central theme to this thesis; from the Hanbury Brow-Twiss experiment to measure the $g^{(2)}$ statistics of a state using a beam-splitter in Chapter 3, to using Hong-Ou-Mandel interference to measure temporal mode overlap in Section 5.2.1. The memory interaction itself, as mentioned in Chapter 2, acts as a beam-splitter – transforming an incident photon mode into a transmitted photon and a matter excitation. This lends itself to an exciting experiment, performing this archetypal quantum optics experiment, within a Raman memory and can be performed in the following way [185]:

1. The read-in and read-out efficiencies of the memory are tuned to 50%, and a heralded single photon is propagated through the memory (with a read-in control pulse).

2. In the cases when a photon is stored[2], a second photon is sent into the memory,

[2]Requiring a difficult, heralding on vacuum, measurement.

again with a read-in control pulse. This control pulse can, however, also act as a read-out pulse for the stored excitation. The state just before this second interaction is $|B, S_{\text{in}}\rangle = |1, 1\rangle$ where B is the stored matter excitation, and S_{in} is the second incident photon. The subsequent results of the beam-splitter interaction within the memory are that either, the second photon is stored as an additional matter excitation, or the second photon is transmitted *and* the stored photon is retrieved. This therefore creates the 2 excitation NOON-state $\frac{1}{\sqrt{2}}(|2, 0\rangle + |0, 2\rangle)$.

3. One could confirm the success of this NOON-state construction by a) Looking at the two-photon contribution of the photonic part of the NOON-state, either with photon-number resolving detectors or with a HBT measurement or b) by sending a third, read-out only, control pulse to the memory (this can be done with a higher power such to maximise the likelihood of emptying the memory). If a HOM interference was demonstrated then there would be a reduced chance of coincidences (ideally zero coincidences) between the first and second retrieval events.

7.2.4 Temporal Mode Manipulation

Section 5.3 detailed a number of experiments performed with coherent states (and in the case of maximising the efficiency, performed only theoretically). Performing these experiments with single-photons would demonstrate a significant milestone in affirming the Raman memory as a crucial device within photonic quantum information. Of particular note would be mode manipulation; using the Raman memory to turn one temporal mode into another. The manipulations performed for temporal modes were thus far broadly qualitative, as only the intensity of the resultant pulse was measured (by APDs). The fundamental test will be

converting one temporal mode to another; the fidelity of this conversion can be measured with a HOM measurement. This can be realised by comparing two orthogonal modes, and then manipulating one, converting it and then re-comparing; the aim being for the two states to now be identical. This represents a quantum gate within the high dimensional Hilbert space offered by Hermite-Gauss temporal modes.

The indistinguishability of the two states would be easier to achieve if both states had been previously stored (for example by two different memories), and subsequently retrieved using the same control pulse. This has the disadvantage of requiring multiple memories, and may potentially suffer from a drop in rates. This would however ensure that the two signals are identical, compared to the not insignificant task of engineering one to exactly match the other, unaltered signal. Another, and conceptually interesting way, to interfere the two orthogonal temporal modes is using the HOM experiment from the previous section. When operated in the single-mode regime all temporal modes are stored within the same spin-wave mode and are insensitive to the input temporal mode, hence the HOM "bunching" and two photon interference will occur *within* the memory.

7.3 Atomic frequency comb

Chapter 6 showed storage of weak coherent states in an atomic frequency comb created by velocity selective pumping in warm vapour. At present, the storage time is dictated by the tooth spacing of the created comb, however this could be extended in a similar fashion to the full spin-wave AFC protocol[186], by mapping the excitation into a long-lived state using a control pulse. Unfortunately for our system we use the other ground-state to "hold" the atoms with un-selected velocities, however, by exploiting the ORCA protocol[171,172]

we could use an upper transition in a ladder-like scheme. The comparatively strong dipole moment associated with these transitions allows them to be accessed with very achievable, (GHz Rabi frequency) control field powers.

The proposal[3] to combine the AFC and ORCA-ladder memory schemes is as follows: After first preparing an AFC, the ORCA protocol is implemented to store the excitation in a doubly excited state. This is achieved by applying an off-resonant control field for the upper transition and the signal similarly detuned from the lower transition. A second control pulse, applied at the AFC-rephasing time τ, will retrieve the excitation from the memory. After a time τ, without a control pulse, the excitation will not be phase-matched and hence cannot be retrieved. Likewise, should the control pulse be applied at a time $t \neq n\tau$, the excitation will not be phase-matched and will not be retrieved. Hence the coherence can only be read-out at a time that is an integer multiple (n) of the rephasing time, creating an on-demand (modulo τ) quantum memory.

7.4 Conclusion

Over the course of this body of work I have presented the theory and implementation of a novel noise suppression scheme for the Raman quantum memory. The reduction in noise is such that the memory is predicted to be functional at the single photon level, and offer applications in temporal multiplexing for photonic quantum information. This also led to a means to characterise different sources of noise when testing memory protocols using photon statistics, not specific to the Raman protocol. Furthermore, I have begun to explore new applications for the Raman memory, exploiting its single-moded nature and

[3]Devised by P.M.L and based on a similar proposal by Rubio *et al.* [187].

manipulating temporal modes of light. Although these are just the first steps, they lay significant groundwork for the memory to be a useful device when utilising the quantum network possibilities offered by temporal modes. Finally, investigations into extending the lifetime of memories in warm atomic vapour led to the first demonstration of photon storage using a atomic frequency comb in warm vapour. All in all, I think the theory, experiments, and subsequent discussions here represent a significant contribution towards the goal of realising the full potential of photonic quantum information with quantum memories.

Appendix A

Quantum Optics

"The tale grew in the telling."

J.R.R. Tolkien

A.1 Fock States I

The photon number states $|n\rangle$ are simultaneous eigenstates of the number operator $\hat{n} = \hat{a}^\dagger \hat{a}$ and the Hamiltonian for a one-dimensional harmonic oscillator:

$$\begin{aligned} \hat{n}\,|n\rangle &= \hat{a}^\dagger \hat{a}\,|n\rangle = n\,|n\rangle \\ \hat{H}\,|n\rangle &= \hbar\omega\left(\hat{a}^\dagger\hat{a} + \frac{1}{2}\right)|n\rangle = \left(n + \frac{1}{2}\right)\hbar\omega\,|n\rangle = E_n\,|n\rangle\,. \end{aligned} \tag{A.1}$$

By applying the creation operator $\hat{a}^\dagger$ to the second of these equations and making use of the commutation relation $[\hat{a}, \hat{a}^\dagger] = 1$, we find that:

$$\hbar\omega\left(\hat{a}^\dagger\hat{a}^\dagger\hat{a} + \frac{1}{2}\hat{a}^\dagger\right)|n\rangle = \hbar\omega\left(\hat{a}^\dagger\hat{a}\hat{a}^\dagger - \hat{a}^\dagger + \frac{1}{2}\hat{a}^\dagger\right)|n\rangle = E_n\hat{a}^\dagger\,|n\rangle\,, \tag{A.2}$$

which can be re-arranged to give:

$$\hbar\omega\left(\hat{a}^\dagger\hat{a}+\frac{1}{2}\right)\hat{a}^\dagger\left|n\right\rangle=(E_n+\hbar\omega)\hat{a}^\dagger\left|n\right\rangle. \tag{A.3}$$

The state $\hat{a}^\dagger\left|n\right\rangle$ is therefore an eigenstate of $\hat{H}$ with eigenvalue $E_n+\hbar\omega$ so we may write $C_{n+1}\left|n+1\right\rangle=\hat{a}^\dagger\left|n\right\rangle$ and likewise, $C_n\left|n-1\right\rangle\hat{a}\left|n\right\rangle$. The normalisation constants are given by $C_{n+1}=\sqrt{n+1}$ and $C_n=\sqrt{n}$. Hence,

$$\begin{aligned}\hat{a}^\dagger\left|n\right\rangle&=\sqrt{n+1}\left|n+1\right\rangle\\ \hat{a}\left|n\right\rangle&=\sqrt{n}\left|n-1\right\rangle\end{aligned} \tag{A.4}$$

The $g^{(2)}(0)$ for a single-mode Fock state $\left|n\right\rangle$ is then given by:

$$g^{(2)}(0)=\frac{\left\langle n\right|\hat{a}^\dagger\hat{a}^\dagger\hat{a}\hat{a}\left|n\right\rangle}{\left\langle n\right|\hat{a}^\dagger\hat{a}\left|n\right\rangle^2}=\frac{n(n-1)}{n^2}=1-\frac{1}{n}<1. \tag{A.5}$$

A.2 Fock States II

Here we explicitly define the creation operator for the signal (and anti-Stokes) modes at a time t_i with temporal mode $\sigma(t_1)$ (where $\int|\sigma(t_1)|^2\mathrm{d}t_1=1$). We use them to define a Fock state of n photons like so:

$$\left|n_\sigma^{(1)}\right\rangle=\int\frac{\sigma(t_1)(S_1^\dagger)^n}{\sqrt{n!}}\left|0\right\rangle\mathrm{d}t_1=\frac{1}{\sqrt{n!}}\int\sigma(t_1)(S_1^\dagger)^n\left|0\right\rangle\mathrm{d}_1 \tag{A.6}$$

where the $^{(1)}$ index, whilst integrated over and therefore semi-redundant, it's useful to keep track of. $\sigma(t_1)=\sigma_1$ and $\mathrm{d}t_1=\mathrm{d}_1$ for brevity. There are also two Bosonic commutation

relations (BCR and BCR2) which will be used. They are:

$$\text{BCR: } [S_i, S_j^\dagger] = \delta(t_i - t_j) \equiv \delta_{ij} \qquad \text{BCR2: } [S_i, (S_j^\dagger)^n] \equiv n\delta_{ij}(S_j^\dagger)^{(n-1)} \tag{A.7}$$

Annihilation on Fock State

Consider the action of operator S_1 on Fock state $\left|n_\sigma^{(2)}\right\rangle$:

$$\begin{aligned}
\int S_1 \left|n_\sigma^{(2)}\right\rangle \mathrm{d}_1 &= \frac{1}{\sqrt{n!}} \int \sigma_2 S_1 (S_2^\dagger)^n \left|0\right\rangle \mathrm{d}_{12} \\
\text{(Using BCR2)} \qquad &= \frac{n}{\sqrt{n}\sqrt{(n-1)!}} \int \sigma_2 \delta_{12} (S_2^\dagger)^{(n-1)} \left|0\right\rangle \mathrm{d}_{12} \\
&= \sqrt{n} \frac{1}{\sqrt{(n-1)!}} \int \sigma(t_1) (S_1^\dagger)^{(n-1)} \left|0\right\rangle \mathrm{d}_1 \\
\therefore \int S_1 \left|n_\sigma^{(2)}\right\rangle \mathrm{d}_1 &= \sqrt{n} \left|(n-1)_\sigma^{(1)}\right\rangle
\end{aligned} \tag{A.8}$$

Overlap of Two Fock States

Does $\left\langle n_\sigma^{(1)} \middle| n_\sigma^{(2)} \right\rangle = \int \sigma_1^* \sigma_2 \delta_{12} \mathrm{d}_{12} (\equiv 1)$? Answer - yes (when the temporal modes are the same), now a proof by induction.

$$\begin{aligned}
n = 1 \qquad \left\langle 1_\sigma^{(1)} \middle| 1_\sigma^{(2)} \right\rangle &= \int \sigma_1^* \sigma_2 \left\langle 0\right| S_1 S_2^\dagger \left|0\right\rangle \mathrm{d}_{12} \\
&= \int \sigma_1^* \sigma_2 \delta_{12} \mathrm{d}_{12} \\
\text{Assume true for } n = k \qquad \left\langle k_\sigma^{(1)} \middle| k_\sigma^{(2)} \right\rangle &= \int \frac{\sigma_1^* \sigma_2}{k!} \left\langle 0\right| (S_1)^k (S_2^\dagger)^k \left|0\right\rangle \mathrm{d}_{12} \\
&= \int \sigma_1^* \sigma_2 \delta_{12} \mathrm{d}_{12} \\
\text{Consider } n = k+1 \qquad \left\langle (k+1)_\sigma^{(1)} \middle| (k+1)_\sigma^{(2)} \right\rangle &= \int \frac{\sigma_1^* \sigma_2}{(k+1)!} \left\langle 0\right| (S_1)^{(k+1)} (S_2^\dagger)^{(k+1)} \left|0\right\rangle \mathrm{d}_{12}
\end{aligned}$$

$$\begin{aligned}
\left\langle (k+1)_\sigma^{(1)} \middle| (k+1)_\sigma^{(2)} \right\rangle &= \int \frac{\sigma_1^* \sigma_2}{(k+1)!} \langle 0| \, S_1^k S_1 (S_2^\dagger)^{(k+1)} \, |0\rangle \, \mathrm{d}_{12} \\
\text{(BCS2)} \qquad &= \int \frac{\sigma_1^* \sigma_2}{(k+1)!} \langle 0| \, S_1^k (S_2^\dagger)^k \, |0\rangle \, (k+1) \delta_{12} \mathrm{d}_{12} \\
&= \int \frac{\sigma_1^* \sigma_2}{k!} \langle 0| \, (S_1)^k (S_2^\dagger)^k \, |0\rangle \, \mathrm{d}_{12} = \left\langle k_\sigma^{(1)} \middle| k_\sigma^{(2)} \right\rangle \\
&= \int \sigma_1^* \sigma_2 \delta_{12} \mathrm{d}_{12} \\
\therefore \left\langle n_\sigma^{(1)} \middle| n_\sigma^{(2)} \right\rangle &= \int \sigma_1^* \sigma_2 \delta_{12} \mathrm{d}_{12}
\end{aligned} \tag{A.9}$$

Note - this also shows $\left\langle n_\sigma^{(1)} \middle| m_\sigma^{(2)} \right\rangle = 0$ for $n \neq m$ as would result in $\langle 0| \, S_1^k \, |0\rangle$ or $\langle 0| \, (S_1^\dagger)^k \, |0\rangle$ both of which equate to zero. There may also be times we are to consider the interaction of two differing temporal modes:

$$\left\langle n_\alpha^{(1)} \middle| n_\beta^{(2)} \right\rangle = \int \alpha_1^* \beta_2 \delta_{12} \mathrm{d}_{12} \tag{A.10}$$

This the result is therefore given by the overlap integral of the two modes. We use this when considering the mode selectivity of the memory interaction.

"Number Operator"

Consider $\int \left\langle n_\sigma^{(3)} \right| S_1^\dagger S_2 \left| n_\sigma^{(4)} \right\rangle \mathrm{d}_{12}$ Using Equation A.8 and then Equation A.9 this is clearly:

$$\begin{aligned}
\int \left\langle n_\sigma^{(3)} \right| S_1^\dagger S_2 \left| n_\sigma^{(4)} \right\rangle \mathrm{d}_{12} &= n \left\langle (n-1)_\sigma^{(1)} \middle| (n-1)_\sigma^{(2)} \right\rangle \\
&= n \int \sigma_1^* \sigma_2 \delta_{12} \mathrm{d}_{12} \\
&= n
\end{aligned} \tag{A.11}$$

Similarly we can consider the term we'll use in the $g^{(2)}$.

$$\begin{aligned}\int \left\langle n_\sigma^{(5)} \right| S_1^\dagger S_2^\dagger S_3 S_4 \left| n_\sigma^{(6)} \right\rangle \mathrm{d}_{1234} &= n \int \left\langle (n-1)_\sigma^{(1)} \right| S_2^\dagger S_3 \left| (n-1)_\sigma^{(4)} \right\rangle \mathrm{d}_{23} \\ &= n(n-1) \left\langle (n-2)_\sigma^{(2)} \right| \left. (n-2)_\sigma^{(3)} \right\rangle \\ &= n(n-1) \int \sigma_2^* \sigma_3 \delta_{23} \mathrm{d}_{23} \\ &= n(n-1) \end{aligned} \tag{A.12}$$

Input States

Now our signal input state might be a single photon or approximately a single photon with a non-zero $g^{(2)}$ or a coherent state or a thermal state etc. Either which way we can write as a linear combination of Fock states with the same temporal mode.

$$\left| \psi_{s,\sigma}^{(1)} \right\rangle = \sum_n c_n \left| n_\sigma^{(1)} \right\rangle \tag{A.13}$$

The number(-ish) operator on this is then:

$$\begin{aligned}\int \left\langle \psi_{s,\sigma}^{(3)} \right| S_1^\dagger S_2 \left| \psi_{s,\sigma}^{(4)} \right\rangle \mathrm{d}_{12} &= \sum_{m,n} c_m^* c_n \sqrt{mn} \left\langle (m-1)_\sigma^{(1)} \right| \left. (n-1)_\sigma^{(2)} \right\rangle \\ &= \sum_{m,n} c_m^* c_n \sqrt{mn} \delta_{mn} \int \sigma_1^* \sigma_2 \delta_{12} \mathrm{d}_{12} \\ &= \sum_n |c_n|^2 n \int \sigma_1^* \sigma_2 \delta_{12} \mathrm{d}_{12} \\ \therefore \int \left\langle \psi_{s,\sigma}^{(3)} \right| S_1^\dagger S_2 \left| \psi_{s,\sigma}^{(4)} \right\rangle \mathrm{d}_{12} &= \langle n \rangle \int \sigma_1^* \sigma_2 \delta_{12} \mathrm{d}_{12} \\ &= \langle n \rangle \end{aligned} \tag{A.14}$$

(In an effort to be helpful I have occasionally left in apparently redundant δ_{ij}. These are for when the full calculation requires a Green's function with this index to be integrated over).

Bibliography

[1] Glosser.ca Wikimedia Commons. Bloch sphere, 2012. Used under creative commons license.

[2] John S Bell. On the einstein podolsky rosen paradox. *Physics Physique Fizika*, 1(3):195, 1964.

[3] John F Clauser, Michael A Horne, Abner Shimony, and Richard A Holt. Proposed experiment to test local hidden-variable theories. *Physical review letters*, 23(15):880, 1969.

[4] Bas Hensen, Hannes Bernien, Anaïs E Dréau, Andreas Reiserer, Norbert Kalb, Machiel S Blok, Just Ruitenberg, Raymond FL Vermeulen, Raymond N Schouten, Carlos Abellán, et al. Loophole-free bell inequality violation using electron spins separated by 1.3 kilometres. *Nature*, 526(7575):682–686, 2015.

[5] Emanuele Polino, Mauro Valeri, Nicolò Spagnolo, and Fabio Sciarrino. Photonic quantum metrology. *AVS Quantum Science*, 2(2):024703, 2020.

[6] Fred Piper. Cryptography. *Encyclopedia of Software Engineering*, 2002.

[7] Charles H Bennett and Gilles Brassard. Quantum cryptography: Public key distribution and con tos5. In *Proceedings of the International Conference on Computers, Systems and Signal Processing*, pages 175–179, 1984.

[8] Artur K Ekert. Quantum cryptography based on bell's theorem. *Physical review letters*, 67(6):661, 1991.

[9] Juan Yin, Yuan Cao, Yu-Huai Li, Sheng-Kai Liao, Liang Zhang, Ji-Gang Ren, Wen-Qi Cai, Wei-Yue Liu, Bo Li, Hui Dai, et al. Satellite-based entanglement distribution over 1200 kilometers. *Science*, 356(6343):1140–1144, 2017.

[10] Mark Howard, Joel Wallman, Victor Veitch, and Joseph Emerson. Contextuality supplies the 'magic'for quantum computation. *Nature*, 510(7505):351–355, 2014.

[11] Robert B Griffiths. Quantum measurements and contextuality. *Philosophical Transactions of the Royal Society A*, 377(2157):20190033, 2019.

[12] Costantino Budroni, Adán Cabello, Otfried Gühne, Matthias Kleinmann, and Jan-Åke Larsson. Quantum contextuality. *arXiv preprint arXiv:2102.13036*, 2021.

[13] Peter W Shor. Polynomial-time algorithms for prime factorization and discrete logarithms on a quantum computer. *SIAM review*, 41(2):303–332, 1999.

[14] Marije Elkenbracht-Huizing. An implementation of the number field sieve. *Experimental Mathematics*, 5(3):231–253, 1996.

[15] Alfred J Menezes, Paul C Van Oorschot, and Scott A Vanstone. *Handbook of applied cryptography*. CRC press, 2018.

[16] Lieven MK Vandersypen, Matthias Steffen, Gregory Breyta, Costantino S Yannoni, Mark H Sherwood, and Isaac L Chuang. Experimental realization of shor's quantum factoring algorithm using nuclear magnetic resonance. *Nature*, 414(6866):883–887, 2001.

[17] Enrique Martin-Lopez, Anthony Laing, Thomas Lawson, Roberto Alvarez, Xiao-Qi Zhou, and Jeremy L O'brien. Experimental realization of shor's quantum factoring algorithm using qubit recycling. *Nature photonics*, 6(11):773–776, 2012.

[18] Lov K Grover. A fast quantum mechanical algorithm for database search. In *Proceedings of the twenty-eighth annual ACM symposium on Theory of computing*, pages 212–219, 1996.

[19] Nathan Wiebe, Daniel Braun, and Seth Lloyd. Quantum algorithm for data fitting. *Physical review letters*, 109(5):050505, 2012.

[20] Aram W Harrow, Avinatan Hassidim, and Seth Lloyd. Quantum algorithm for linear systems of equations. *Physical review letters*, 103(15):150502, 2009.

[21] X-D Cai, Christian Weedbrook, Z-E Su, M-C Chen, Mile Gu, M-J Zhu, Li Li, Nai-Le Liu, Chao-Yang Lu, and Jian-Wei Pan. Experimental quantum computing to solve systems of linear equations. *Physical review letters*, 110(23):230501, 2013.

[22] David P DiVincenzo. The physical implementation of quantum computation. *Fortschritte der Physik: Progress of Physics*, 48(9-11):771–783, 2000.

[23] Alan Migdall, Sergey V Polyakov, Jingyun Fan, and Joshua C Bienfang. *Single-photon generation and detection: physics and applications*. Academic Press, 2013.

[24] CK Hong, Zhe-Yu Ou, and Leonard Mandel. Measurement of subpicosecond time intervals between two photons by interference. *Physical review letters*, 59(18):2044, 1987.

[25] W. Boyd. *Nonlinear Optics*. Academic Press, 2003.

[26] A. L. Migdall, D. Branning, and S. Castelletto. Tailoring single-photon and multiphoton probabilities of a single-photon on-demand source. *Phys. Rev. A*, 66(053805), 2002.

[27] P. Michler, A. Kiraz, C. Becher, W. V. Schoenfeld, P. M. Petroff, L. Zhang, E. Hu, and A. Imamoglu. A quantum dot single-photon turnstile device. *Science*, 290, 2000.

[28] M. Muller, S. Bounouar, K. D. Jons, M. Glassl, and P. Michler. On-demand generation of indistinguishablepolarization-entangled photon pairs. *Nature Photonics*, 8, 2014.

[29] O. Gazzano, S. Michaelis de Vasconcellos, C. Arnold, A. Nowak, E. Galopin, I. Sagnes, L. Lanco, A. Lemaitre, and P. Senellart. Bright solid-state sources of indistinguishable single photons. *Nat. Comms.*, 4(1425), 2013.

[30] J. C. Loredo, N. A. Zakaria, N. Somaschi, C. Anton, L. de Santis, V. Giesz, T. Grange, M. A. Broome, O. Gazzano, G. Coppola, I. Sagnes, A. Lemaitre, A. Auffeves, P. Senellart, M. P. Almeida, and A. G. White. Scalable performance in solid-state single-photon sources. *Optica*, 3(4), 2016.

[31] Natasha Tomm, Alisa Javadi, Nadia Olympia Antoniadis, Daniel Najer, Matthias Christian Löbl, Alexander Rolf Korsch, Rüdiger Schott, Sascha René Valentin, Andreas Dirk Wieck, Arne Ludwig, et al. A bright and fast source of coherent single photons. *Nature Nanotechnology*, 16(4):399–403, 2021.

[32] Samuel L Braunstein and Arun K Pati. *Quantum information with continuous variables*. Springer Science & Business Media, 2012.

[33] Linda Sansoni, Fabio Sciarrino, Giuseppe Vallone, Paolo Mataloni, Andrea Crespi, Roberta Ramponi, and Roberto Osellame. Polarization entangled state measurement on a chip. *Physical review letters*, 105(20):200503, 2010.

[34] Andrea Crespi, Roberta Ramponi, Roberto Osellame, Linda Sansoni, Irene Bongioanni, Fabio Sciarrino, Giuseppe Vallone, and Paolo Mataloni. Integrated photonic quantum gates for polarization qubits. *Nature communications*, 2(1):1–6, 2011.

[35] Pierre Vernaz-Gris, Kun Huang, Mingtao Cao, Alexandra S Sheremet, and Julien Laurat. Highly-efficient quantum memory for polarization qubits in a spatially-multiplexed cold atomic ensemble. *Nature communications*, 9(1):1–6, 2018.

[36] Damien Bonneau, Mirko Lobino, Pisu Jiang, Chandra M Natarajan, Michael G Tanner, Robert H Hadfield, Sanders N Dorenbos, Val Zwiller, Mark G Thompson, and Jeremy L O'Brien. Fast path and polarization manipulation of telecom wavelength single photons in lithium niobate waveguide devices. *Physical review letters*, 108(5):053601, 2012.

[37] Tian Zhong, Xiaolong Hu, Franco NC Wong, Karl K Berggren, Tony D Roberts, and Philip Battle. High-quality fiber-optic polarization entanglement distribution at 1.3 μm telecom wavelength. *Optics letters*, 35(9):1392–1394, 2010.

[38] Chao-Yang Lu, Daniel E Browne, Tao Yang, and Jian-Wei Pan. Demonstration of a compiled version of shor's quantum factoring algorithm using photonic qubits. *Physical Review Letters*, 99(25):250504, 2007.

[39] Qiang Zhang, Xiao-Hui Bao, Chao-Yang Lu, Xiao-Qi Zhou, Tao Yang, Terry Rudolph, and Jian-Wei Pan. Demonstration of a scheme for the generation of "event-ready" entangled photon pairs from a single-photon source. *Physical Review A*, 77(6):062316, 2008.

[40] Dirk Heinze, Artur Zrenner, and Stefan Schumacher. Polarization-entangled twin photons from two-photon quantum-dot emission. *Physical Review B*, 95(24):245306, 2017.

[41] Paul G Kwiat, Klaus Mattle, Harald Weinfurter, Anton Zeilinger, Alexander V Sergienko, and Yanhua Shih. New high-intensity source of polarization-entangled photon pairs. *Physical Review Letters*, 75(24):4337, 1995.

[42] Li-Ping Deng, Haibo Wang, and Kaige Wang. Quantum cnot gates with orbital angular momentum and polarization of single-photon quantum logic. *JOSA B*, 24(9):2517–2520, 2007.

[43] Vincenzo D'Ambrosio, Eleonora Nagali, Carlos H Monken, Sergei Slussarenko, Lorenzo Marrucci, and Fabio Sciarrino. Deterministic qubit transfer between orbital and spin angular momentum of single photons. *Optics letters*, 37(2):172–174, 2012.

[44] Mohammad Mirhosseini, Omar S Magaña-Loaiza, Malcolm N O'Sullivan, Brandon Rodenburg, Mehul Malik, Martin PJ Lavery, Miles J Padgett, Daniel J Gauthier, and Robert W Boyd. High-dimensional quantum cryptography with twisted light. *New Journal of Physics*, 17(3):033033, 2015.

[45] Bao-Cang Ren, Hai-Rui Wei, and Fu-Guo Deng. Deterministic photonic spatial-polarization hyper-controlled-not gate assisted by a quantum dot inside a one-side optical microcavity. *Laser Physics Letters*, 10(9):095202, jul 2013.

[46] Matthias Scholz, T Aichele, S Ramelow, and O Benson. Deutsch-jozsa algorithm using triggered single photons from a single quantum dot. *Physical review letters*, 96(18):180501, 2006.

[47] Xi-Lin Wang, Yi-Han Luo, He-Liang Huang, Ming-Cheng Chen, Zu-En Su, Chang Liu, Chao Chen, Wei Li, Yu-Qiang Fang, Xiao Jiang, et al. 18-qubit entanglement with six photons' three degrees of freedom. *Physical review letters*, 120(26):260502, 2018.

[48] Huan Cao, She-Cheng Gao, Chao Zhang, Jian Wang, De-Yong He, Bi-Heng Liu, Zheng-Wei Zhou, Yu-Jie Chen, Zhao-Hui Li, Si-Yuan Yu, et al. Distribution of high-dimensional orbital angular momentum entanglement at telecom wavelength over 1km of optical fibre. *arXiv preprint arXiv:1811.12195*, 2018.

[49] Siddharth Ramachandran, John M Fini, Marc Mermelstein, Jeffery W Nicholson, Samir Ghalmi, and Man F Yan. Ultra-large effective-area, higher-order mode fibers: a new strategy for high-power lasers. *Laser & Photonics Reviews*, 2(6):429–448, 2008.

[50] Matthew A Hall, Joseph B Altepeter, and Prem Kumar. Ultrafast switching of photonic entanglement. *Physical review letters*, 106(5):053901, 2011.

[51] Andreas Schreiber, Aurél Gábris, Peter P Rohde, Kaisa Laiho, Martin Štefaňák, Václav Potoček, Craig Hamilton, Igor Jex, and Christine Silberhorn. A 2d quantum walk simulation of two-particle dynamics. *Science*, 336(6077):55–58, 2012.

[52] B Brecht, Dileep V Reddy, C Silberhorn, and MG Raymer. Photon temporal modes: a complete framework for quantum information science. *Physical Review X*, 5(4):041017, 2015.

[53] Michael G Raymer and Ian A Walmsley. Temporal modes in quantum optics: then and now. *Physica Scripta*, 95(6):064002, 2020.

[54] Cody Jones, Danny Kim, Matthew T Rakher, Paul G Kwiat, and Thaddeus D Ladd. Design and analysis of communication protocols for quantum repeater networks. *New Journal of Physics*, 18(8):083015, 2016.

[55] Fumihiro Kaneda and Paul G Kwiat. High-efficiency single-photon generation via large-scale active time multiplexing. *Science advances*, 5(10):eaaw8586, 2019.

[56] Fumihiro Kaneda, Feihu Xu, Joseph Chapman, and Paul G Kwiat. Quantum-memory-assisted multi-photon generation for efficient quantum information processing. *Optica*, 4(9):1034–1037, 2017.

[57] E. Knill, R. Laflamme, and G. J. Milburn. A scheme for efficient quantum computation with linear optics. *Nature*, 409(6816):46–52, January 2001.

[58] Nicolas Sangouard, Christoph Simon, Jiří Minář, Hugo Zbinden, Hugues De Riedmatten, and Nicolas Gisin. Long-distance entanglement distribution with single-photon sources. *Physical Review A*, 76(5):050301, 2007.

[59] H-J Briegel, Wolfgang Dür, Juan I Cirac, and Peter Zoller. Quantum repeaters: the role of imperfect local operations in quantum communication. *Physical Review Letters*, 81(26):5932, 1998.

[60] Alexander I Lvovsky, Barry C Sanders, and Wolfgang Tittel. Optical quantum memory. *Nature photonics*, 3(12):706–714, 2009.

[61] Sebastian Zaiser, Torsten Rendler, Ingmar Jakobi, Thomas Wolf, Sang-Yun Lee, Samuel Wagner, Ville Bergholm, Thomas Schulte-Herbrüggen, Philipp Neumann, and Jörg Wrachtrup. Enhancing quantum sensing sensitivity by a quantum memory. *Nature communications*, 7, 2016.

[62] H. J. Kimble. The quantum internet. *Nature*, 453(7198):1023–1030, Jun 2008.

[63] TB Pittman, BC Jacobs, and JD Franson. Single photons on pseudodemand from stored parametric down-conversion. *Physical Review A*, 66(4):042303, 2002.

[64] C Xiong, X Zhang, Z Liu, MJ Collins, A Mahendra, LG Helt, MJ Steel, D-Y Choi, CJ Chae, PHW Leong, et al. Active temporal multiplexing of indistinguishable heralded single photons. *Nature communications*, 7, 2016.

[65] Yanhua Shih. Entangled biphoton source-property and preparation. *Reports on Progress in Physics*, 66(6):1009, 2003.

[66] Alexander Ling, Antia Lamas-Linares, and Christian Kurtsiefer. Absolute emission rates of spontaneous parametric down-conversion into single transverse gaussian modes. *Physical Review A*, 77(4):043834, 2008.

[67] J Nunn, NK Langford, WS Kolthammer, TFM Champion, MR Sprague, PS Michelberger, X-M Jin, DG England, and IA Walmsley. Enhancing multiphoton rates with quantum memories. *Physical review letters*, 110(13):133601, 2013.

[68] M. Hosseini, G. Campbell, B. M. Sparkes, P. K. Lam, and B. C. Buchler. Unconditional room-temperature quantum memory. *Nat Phys*, 7(10):794–798, Oct 2011.

[69] Hyunseok Jeong, Timothy C Ralph, and Warwick P Bowen. Quantum and classical fidelities for gaussian states. *JOSA B*, 24(2):355–362, 2007.

[70] Serge Massar and Sandu Popescu. Optimal extraction of information from finite quantum ensembles. *Physical review letters*, 74(8):1259, 1995.

[71] Michael A Nielsen and Isaac Chuang. Quantum computation and quantum information, 2002.

[72] Mustafa Gündoğan, Patrick M Ledingham, Kutlu Kutluer, Margherita Mazzera, and Hugues de Riedmatten. Solid state spin-wave quantum memory for time-bin qubits. *Physical review letters*, 114(23):230501, 2015.

[73] OA Collins, SD Jenkins, A Kuzmich, and TAB Kennedy. Multiplexed memory-insensitive quantum repeaters. *Physical review letters*, 98(6):060502, 2007.

[74] S Gao, O Lazo-Arjona, B Brecht, KT Kaczmarek, SE Thomas, J Nunn, PM Ledingham, DJ Saunders, and IA Walmsley. Optimal coherent filtering for single noisy photons. *Physical review letters*, 123(21):213604, 2019.

[75] TB Pittman and JD Franson. Cyclical quantum memory for photonic qubits. *Physical Review A*, 66(6):062302, 2002.

[76] Patrick M Leung and Timothy C Ralph. Quantum memory scheme based on optical fibers and cavities. *Physical Review A*, 74(2):022311, 2006.

[77] Olivier Landry, Jeroen Anton Willem van Houwelingen, Alexios Beveratos, Hugo Zbinden, and Nicolas Gisin. Quantum teleportation over the swisscom telecommunication network. *JOSA B*, 24(2):398–403, 2007.

[78] C Langer, R Ozeri, John D Jost, J Chiaverini, B DeMarco, A Ben-Kish, RB Blakestad, J Britton, DB Hume, Wayne M Itano, et al. Long-lived qubit memory using atomic ions. *Physical Review Letters*, 95(6):060502, 2005.

[79] Michael Fleischhauer, Atac Imamoglu, and Jonathan P Marangos. Electromagnetically induced transparency: Optics in coherent media. *Reviews of modern physics*, 77(2):633, 2005.

[80] Theresa F. M. Champion. *"Towards storage and retrieval of non-classical light in a broadband quantum memory - An investigation of free-space and cavity Raman memories"*. PhD thesis, University of Oxford, 2015.

[81] Michael Fleischhauer and Mikhail D Lukin. Dark-state polaritons in electromagnetically induced transparency. *Physical Review Letters*, 84(22):5094, 2000.

[82] DF Phillips, A Fleischhauer, A Mair, RL Walsworth, and Mikhail D Lukin. Storage of light in atomic vapor. *Physical Review Letters*, 86(5):783, 2001.

[83] J Cviklinski, J Ortalo, J Laurat, A Bramati, M Pinard, and E Giacobino. Reversible quantum interface for tunable single-sideband modulation. *Physical review letters*, 101(13):133601, 2008.

[84] AV Turukhin, VS Sudarshanam, MS Shahriar, JA Musser, BS Ham, and PR Hemmer. Observation of ultraslow and stored light pulses in a solid. *Physical Review Letters*, 88(2):023602, 2001.

[85] Mingtao Cao, Félix Hoffet, Shuwei Qiu, Alexandra S Sheremet, and Julien Laurat. Efficient reversible entanglement transfer between light and quantum memories. *Optica*, 7(10):1440–1444, 2020.

[86] Ya-Fen Hsiao, Pin-Ju Tsai, Hung-Shiue Chen, Sheng-Xiang Lin, Chih-Chiao Hung, Chih-Hsi Lee, Yi-Hsin Chen, Yong-Fan Chen, A Yu Ite, and Ying-Cheng Chen. Highly efficient coherent optical memory based on electromagnetically induced transparency. *Physical review letters*, 120(18):183602, 2018.

[87] Lijun Ma, Oliver Slattery, and Xiao Tang. Optical quantum memory based on electromagnetically induced transparency. *Journal of Optics*, 19(4):043001, 2017.

[88] A Nicolas, L Veissier, L Giner, E Giacobino, D Maxein, and J Laurat. A quantum memory for orbital angular momentum photonic qubits. *Nature Photonics*, 8(3):234–238, 2014.

[89] Valentina Parigi, Vincenzo D'Ambrosio, Christophe Arnold, Lorenzo Marrucci, Fabio Sciarrino, and Julien Laurat. Storage and retrieval of vector beams of light in a multiple-degree-of-freedom quantum memory. *Nature communications*, 6, 2015.

[90] Erhan Saglamyurek, Taras Hrushevskyi, Anindya Rastogi, Khabat Heshami, and Lindsay J LeBlanc. Coherent storage and manipulation of broadband photons via dynamically controlled autler–townes splitting. *Nature Photonics*, 12(12):774–782, 2018.

[91] Erhan Saglamyurek, Taras Hrushevskyi, Anindya Rastogi, Logan W Cooke, Benjamin D Smith, and Lindsay J LeBlanc. Storing short single-photon-level optical pulses in bose–einstein condensates for high-performance quantum memory. *New Journal of Physics*, 23(4):043028, 2021.

[92] P S Michelberger, T F M Champion, M R Sprague, K T Kaczmarek, M Barbieri, X M Jin, D G England, W S Kolthammer, D J Saunders, J Nunn, and I A Walmsley. Interfacing ghz-bandwidth heralded single photons with a warm vapour raman memory. *New Journal of Physics*, 17(4):043006, 2015.

[93] KF Reim, J Nunn, VO Lorenz, BJ Sussman, KC Lee, NK Langford, D Jaksch, and IA Walmsley. Towards high-speed optical quantum memories. *Nature Photonics*, 4(4):218–221, 2010.

[94] Philip J Bustard, Rune Lausten, Duncan G England, and Benjamin J Sussman. Toward quantum processing in molecules: A thz-bandwidth coherent memory for light. *Physical review letters*, 111(8):083901, 2013.

[95] DG England, PJ Bustard, J Nunn, R Lausten, and BJ Sussman. From photons to phonons and back: a thz optical memory in diamond. *Physical review letters*, 111(24):243601, 2013.

[96] Pascale Senellart, Glenn Solomon, and Andrew White. High-performance semiconductor quantum-dot single-photon sources. *Nature nanotechnology*, 12(11):1026, 2017.

[97] Erwin L Hahn. Spin echoes. *Physical review*, 80(4):580, 1950.

[98] Jérôme Ruggiero, Jean-Louis Le Gouët, Christoph Simon, and Thierry Chanelière. Why the two-pulse photon echo is not a good quantum memory protocol. *Physical Review A*, 79(5):053851, 2009.

[99] Nicklas Ohlsson, R Krishna Mohan, and Stefan Kröll. Quantum computer hardware based on rare-earth-ion-doped inorganic crystals. *Optics communications*, 201(1):71–77, 2002.

[100] Sebastian P Horvath, Mohammed K Alqedra, Adam Kinos, Andreas Walther, Jan Marcus Dahlström, Stefan Kröll, and Lars Rippe. Noise-free on-demand atomic frequency comb quantum memory. *Physical Review Research*, 3(2):023099, 2021.

[101] Chao Liu, Tian-Xiang Zhu, Ming-Xu Su, You-Zhi Ma, Zong-Quan Zhou, Chuan-Feng Li, and Guang-Can Guo. On-demand quantum storage of photonic qubits in an on-chip waveguide. *Physical Review Letters*, 125(26):260504, 2020.

[102] Tian Zhong, Jonathan M Kindem, John G Bartholomew, Jake Rochman, Ioana Craiciu, Evan Miyazono, Marco Bettinelli, Enrico Cavalli, Varun Verma, Sae Woo Nam, et al. Nanophotonic rare-earth quantum memory with optically controlled retrieval. *Science*, 357(6358):1392–1395, 2017.

[103] Mustafa Gündoğan, Patrick M. Ledingham, Attaallah Almasi, Matteo Cristiani, and Hugues de Riedmatten. Quantum Storage of a Photonic Polarization Qubit in a Solid. *Phys. Rev. Lett.*, 108(19):190504, May 2012.

[104] Zong-Quan Zhou, Wei-Bin Lin, Ming Yang, Chuan-Feng Li, and Guang-Can Guo. Realization of reliable solid-state quantum memory for photonic polarization qubit. *Phys. Rev. Lett.*, 108:190505, May 2012.

[105] Christoph Clausen, Félix Bussières, Mikael Afzelius, and Nicolas Gisin. Quantum storage of heralded polarization qubits in birefringent and anisotropically absorbing materials. *Phys. Rev. Lett.*, 108:190503, May 2012.

[106] M. Gündoğan, P. M. Ledingham, K. Kutluer, M. Mazzera, and H. De Riedmatten. Solid State Spin-Wave Quantum Memory for Time-Bin Qubits. *Phys. Rev. Lett.*, 114(23):1–5, 2015.

[107] Yi-Lin Hua, Tian-Shu Yang, Zong-Quan Zhou, Jian Wang, Xiao Liu, Zong-Feng Li, Pei-Yun Li, Yu Ma, Chao Liu, Peng-Jun Liang, Jun Hu, Xue Li, Chuan-Feng Li, and Guang-Can Guo. Storage of telecom-c-band heralded single photons with orbital-angular-momentum encoding in a crystal. *Science Bulletin*, 64(21):1577 – 1583, 2019.

[108] Jian-Shun Tang, Zong-Quan Zhou, Yi-Tao Wang, Yu-Long Li, Xiao Liu, Yi-Lin Hua, Yang Zou, Shuang Wang, De-Yong He, Geng Chen, Yong-Nan Sun, Ying Yu, Mi-Feng Li, Guo-Wei Zha, Hai-Qiao Ni, Zhi-Chuan Niu, Chuan-Feng Li, and Guang-Can Guo. Storage of multiple single-photon pulses emitted from a quantum dot in a solid-state quantum memory. *Nature Communications*, 6(1):8652, 2015.

[109] Daniel Rieländer, Kutlu Kutluer, Patrick M. Ledingham, Mustafa Gündoğan, Julia Fekete, Margherita Mazzera, and Hugues de Riedmatten. Quantum Storage of Heralded Single Photons in a Praseodymium-Doped Crystal. *Phys. Rev. Lett.*, 112(4):040504, January 2014.

[110] Imam Usmani, Mikael Afzelius, Hugues de Riedmatten, and Nicolas Gisin. Mapping multiple photonic qubits into and out of one solid-state atomic ensemble. *Nature Communications*, 1(1):12, 2010.

[111] Alessandro Seri, Dario Lago-Rivera, Andreas Lenhard, Giacomo Corrielli, Roberto Osellame, Margherita Mazzera, and Hugues de Riedmatten. Quantum storage of frequency-multiplexed heralded single photons. *Phys. Rev. Lett.*, 123:080502, Aug 2019.

[112] Mahmood Sabooni, Qian Li, Stefan Kröll, and Lars Rippe. Efficient quantum memory using a weakly absorbing sample. *Physical review letters*, 110(13):133604, 2013.

[113] J Nunn, K Reim, KC Lee, VO Lorenz, BJ Sussman, IA Walmsley, and D Jaksch. Multimode memories in atomic ensembles. *Physical Review Letters*, 101(26):260502, 2008.

[114] L-m Duan, MD Lukin, JI Cirac, and P Zoller. Long-distance quantum communication with atomic ensembles and linear optics. *Nature*, 414(6862):413–418, 2001.

[115] Nicolas Sangouard, Christoph Simon, Hugues De Riedmatten, and Nicolas Gisin. Quantum repeaters based on atomic ensembles and linear optics. *Reviews of Modern Physics*, 83(1):33, 2011.

[116] Sheng-Jun Yang, Xu-Jie Wang, Xiao-Hui Bao, and Jian-Wei Pan. An efficient quantum light–matter interface with sub-second lifetime. *Nature Photonics*, 10(6):381–384, 2016.

[117] A. E. Kozhekin, K. Mølmer, and E. Polzik. Quantum memory for light. *Phys. Rev. A*, 62:033809, Aug 2000.

[118] Alexey V Gorshkov, Axel André, Mikhail D Lukin, and Anders S Sørensen. Photon storage in λ-type optically dense atomic media. ii. free-space model. *Physical Review A*, 76(3):033805, 2007.

[119] Joshua Nunn. *"Quantum Memory in Atomic Ensembles"*. PhD thesis, University of Oxford, 2008.

[120] S.E. Thomas. *Efficient, low noise, mode-selective quantum memory.* PhD thesis, Imperial College London, 2019.

[121] J.H.D. Munns. *Optimisation and applications of a Raman quantum memory for temporal modes of light.* PhD thesis, Imperial College London, 2018.

[122] Chien Liu, Zachary Dutton, Cyrus H Behroozi, and Lene Vestergaard Hau. Observation of coherent optical information storage in an atomic medium using halted light pulses. *Nature*, 409(6819):490–493, 2001.

[123] Nikolay V Vitanov, Andon A Rangelov, Bruce W Shore, and Klaas Bergmann. Stimulated raman adiabatic passage in physics, chemistry, and beyond. *Reviews of Modern Physics*, 89(1):015006, 2017.

[124] Klaas Bergmann, Nikolay V Vitanov, and Bruce W Shore. Perspective: Stimulated raman adiabatic passage: The status after 25 years. *The Journal of chemical physics*, 142(17):170901, 2015.

[125] Rodney Loudon. *The quantum theory of light.* OUP Oxford, 2000.

[126] T Holstein and Hl Primakoff. Field dependence of the intrinsic domain magnetization of a ferromagnet. *Physical Review*, 58(12):1098, 1940.

[127] Wolfgang Dür, Guifre Vidal, and J Ignacio Cirac. Three qubits can be entangled in two inequivalent ways. *Physical Review A*, 62(6):062314, 2000.

[128] Guido Van Rossum and Fred L. Drake. *Python 3 Reference Manual.* CreateSpace, Scotts Valley, CA, 2009.

[129] M. Hazewinkel. *Runge-Kutta Method.* Encyclopaedia of Mathematics; Springer / Kluwer Academic Publishers 1995, 1995.

[130] M. Hazewinkel. *Chebyshev Iteration Method.* Encyclopaedia of Mathematics; Springer / Kluwer Academic Publishers 1995, 1995.

[131] J Nunn, IA Walmsley, MG Raymer, K Surmacz, FC Waldermann, Z Wang, and D Jaksch. Mapping broadband single-photon wave packets into an atomic memory. *Physical Review A*, 75(1):011401, 2007.

[132] Klaus F Reim, Patrick Michelberger, Ka C Lee, Joshua Nunn, Nathan K Langford, and Ian A Walmsley. Single-photon-level memory at room temperature. In *Quantum Electronics and Laser Science Conference*, page QThJ1. Optical Society of America, 2011.

[133] DG England, PS Michelberger, TFM Champion, KF Reim, KC Lee, MR Sprague, XM Jin, NK Langford, WS Kolthammer, J Nunn, et al. High-fidelity polarization storage in a gigahertz bandwidth quantum memory. *Journal of Physics B: Atomic, Molecular and Optical Physics*, 45(12):124008, 2012.

[134] DJ Saunders, JHD Munns, TFM Champion, C Qiu, KT Kaczmarek, E Poem, PM Ledingham, IA Walmsley, and J Nunn. Cavity-enhanced room-temperature broadband raman memory. *Physical review letters*, 116(9):090501, 2016.

[135] Roy J Glauber. The quantum theory of optical coherence. *Physical Review*, 130(6):2529, 1963.

[136] SE Thomas, JHD Munns, KT Kaczmarek, C Qiu, B Brecht, A Feizpour, PM Ledingham, IA Walmsley, J Nunn, and DJ Saunders. High efficiency raman memory by suppressing radiation trapping. *New Journal of Physics*, 19(6), 2017.

[137] Sarah E Thomas, Thomas M Hird, Joseph HD Munns, Benjamin Brecht, Dylan J Saunders, Joshua Nunn, Ian A Walmsley, and Patrick M Ledingham. Raman quantum memory with built-in suppression of four-wave-mixing noise. *Physical Review A*, 100(3):033801, 2019.

[138] P Walther, MD Eisaman, A André, F Massou, M Fleischhauer, AS Zibrov, and MD Lukin. Generation of narrow-bandwidth single photons using electromagnetically induced transparency in atomic ensembles. *International Journal of Quantum Information*, 5(01n02):51–62, 2007.

[139] E Poem, C Weinzetl, J Klatzow, KT Kaczmarek, JHD Munns, TFM Champion, DJ Saunders, J Nunn, and IA Walmsley. Broadband noise-free optical quantum memory with neutral nitrogen-vacancy centers in diamond. *Physical Review B*, 91(20):205108, 2015.

[140] Igor Vurgaftman and Mark Bashkansky. Suppressing four-wave mixing in warm-atomic-vapor quantum memory. *Physical Review A*, 87(6):063836, 2013.

[141] Karsten B Dideriksen, Rebecca Schmieg, Michael Zugenmaier, and Eugene S Polzik. Room-temperature single-photon source with near-millisecond built-in memory. *arXiv preprint arXiv:2010.06875*, 2020.

[142] KC Lee, BJ Sussman, MR Sprague, P Michelberger, KF Reim, J Nunn, NK Langford, PJ Bustard, D Jaksch, and IA Walmsley. Macroscopic non-classical states and terahertz quantum processing in room-temperature diamond. *Nature Photonics*, 6(1):41–44, 2012.

[143] Duncan G England, Kent AG Fisher, Jean-Philippe W MacLean, Philip J Bustard, Rune Lausten, Kevin J Resch, and Benjamin J Sussman. Storage and retrieval of

thz-bandwidth single photons using a room-temperature diamond quantum memory. *Physical review letters*, 114(5):053602, 2015.

[144] J. Nunn, J. H. D. Munns, S. Thomas, K. T. Kaczmarek, C. Qiu, A. Feizpour, E. Poem, B. Brecht, D. J. Saunders, P. M. Ledingham, Dileep V. Reddy, M. G. Raymer, and I. A. Walmsley. Theory of noise suppression in Λ-type quantum memories by means of a cavity. *Phys. Rev. A*, 96:012338, Jul 2017.

[145] Gleb Romanov, Chris O'Brien, and Irina Novikova. Suppression of the four-wave mixing amplification via raman absorption. *Journal of Modern Optics*, 63(20):2048–2057, 2016.

[146] Vladislav Popkov, Simon Essink, Carlo Presilla, and Gunter Schütz. Effective quantum zeno dynamics in dissipative quantum systems. *Physical Review A*, 98(5):052110, 2018.

[147] Prem Kumar and Mikhail I Kolobov. Degenerate four-wave mixing as a source for spatially-broadband squeezed light. *Optics communications*, 104(4-6):374–378, 1994.

[148] Jean E Sansonetti and William Clyde Martin. Handbook of basic atomic spectroscopic data. *Journal of physical and chemical reference data*, 34(4):1559–2259, 2005.

[149] L Essen and JVL Parry. An atomic standard of frequency and time interval: a caesium resonator. *Nature*, 176(4476):280–282, 1955.

[150] Georges Audi, Olivier Bersillon, Jean Blachot, and Aaldert Hendrik Wapstra. The nubase evaluation of nuclear and decay properties. *Nuclear Physics A*, 729(1):3–128, 2003.

[151] Daniel A Steck. Cesium d line data, 2003.

[152] Andreas F Molisch and Bernhard P Oehry. *Radiation trapping in atomic vapours*. Oxford University Press, 1998.

[153] Mark A Rosenberry, JP Reyes, D Tupa, and Timothy J Gay. Radiation trapping in rubidium optical pumping at low buffer-gas pressures. *Physical Review A*, 75(2):023401, 2007.

[154] William Happer. Optical pumping. *Reviews of Modern Physics*, 44(2):169, 1972.

[155] Benjamin Brecht, Andreas Eckstein, Raimund Ricken, Viktor Quiring, Hubertus Suche, Linda Sansoni, and Christine Silberhorn. Demonstration of coherent time-frequency schmidt mode selection using dispersion-engineered frequency conversion. *Physical Review A*, 90(3):030302, 2014.

[156] DV Reddy, MG Raymer, and CJ McKinstrie. Sorting photon wave packets using temporal-mode interferometry based on multiple-stage quantum frequency conversion. *Physical Review A*, 91(1):012323, 2015.

[157] Vahid Ansari, John M Donohue, Benjamin Brecht, and Christine Silberhorn. Tailoring nonlinear processes for quantum optics with pulsed temporal-mode encodings. *Optica*, 5(5):534–550, 2018.

[158] George E Andrews, Richard Askey, Ranjan Roy, Ranjan Roy, and Richard Askey. *Special functions*, volume 71. Cambridge university press Cambridge, 1999.

[159] Serkan Ates, Imad Agha, Angelo Gulinatti, Ivan Rech, Antonio Badolato, and Kartik Srinivasan. Improving the performance of bright quantum dot single photon sources using temporal filtering via amplitude modulation. *Scientific Reports*, 3(1):1–7, 2013.

[160] Charles Santori, David Fattal, Jelena Vuckovic, Glenn S Solomon, and Yoshihisa Yamamoto. Indistinguishable photons from a single-photon device. *nature*, 419(6907):594, 2002.

[161] JH Eberly. Schmidt analysis of pure-state entanglement. *Laser physics*, 16(6):921–926, 2006.

[162] Peter J Mosley, Jeff S Lundeen, Brian J Smith, Piotr Wasylczyk, Alfred B U'Ren, Christine Silberhorn, and Ian A Walmsley. Heralded generation of ultrafast single photons in pure quantum states. *Physical Review Letters*, 100(13):133601, 2008.

[163] Evan Meyer-Scott, Nicola Montaut, Johannes Tiedau, Linda Sansoni, Harald Herrmann, Tim J Bartley, and Christine Silberhorn. Limits on the heralding efficiencies and spectral purities of spectrally filtered single photons from photon-pair sources. *Physical Review A*, 95(6):061803, 2017.

[164] Andreas Eckstein, Benjamin Brecht, and Christine Silberhorn. A quantum pulse gate based on spectrally engineered sum frequency generation. *Optics express*, 19(15):13770–13778, 2011.

[165] Irina Novikova, Nathaniel B Phillips, and Alexey V Gorshkov. Optimal light storage with full pulse-shape control. *Physical Review A*, 78(2):021802, 2008.

[166] Stephen Brierley, Stefan Weigert, and Ingemar Bengtsson. All mutually unbiased bases in dimensions two to five. *arXiv preprint arXiv:0907.4097*, 2009.

[167] D Main, TM Hird, S Gao, E Oguz, DJ Saunders, IA Walmsley, and PM Ledingham. Preparing narrow velocity distributions for quantum memories in room-temperature alkali vapours. *arXiv preprint arXiv:2011.03766*, 2020.

[168] D Main, TM Hird, S Gao, IA Walmsley, and PM Ledingham. Room temperature atomic frequency comb memory for light. *arXiv preprint arXiv:2011.03765*, 2020.

[169] Daryl W. Preston. Doppler-free saturated absorption: Laser spectroscopy. *American Journal of Physics*, 64(11):1432–1436, November 1996.

[170] J. Nunn, N. K. Langford, W. S. Kolthammer, T. F. M. Champion, M. R. Sprague, P. S. Michelberger, X.-M. Jin, D. G. England, and I. A. Walmsley. Enhancing Multiphoton Rates with Quantum Memories. *Phys. Rev. Lett.*, 110(13):133601, March 2013.

[171] K. T. Kaczmarek, P. M. Ledingham, B. Brecht, S. E. Thomas, G. S. Thekkadath, O. Lazo-Arjona, J. H. D. Munns, E. Poem, A. Feizpour, D. J. Saunders, J. Nunn, and I. A. Walmsley. High-Speed Noise-Free Optical Quantum Memory. *Phys. Rev. A*, 97(4):042316, April 2018.

[172] Ran Finkelstein, Eilon Poem, Ohad Michel, Ohr Lahad, and Ofer Firstenberg. Fast, Noise-Free Memory for Photon Synchronization at Room Temperature. *Science Advances*, 4(1):eaap8598, January 2018.

[173] Ran Finkelstein, Ohr Lahad, Itsik Cohen, Omri Davidson, Shai Kiriati, Eilon Poem, and Ofer Firstenberg. Optical protection of a collective state from inhomogeneous dephasing. *arXiv preprint arXiv:2004.02295*, 2020.

[174] Wenhao Li, Xiang Peng, Dmitry Budker, Arne Wickenbrock, Bo Pang, Rui Zhang, and Hong Guo. Hybrid optical pumping of k and rb atoms in a paraffin coated vapor cell. *Opt. Lett.*, 42(20):4163–4166, Oct 2017.

[175] Wenhao Li, Mikhail Balabas, Xiang Peng, Szymon Pustelny, Arne Wickenbrock, Hong Guo, and Dmitry Budker. Characterization of high-temperature performance of cesium vapor cells with anti-relaxation coating. *Journal of Applied Physics*, 121(6):063104, 2017.

[176] KT Kaczmarek, PM Ledingham, B Brecht, SE Thomas, GS Thekkadath, O Lazo-Arjona, JHD Munns, E Poem, A Feizpour, DJ Saunders, et al. High-speed noise-free optical quantum memory. *Physical Review A*, 97(4):042316, 2018.

[177] William Esco Moerner and Gary C Bjorklund. *Persistent spectral hole-burning: science and applications*, volume 1. Springer, 1988.

[178] Hugues de Riedmatten, Mikael Afzelius, Matthias U. Staudt, Christoph Simon, and Nicolas Gisin. A Solid-State Light-Matter Interface at the Single-Photon Level. *Nature*, 456(7223):773–777, December 2008.

[179] Morgan P. Hedges, Jevon J. Longdell, Yongmin Li, and Matthew J. Sellars. Efficient Quantum Memory for Light. *Nature*, 465(7301):1052–1056, June 2010.

[180] Georg Heinze, Christian Hubrich, and Thomas Halfmann. Stopped Light and Image Storage by Electromagnetically Induced Transparency up to the Regime of One Minute. *Phys. Rev. Lett.*, 111(3):033601, July 2013.

[181] Kutlu Kutluer, María Florencia Pascual-Winter, Julian Dajczgewand, Patrick M. Ledingham, Margherita Mazzera, Thierry Chanelière, and Hugues de Riedmatten. Spectral-hole memory for light at the single-photon level. *Phys. Rev. A*, 93(4):040302, April 2016.

[182] Julia Fekete, Daniel Rieländer, Matteo Cristiani, and Hugues de Riedmatten. Ultranarrow-band photon-pair source compatible with solid state quantum memories and telecommunication networks. *Physical review letters*, 110(22):220502, 2013.

[183] Neil Sinclair, Erhan Saglamyurek, Hassan Mallahzadeh, Joshua A Slater, Mathew George, Raimund Ricken, Morgan P Hedges, Daniel Oblak, Christoph Simon, Wolfgang Sohler, et al. Spectral multiplexing for scalable quantum photonics using an atomic frequency comb quantum memory and feed-forward control. *Physical review letters*, 113(5):053603, 2014.

[184] Mikael Afzelius, Christoph Simon, Hugues de Riedmatten, and Nicolas Gisin. Multimode quantum memory based on atomic frequency combs. *Phys. Rev. A*, 79:052329, May 2009.

[185] Duncan G England, Kent AG Fisher, Jean-Philippe W MacLean, Philip J Bustard, Khabat Heshami, Kevin J Resch, and Benjamin J Sussman. Phonon-mediated nonclassical interference in diamond. *Physical review letters*, 117(7):073603, 2016.

[186] Mikael Afzelius, Imam Usmani, Atia Amari, Björn Lauritzen, Andreas Walther, Christoph Simon, Nicolas Sangouard, Ji ří Minář, Hugues de Riedmatten, Nicolas Gisin, and Stefan Kröll. Demonstration of atomic frequency comb memory for light with spin-wave storage. *Phys. Rev. Lett.*, 104:040503, Jan 2010.

[187] J. L. Rubio, D. Viscor, J. Mompart, and V. Ahufinger. Atomic-frequency-comb quantum memory via piecewise adiabatic passage. *Phys. Rev. A*, 98(4):043834, October 2018.